FATIGUE DAMAGE MECHANISMS IN FIBER REINFORCED COMPOSITE MATERIALS INCLUDING THE EFFECT OF CYCLIC LOADING FREQUENCY

by

Richard Scott Williams

Dissertation submitted to the Graduate Faculty of the
Virginia Polytechnic Institute and State University
in partial fulfillment of the requirements for the degree of
DOCTOR OF PHILOSOPHY
in
Materials Engineering Science

APPROVED:

K.L. Reifsnider, Chairman

C.W. Smith	W.W. Stinchcomb
E.G. Henneke	J.H. Steele, Jr.

January, 1975
Blacksburg, Virginia

ACKNOWLEDGEMENTS

The author wishes to
--thank his wife and family for their patience and understanding throughout this endeavor.
--thank Dr. Kenneth Reifsnider for his assistance and guidance without which this work would not have been possible.
--thank Dr. Wayne Stinchcomb for his help and advice. And also thank Dr. Henneke, Dr. Steele, and Prof. Smith for serving on his committee.
--express his gratitude to the Air Force Office of Scientific Research and project monitors, Dr. Jacob Pomerantz and Dr. William Walker, who supported this research through contract no. AFOSR-72-2358.
--thank Mr. G.K. Mc Cauley and Mr. Robert Chaves for their photographic and drafting assistance.
--acknowledge the faculty and staff of the Department of Engineering Science and Mechanics with whom he has had the pleasure of being associated for three years.

TABLE OF CONTENTS

TABLE OF CONTENTS (cont.)

LIST OF FIGURES

LIST OF FIGURES (cont.)

LIST OF FIGURES (cont.)

LIST OF TABLES

CHAPTER I
INTRODUCTION

Over the past decade extensive developmental work has been devoted to the area of fiber reinforced composite materials. This is due, primarily, to their high strength-to-weight ratio and structural design flexibility, which allows the directional material properties to be tailored to fit the loading application. Since one of the most promising applications of these materials is in aerospace hardware, where fatigue is a primary mechanism of failure, there has been a substantial effort to document the fatigue behavior.

Compared to isotropic homogeneous materials, the mechanisms by which composite materials fail are several orders of magnitude more complex. In homogeneous materials, fracture usually results from the nucleation and eventual propagation of a single crack to failure. For composite materials this process consists of a number of interelated mechanisms, including delamination, debonding, fiber breakage, void growth, matrix crazing, and matrix cracking. Because of these varied and interelated damage mechanisms, conventional means of fracture analysis are not directly applicable. The fracture analysis, therefore, must be modified(or discarded entirely, in favor of a new approach) in order that the fatigue fracture mechanisms can be correctly characterized.

Since composite materials are subjected to a wide spectrum of loading frequencies, as a consequence of their typical applications, the effect of frequency on damage initiation and propagation is of concern. This effect has been noted in metals(1) at high temperatures and/or

at high cycling frequencies, but it has not previously been observed or characterized in composite materials.

It will be the intent of this dissertation to characterize fatigue and fracture damage mechanisms and account for the effect of frequency on these processes in fiber reinforced composite materials. The approach will be many faceted, analyzing the problem from several different viewpoints. Structural aspects of fatigue damage will be investigated utilizing large amounts of experimental data; physical aspects of fracture will be examined by means of scanning electron microscopy; damage extent and propagation will be monitored and studied experimentally using energy-emission methods, such as acoustic and thermal emissions; and finally, using an energy criterion as a basis, a failure theory will be proposed.

The organization of this dissertation will be arranged so as to devote a chapter to each of the previously mentioned areas, discussing it separately and completely. Finally, in a summary chapter, each of these areas will be interelated and major conclusions will be listed.

GENERAL LITERATURE SURVEY

Earlier work includes a great deal of research which was done to characterize the fatigue properties of composite materials with different ply orientations and matrix/fiber combinations(2-8). Conventional testing methods were used and S/N type curves were developed indicating good fatigue resistance. Endurance limits were measured, using fracture as a criterion for failure, of 70-75% the ultimate stress.

In an effort to characterize the mechanisms by which fatigue damage propagates in aluminum matrix composites by means of photomicrographs of sections within the damage affected zone, Baker(9) noted a variety of

damage mechanisms, none of which appeared to dominate fracture. Schwabe(10) investigated matrix crazing by using a clear matrix with glass fibers. Using single-edge-notched(SEN) tensile specimens, Underwood(11) studied crack tip deformation and produced a series of crack propagation photomicrographs. The conclusion drawn by the previous investigators and most others in the field is that damage propagates by means of a complex combination of several mechanisms.

A number of attempts have also been made to apply linear elastic fracture mechanics(LEFM) to the fracture of composite materials. Using SEN specimens, Beaumont and Tetelman(12), and Konish et al(13) have measured critical values of the stress intensity factor(K_{Ic}) and strain energy release rate(G_{Ic}) for epoxy-based composites. Zweben (14) has developed a model for a center cracked plate based on a ligament theory. Using a Bowie solution, Waddoups et al(15) investigated radial cracks eminating from circular cutouts in plates. Mandell and Meier(16) have attempted to apply a Paris type crack propagation law to SEN unidirectional glass/epoxy specimens. Generally, although physical evidence exists(and is acknowledged by most investigators) that the fracture process is characterized by several different damage mechanisms, the LEFM model proposed by these investigators, and used in their analysis, assumes the propagation of a single self-similar through-crack to fracture.

There has been very little work done pertaining to the effect of frequency on composite material damage processes. Dally and Broutman(17) investigated this effect in glass/epoxy. They found the effect to be most predominate at high stress levels. These effects have also been noted by Liu, Stinchcomb, and Heller(18) in load controlled tests of graphite/epoxy and boron/epoxy.

This initial literature survey has been included to generally define trends and directions that previous work pertaining to fatigue and fracture of composite materials has taken. As it is applicable, the full extent of previous investigations, as they relate to each chapter, will be presented in greater detail.

CHAPTER II

EXPERIMENTAL FATIGUE INVESTIGATIONS

This chapter presents the results of a large number of fatigue tests, and investigates the effect of cyclic frequency and specimen conditioning on the damage processes.

INTRODUCTION

In any experimental investigation that seeks to determine the effect of one or more parameters on a process, it is essential to control all other possible test parameters and at the same time monitor all parameters, both controlled and uncontrolled. It is this philosophy that was applied to a large number of fatigue tests that sought to characterize the fatigue damage process, accounting for the effect of cyclic frequency and other variables, such as specimen conditioning.

It will be the purpose of this chapter to discuss and describe the experimental methods pertaining to the entire research effort, including those applying to areas discussed in subsequent chapters. The results of a large number of fatigue tests of boron/epoxy and boron/aluminum, which describe the effects of cyclic frequency and specimen conditioning, will be presented and discussed. In addition to these series of tests, static tests at different temperatures, low cycle fatigue tests(both load and strain controlled), and static and cyclic investigations of specially laid up panels and specimen configurations have been conducted. This has resulted in a substantial data base, with the number of tests run well over two hundred. Due to the large volume of this test data, only tables summarizing the results will be presented in this chapter. A detailed presentation is contained in references 19-22.

EXPERIMENTAL METHODS

Three basic types of tests were performed. Virgin cyclic stress/strain(σ/ϵ) tests were performed(to failure) in the manner described by Raske and Morrow(23) on undamaged specimens at different cyclic loading frequencies. The cyclic σ/ϵ curve was obtained by plotting the strain at a given level versus the maximum stress corresponding to the strain for that level. These curves were used to establish running parameters for the fatigue tests. The fatigue tests were run at a constant strain amplitude for a fixed length, usually 1500K cycles. The normal proceedure was to try to minimize the R value for the test series by choosing as low a value of minimum strain as possible, limited by the responce of the loading device. Lastly, 'post/mortem'(P/M) cyclic σ/ϵ tests were then run on the fatigue damaged specimens (to failure) in the same manner as were the virgin cyclic σ/ϵ tests. These tests were used to establish the extent of the fatigue damage.

All tests were run in a strain-controlled mode using a one inch(2.54cm.) gage length , clip-on extensometer designed for fatigue applications. Also, as mentioned earlier, prior to each test the specimens were preloaded to a set value of strain to establish a static modulus and to precondition specimens prior to fatiguing. A step-loading procedure was used in reaching running conditions for the fatigue tests. The normal procedure was to increment ϵ_{max} to 40%, 60%, 80%, 90% and then 100% of the running condition strain by 5K cycle increments, thereby reaching running conditions in about 25K cycles.

Two basic types of specimens were used in these tests: boron/aluminum(B/Al) and boron/epoxy(B/Ep). Both seven inches(17.78cm.) long by one inch(2.54cm.) wide by eight plies thick with a centered $\frac{1}{4}$ inch(.635cm.) diameter

hole(Figure 1). End tabs were not used on either type of specimen.

The B/Al specimens were supplied by Amercom Corp. and consisted of about 50 volume percent boron(0.142mm) embedded in a 6061 aluminum matrix. The specimens were symmetric lay-ups with ply orientations of $(0^\circ; \pm 45^\circ; 0^\circ)_{sym}$. Earlier specimens had punched holes using a Roper-Whitney no. 5 punch, but to achieve a greater control over the hole condition, later specimens had holes machined by electrical discharge machining(EDM). The specimens were received in two different batches with somewhat different properties and therefore are designated as B/Al I and B/Al II, respectfully. Also, the type of hole is denoted by 'a'for a punched hole and 'b' for an EDM hole, therefore, a batch number two specimen with an EDM hole would be designated as B/Al IIb, and so on.

The B/Ep was supplied by two different vendors. The B/Ep from Brunswich Corp., designated type I, was made of AVCO 55-05 boron tape. This resulted in about a 55-60 volume percent fiber with less than a 5% void content. The ply orientations were $(0^\circ; -45^\circ; +45^\circ; 0^\circ; 0^\circ; -45^\circ; +45^\circ; 0^\circ)$. The holes were drilled using a Branson Ultrasonic drill. The second batch of B/Ep was obtained from AVCO, Inc. and was made of AVCO 55-05 boron tape resulting in 50 volume percent fiber. The ply orientations were symmetric with the order being $(0^\circ; \pm 45^\circ; 0^\circ)_{sym}$. Again, the holes were drilled ultrasonically. This batch was designated group II.

The tests were run on an MTS servo-controlled, closed-loop, tension-torsion testing machine, with an axial capacity of 50,000 pounds(222.411N) and a torsional capacity of 20,000 in-lbs(2,259N-m). The tests were run in the axial mode using the torsional mode to prevent any specimen twisting. In the axial mode the testing machine

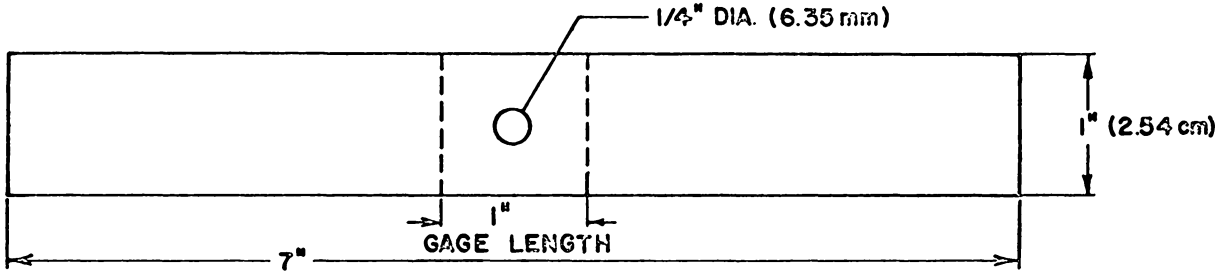

TEST SPECIMEN

Figure 1. Test specimen showing gage length.

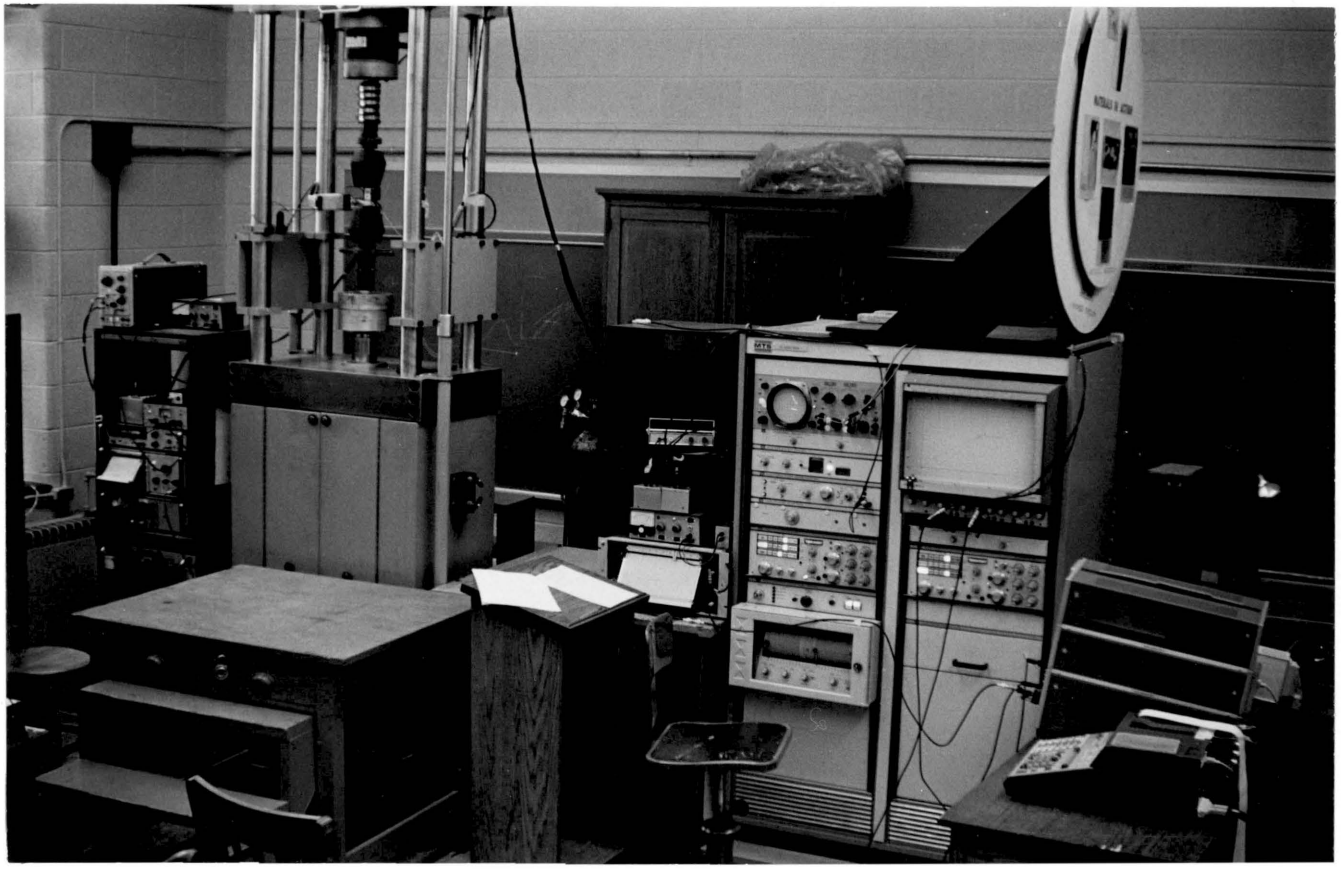

Figure 2. Picture of over all testing apparatus.

has the capbility of monitoring, continuously, the load, strain, and displacement signals and selecting any one of these as the controlled parameter. In the piston displacement ranges required of these tests, the testing machine has an upper response limit of about 50-60 cycles per second. To allow a margin of reliability, the maximum loading frequency for any series of tests was 45Hz.

The specimens were held using Instron 20,000 pound (88,964n) wedge grips. The grip faces were partially filled with epoxy and the specimen ends wrapped with medium grit emery paper, thereby preventing grip failures and eliminating the need for end tabs on the specimens. A restrained Instron universal joint was used to insure proper alignment.

During the tests, as many physical and material parameters as practicably possible were monitored. Also, since fatigue is a dynamic real-time process, these parameters were also monitored continuously in real-time. Parameters monitored continuously were load, strain, surface temperature distribution, and acoustic emission. Also periodically throughout the test,pictures of the extent of surface damage were taken. By means of several electronic systems and real-time data acquisition and reduction equipment, these parameters were operated upon, resulting in the following variables as output: maximum strain, load at maximum strain, minimum strain, load at minimum strain, dynamic secant compliance(C_d), specimen damping(ΔU), specific specimen damping($\Delta U/U$), point-wise specimen temperatures, acoustic emission rate, and totalized acoustic emission counts.

A block diagram of the functional components of the acoustic emission(A.E.) system is shown in Figure 3. This system incorporated a programmable gate, sample rate and read out. Therefore, it was possible to look

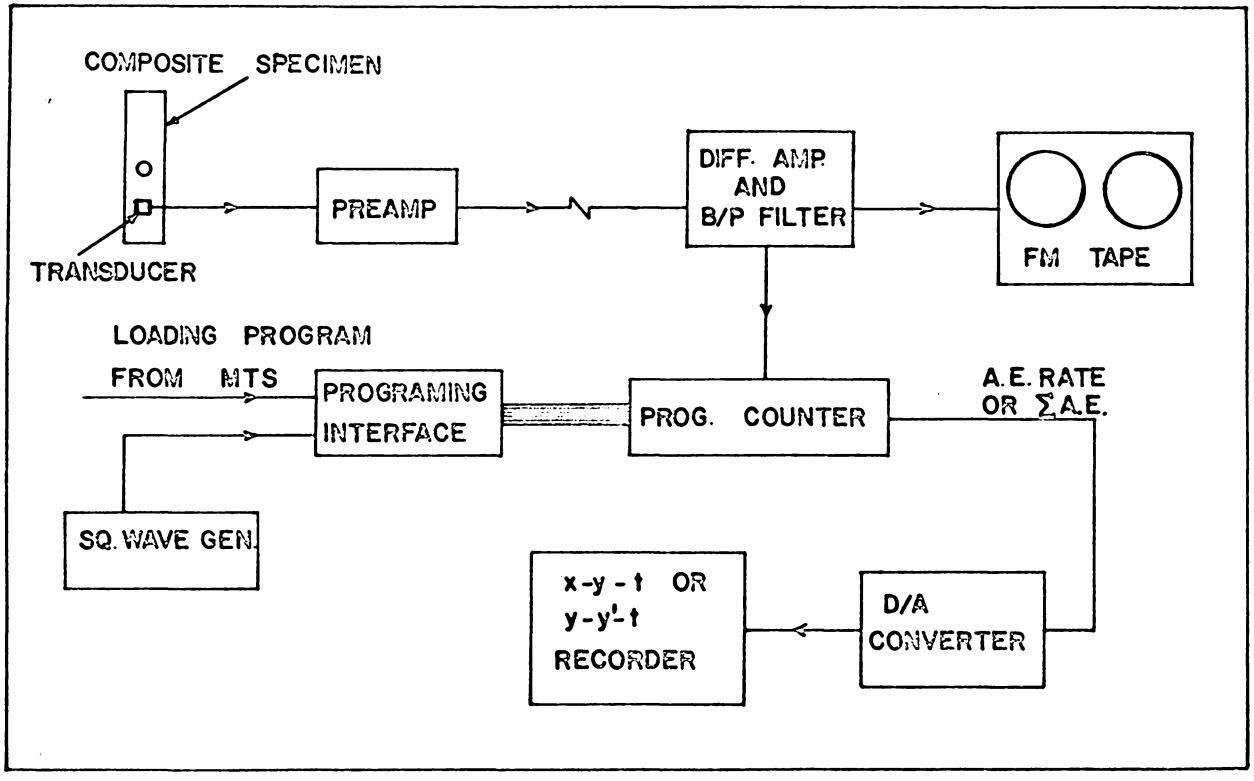

Figure 3. Schematic of acoustic emission system.

at the acoustic emission over a specific part of the loading function. The normal practice was to look at A. E. generated only during the top half of the loading signal. By doing this, acoustic emission generated at and approaching high stress levels where damage is most likely to occur was recorded, and the A.E. generated during unloading and at low stress levels where damage is least likely to occur was not. In this manner, specimen fretting and machine noise were largely avoided. Also, this system provided the option of recording totalized A.E. or A.E. rate averaged over long periods of time(10sec. to 5min.).

A broad-band Panametrics acoustic emission transducer with a center frequency of 100KHz was bonded to the specimen using 3M double-stick tape. Its signal was amplified 60db by a Panametrics preamp incorporating a bandpass of 10KHz-300KHz, to eliminate transmission noise. This was processed by a Hewlett-Packard programable counter. This counter was interfaced to an inhouse controller that controlled the sample interval and the output mode and frequency. The counter output (in BCD form) was channeled through a D/A convertor to one of several analog recording devices.

An AGA Thermovision thermographic video-camera (Figure 4) was used to record the surface temperature distribution of the specimen during cyclic loading. The unit is a real-time camera that scans at a continuos rate of 16 frames/second. The infrared detector is an indium antimonide photo-voltaic crystal which is cooled by liquid nitrogen and has an infrared sensitivity in the range of 2.0-5.6 microns. Using a 10° lens with an extension tube, a differential temperature sensitivity, over a scanned area of 4.2 x 4.2cm., of0.2° C was achieved. Video presentation is available in both a variable black and white mode and a continuously adjustable ten-color calibrated isotherm

Figure 4. Picture of thermographic camera.

display. Time resolved data was recorded using a Honeywell 5600B FM/Video tape recorder and still data was acquired using a Nikon F2 35mm still camera.

A Tektronix DPO 3107 system (Figure 5) was used to monitor the load and strain signals and the output of the acoustic emission system. The Tektronix system consists of a four channel digital processor with a 4000 word (of 10 bit each) nonvolitile memory and a digital oscilloscope coupled by an intelligent interface to a TEK 31 programmable calculator. The heart of this interface is an Intel 8008 micro processor.

An inhouse developed software package controlled the data sampling and reduction. It was executed in the following sequence: simultaneously load, strain and acoustic emission signals are digitized and stored, and then signal averaged to minimize noise. The stress and strain signals are searched for corresponding maxima and minima and then cross plotted on the CRT to form a hysteresis loop. This is then intergrated numerically to give the area under the curves. The output, in the form of max and min stress and strain, dynamic compliance, damping, specific damping and totalized acoustic emmission, keyed to the number of elapsed cycles is printed out on a thermal printer. The program has provisions for continuous unattended data logging and reduction with user specified intervals or one shot sampling triggered by the user. Initialization, calibration and program reload are also handled by the software.

The DPO system was also interfaced with programmable digital plotter(Tektronix 4661). With the addition of the plotter to the system, it is possible to plot in real-time all the critical parameters on one composite plot versus cycles. This enabled testing trends to be observed while the test was in progress and appropriate

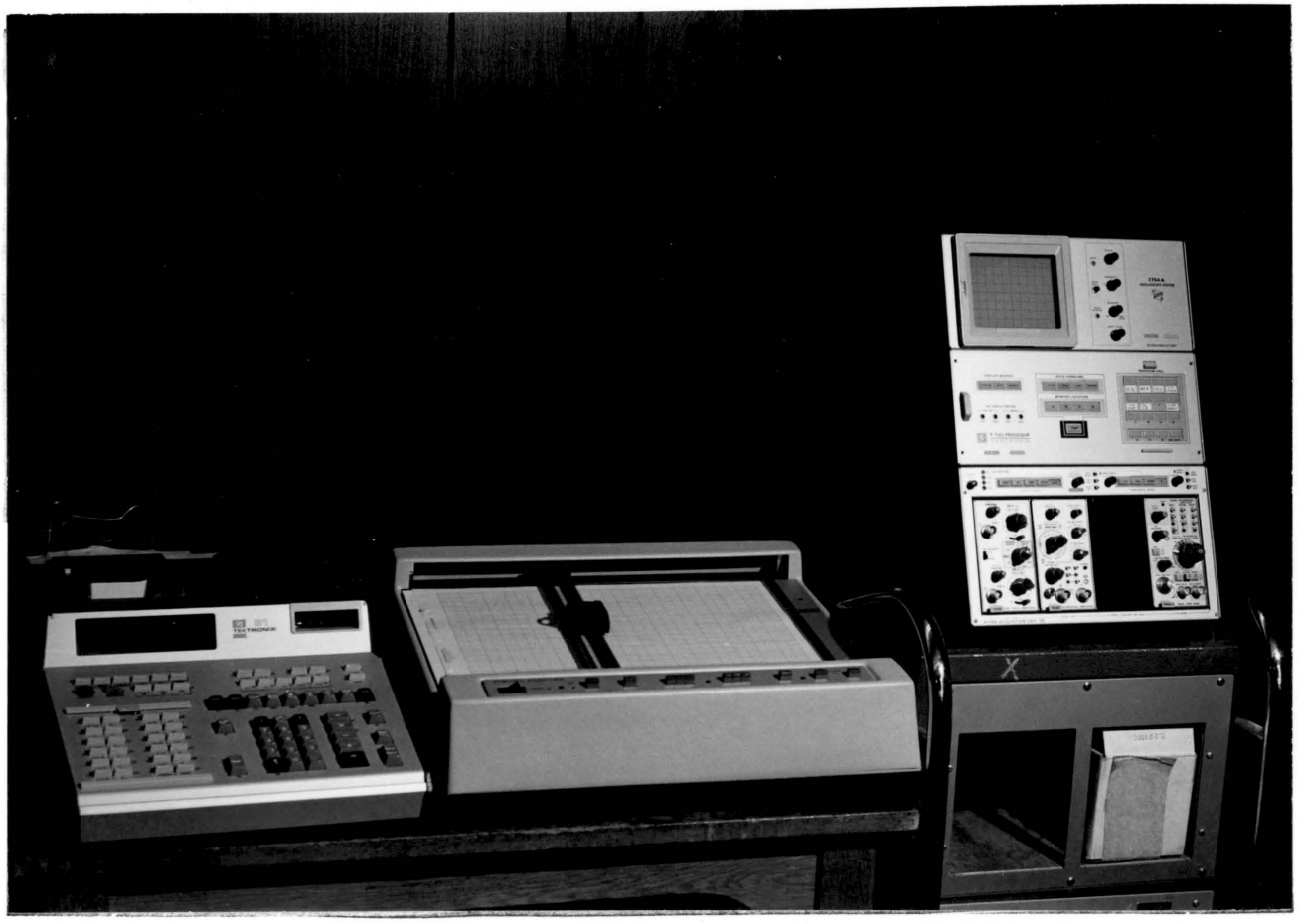

Figure 5. Picture of Tektronix digital data acquisition system.

measures taken if necessary. The numerical data from the thermal printer was also punched onto cards and used on the IBM/CALCOMP plotter for additional plotting and cross-plotting.

Fracture surface analysis was performed using an AMR model 900 scanning electron microscope. The unit has better than 200A resolution at 20KV and is capable of magnifications of 20x to 100,000x at a working distance of 12mm. Since it was the general fracture surface characteristics that was of interest, most work was done at 100x to 150x. Occasionally, to further investigate matrix or fiber fracture detail, magnifications of up to 3500x were used. The B/Al specimens required no preparation other than cleaning, but it was necessary to gold sputter-coat the B/Ep before viewing.

RESULTS

As previously stated in the introduction, the results presented in this section are summaries of the data contained in references 19-22. Typical examples of the data are shown in Figures 6-8. A composite plot of virgin cyclic σ/ϵ tests of B/Ep II at several test frequencies is shown in Figure 6. The results of several 15Hz. B/Ep II fatigue tests and their respective P/M cyclic σ/ϵ tests are shown in Figures 7 and 8. The characteristic rapid decrease in stress, which is indicative of specimen damage, shown in Figure 7 is quite typical of most tests. Usually 80% to 90% of the specimen damage occurs within the first 500K cycles of a 1500K cycle test. In some cases a second rapid decrease in stress occurs near the end of the test, but this has been infrequent.

Summaries of material properties and changes in material properties during fatigue and cyclic σ/ϵ tests

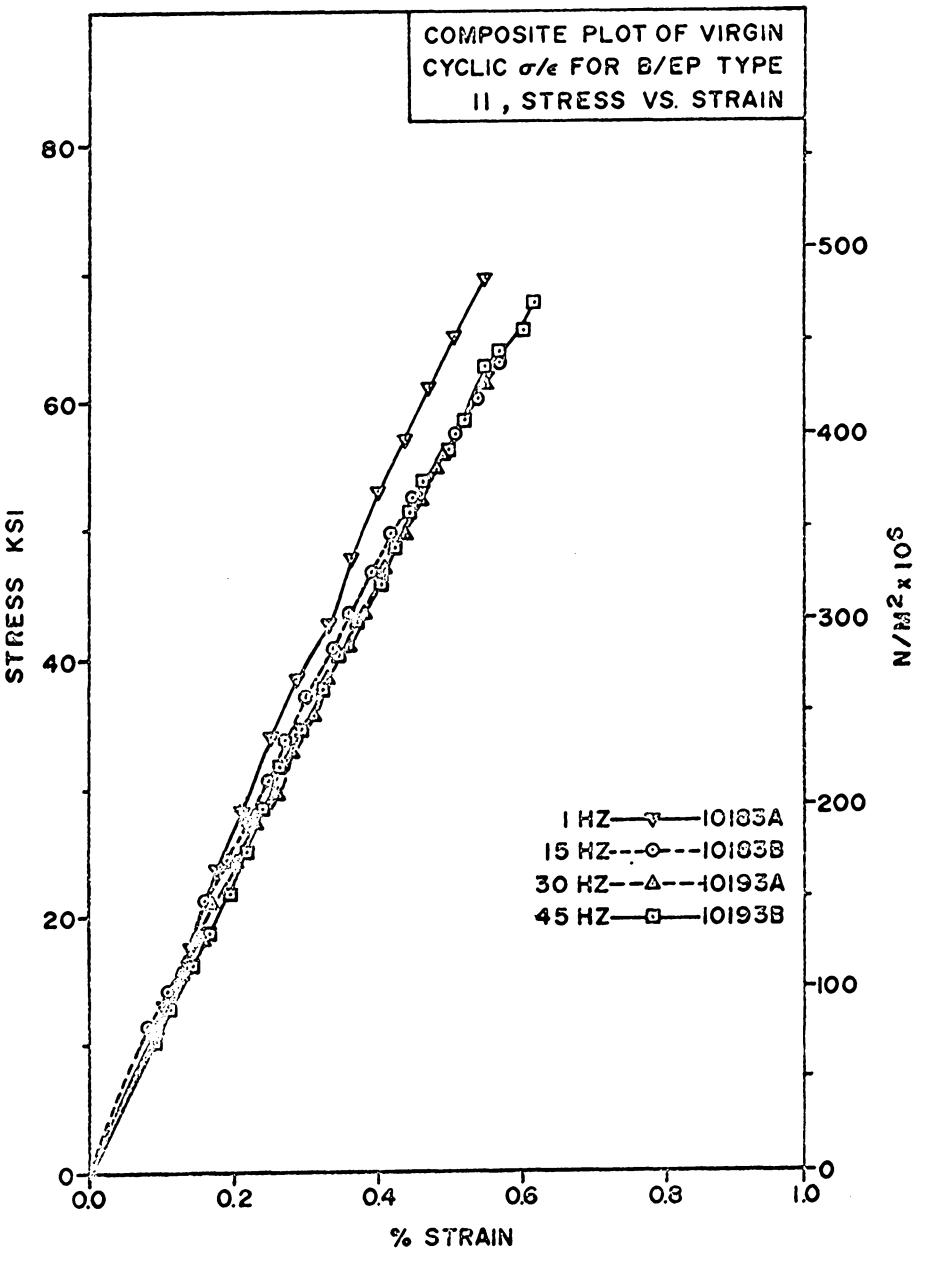

Figure 6. Composite plot of virgin cyclic σ/ε tests of B/Ep II, stress versus strain.

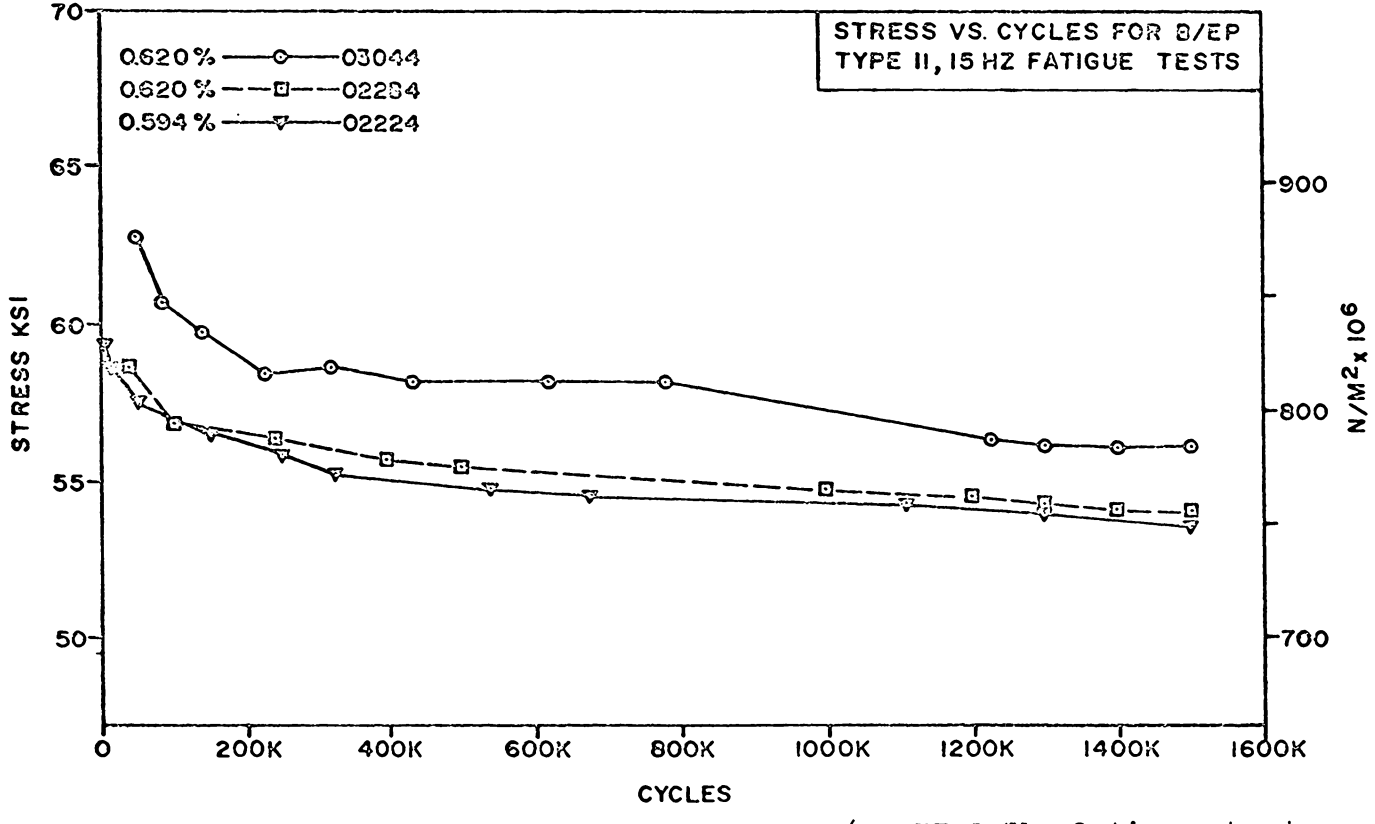

Figure 7. Stress versus cycles for B/Ep II 15Hz fatigue tests.

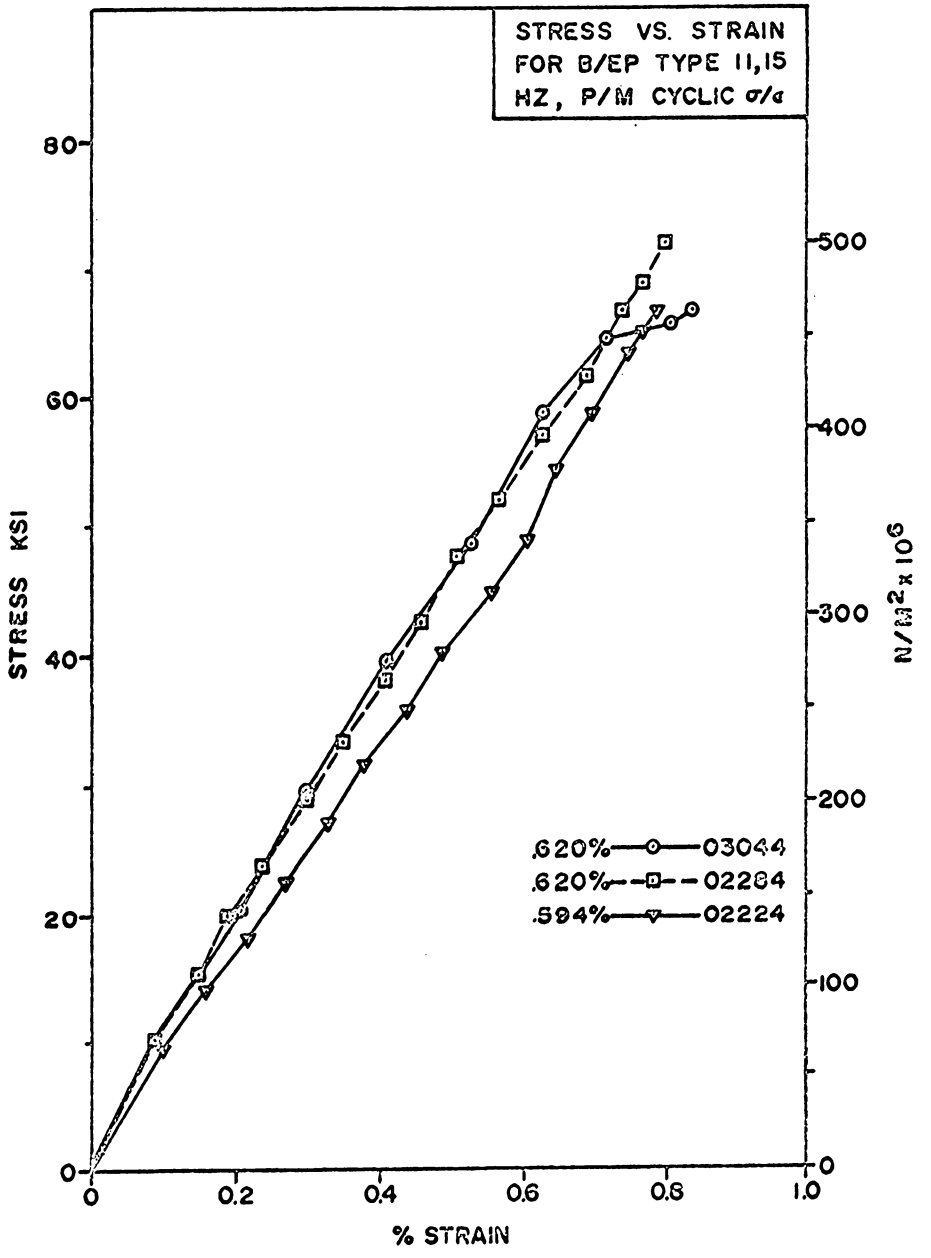

Figure 8. Stress versus strain for B/Ep II 15Hz P/M cyclic σ/ϵ tests.

TABLE I Material Parameters and Changes for B/Ep II Virgin Cyclic σ/ϵ Tests and Fatigue Tests(ϵ_r@.620%) with P/M Cyclic σ/ϵ Tests.*

Spec. No.	Type of Test	Freq. Hz.	$E_{s_{int}}$ MSI	$E_{s_{fin}}$ MSI	ΔE_s %	$C_{d_{int}}$ $psi^{-1} \times 10^{-8}$	$C_{d_{fin}}$	ΔC_d %	ϵ_{fr} %	P_{fr} lbs.	$C_{d_{fr}}$
10183A	Virgin σ/ϵ	1	11.2	--	--	--	--	--	.524	3075	9.0
10183B	Virgin σ/ϵ	15	11.4	--	--	--	--	--	.522	2800	10.5
10193A	Virgin σ/ϵ	30	10.8	--	--	--	--	--	.522	2825	10.6
10193B	Virgin σ/ϵ	45	10.6	--	--	--	--	--	.594	3000	10.7
03044	Fatigue	15	11.4	9.1	20.0	8.52	10.8	27.0	.83	2950	12.4
02284	Fatigue	15	11.4	9.1	20.0	8.55	11.1	29.8	.80	3180	11.4
02224	Fatigue	15	10.5	7.95	23.5	9.70	11.8	21.7	.79	2950	12.2
03274	Fatigue	30	11.6	9.1	21.5	8.5	10.7	26.2	.74	3300	10.8
03284	Fatigue	30	11.0	8.75	21.0	9.2	11.1	21.7	.83	3250	11.1
02204	Fatigue	30	10.6	8.2	23.0	9.6	11.9	23.9	.76	3000	11.9
02214A	Fatigue	45	10.8	9.1	15.5	9.7	11.4	17.2	.85	3120	13.5
03014A	Fatigue	45	11.1	9.1	17.0	9.5	11.3	18.9	.82	3100	11.5
03024A	Fatigue	45	10.6	9.1	14.0	9.7	11.2	15.0	.79	3100	11.5
08114	Fatigue	15	11.5	8.5	26.3	8.91	11.8	32.4	.80	2795	11.9
08124	Fatigue	15	11.0	8.9	19.1	8.77	10.8	23.1	.85	3200	11.0
08164	Fatigue	15	12.4	9.0	27.6	8.77	11.0	25.0	.79	2900	11.1
08144A	Fatigue	30	11.8	8.9	24.7	8.66	10.9	25.9	.80	3075	11.1
08154A	Fatigue	30	12.8	9.8	23.8	8.62	10.5	21.8	.85	3100	11.3
08144B	Fatigue	45	11.4	9.8	13.5	8.92	10.5	17.7	.69	2710	10.7
08154B	Fatigue	45	12.3	10.0	19.0	8.04	9.7	20.8	.84	3040	9.9
03204	Fatigue	$2\frac{1}{2}$	11.8	9.1	23.0	8.34	10.9	30.1	.69	2825	10.9

*ϵ_{min}=.120% and $R = \epsilon_{min}/\epsilon_{max}$.

TABLE II

Material Parameters and Changes for B/Al Ib Virgin Cyclic σ/ϵ Tests and Fatigue Tests(ϵ_r@.400%) with P/M cyclic σ/ϵ Tests.*

Spec. No.	Type of Test	Freq. Hz.	$E_{s_{int}}$ MSI	$E_{s_{fin}}$ MSI	ΔE_s %	$C_{d_{int}}$ $psi^{-1} \times 10^{-8}$	$C_{d_{fin}}$	ΔC_d %	ϵ_{fr} %	P_{fr} lbs.	$C_{d_{fr}}$ $psi^{-1} \times 10^{-8}$
04244	Fatigue	15	20.6	19.2	6.80	4.70	7.08	50.6	.60	2000	9.06
04254	Fatigue	15	20.0	18.3	9.29	4.47	6.78	51.7	.55	2400	8.92
04224	Fatigue	30	22.2	20.0	9.91	4.18	6.29	50.5	.56	2650	8.97
04254	Fatigue	30	18.7	18.7	0.00	4.31	6.08	41.1	.56	2900	7.69
04254	Fatigue	45	20.4	18.9	7.93	5.01	5.79	15.6	.54	2400	7.48
06194	Fatigue	45	18.8	18.4	2.60	3.89	5.09	30.8	.46	2870	7.15
07243	Fatigue	15	19.4	17.4	10.3	4.31	7.20	67.0	.43	1990	10.9
06273	Fatigue	45	20.0	18.6	6.8	4.40	5.04	14.6	.44	2580	8.48
07213A	Fatigue	45	21.8	19.0	8.3	4.18	5.26	25.8	---	----	----
12152A	Virgin σ/ϵ	15	----	----	---	----	----	----	.66	3550	----
12162B	Virgin σ/ϵ	30	----	----	---	----	----	----	.56	3625	----
03203	Virgin σ/ϵ	45	----	----	---	----	----	----	.45	2975	----

* ϵ_{min}= .120%.

TABLE III

Material Parameters and Changes for B/Al IIb Fatigue Tests (ϵ_r@ different levels) with P/M cyclic σ/ϵ Tests.**

Spec. No.	ϵ_r %	Preload Strain %	Freq. Hz.	$E_{s_{int}}$ MSI	$E_{s_{fin}}$ MSI	ΔE_s %	$C_{d_{int}}$ $psi^{-1} \times 10^{-8}$	$C_{d_{fin}}$	ΔC_d %	ϵ_{fr} %	P_{fr} lbs.	$C_{d_{fr}}$ $psi^{-1} \times 10^{-8}$
07314A	.300	.20	15	20.5	*--	--	5.23	21.7	315	--	--	21.7
07314B	.300	.25	15	19.4	*--	--	5.22	8.89	70	--	--	8.89
08024	.270	.20	15	20.9	17.7	15.3	5.21	7.76	49	.356	1235	9.92
08034	.270	.20	15	21.3	*--	--	5.02	8.44	68	--	--	8.44
08064	.250	.20	15	19.9	20.4	2.3	5.14	5.90	15	.493	2137	8.66
08104	.250	.18	15	19.4	21.1	8.6	5.14	5.59	9.0	.514	2284	8.04
08014A	.300	.20	30	19.4	*--	--	5.22	8.89	70	--	--	8.89
08014B	.270	.20	30	20.0	20.8	3.8	5.08	6.20	22	.475	1827	9.76
08044	.270	.20	30	20.4	17.4	14.5	5.29	7.22	36	.433	1482	10.6
08074	.250	.20	30	21.1	*--	--	5.06	7.16	42	--	--	7.16
08084	.250	.18	30	20.0	19.3	3.6	5.17	5.88	14	.458	2346	7.85
04294A	.400	.30	45	19.1	*--	--	4.46	7.99	79	--	--	7.99
04294B	.400	.30	45	20.4	*--	--	3.59	7.65	113	--	--	7.65
08054A	.270	.20	45	22.4	*--	--	5.04	7.80	55	--	--	7.80
08054B	.270	.20	45	20.7	17.6	15.3	5.84	7.93	36	.373	1628	10.0
08074	.250	.20	45	18.9	*--	--	5.28	10.2	93	--	--	10.2
08084	.250	.20	45	20.5	*--	--	5.24	7.85	50	--	--	7.85
08094A	.250	.18	45	20.6	20.2	1.9	5.02	5.48	11	.396	2168	7.18
08094B	.250	.18	45	20.8	18.5	10.8	5.37	6.76	26	.510	1714	11.6

*Specimen fractured during fatigue test.

**ϵ_{min} = .120%.

TABLE IV

Average Material Parameters and Changes for Fatigue Tests of B/Ep II and B/Al Ib.

Material	Freq. Hz.	E_d/E_s Init. %	E_d/E_s Final %	ΔE_s %	ΔC_d %	ϵ_{fr} %	P_{fr} lbs.
B/EpII	15	103	100	22.8	26.8	.81	2995
B/EpII	30	100	103	22.8	23.9	.78	3105
B/EpII	45	95	97	15.8	17.9	.80	3015
B/AlIb	15	111	79	8.8	56.4	.53	2130
B/AlIb	30	115	84	4.9	45.8	.56	2775
B/AlIb	45	118	96	6.4	21.7	.48	2615

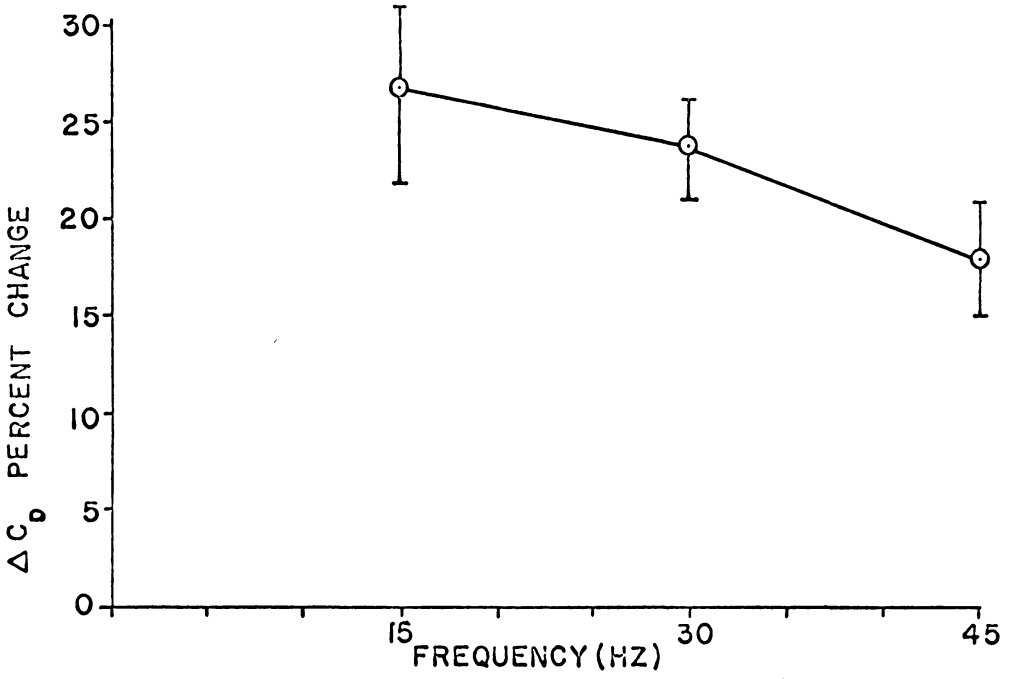

Figure 9. Change in dynamic compliance versus frequency for B/Ep II.

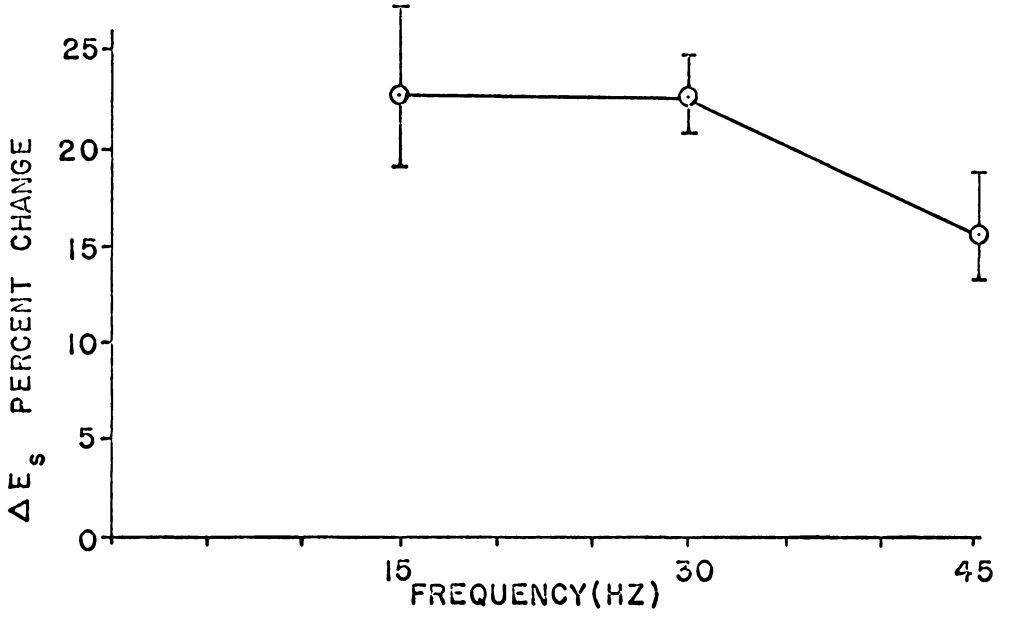

Figure 10. Change in static stiffness versus frequency for B/Ep II.

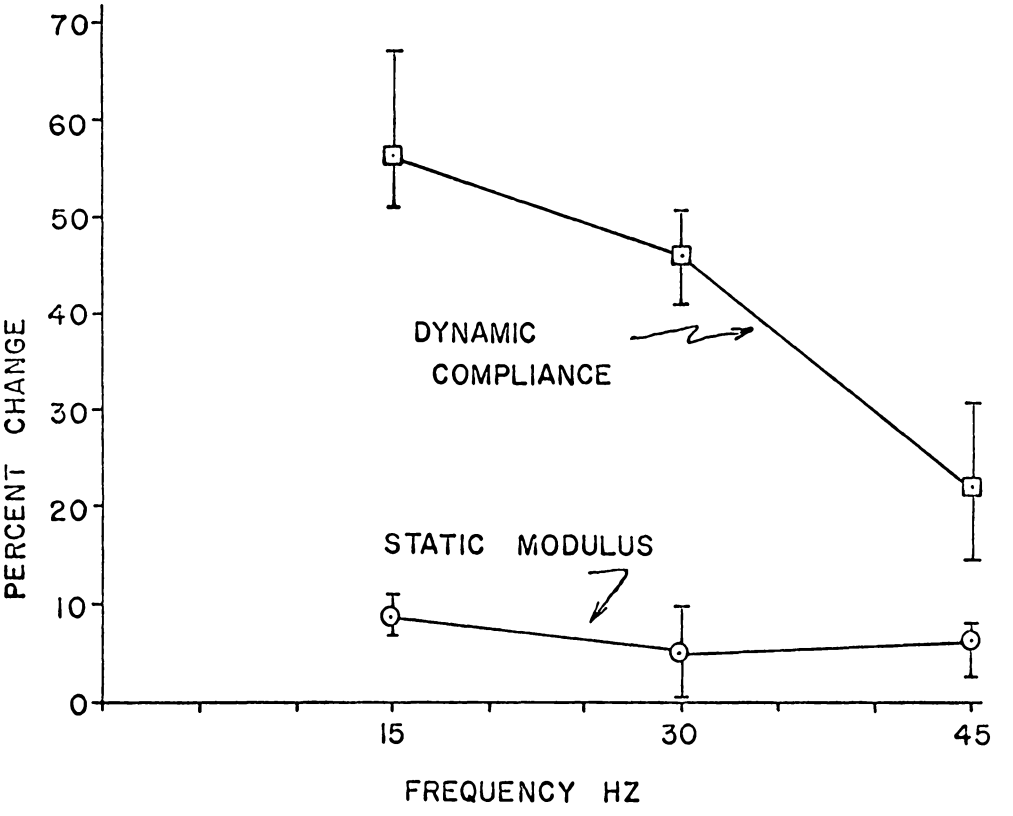

Figure 11. Change in dynamic compliance and static stiffness versus frequency for B/Al Ib.

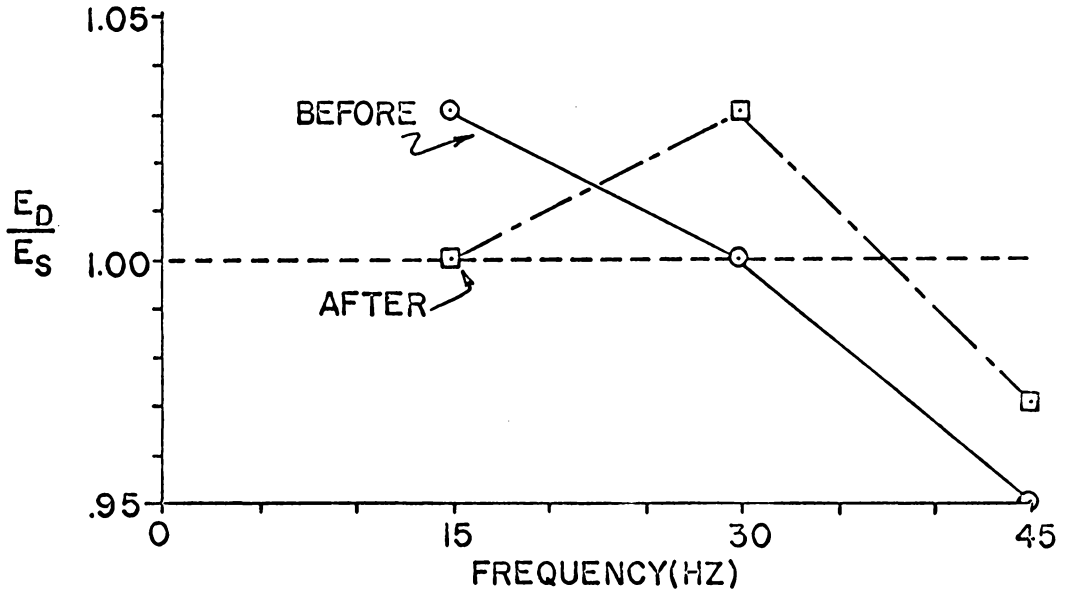

Figure 12. Ratio of dynamic to static stiffness versus frequency for B/Ep II.

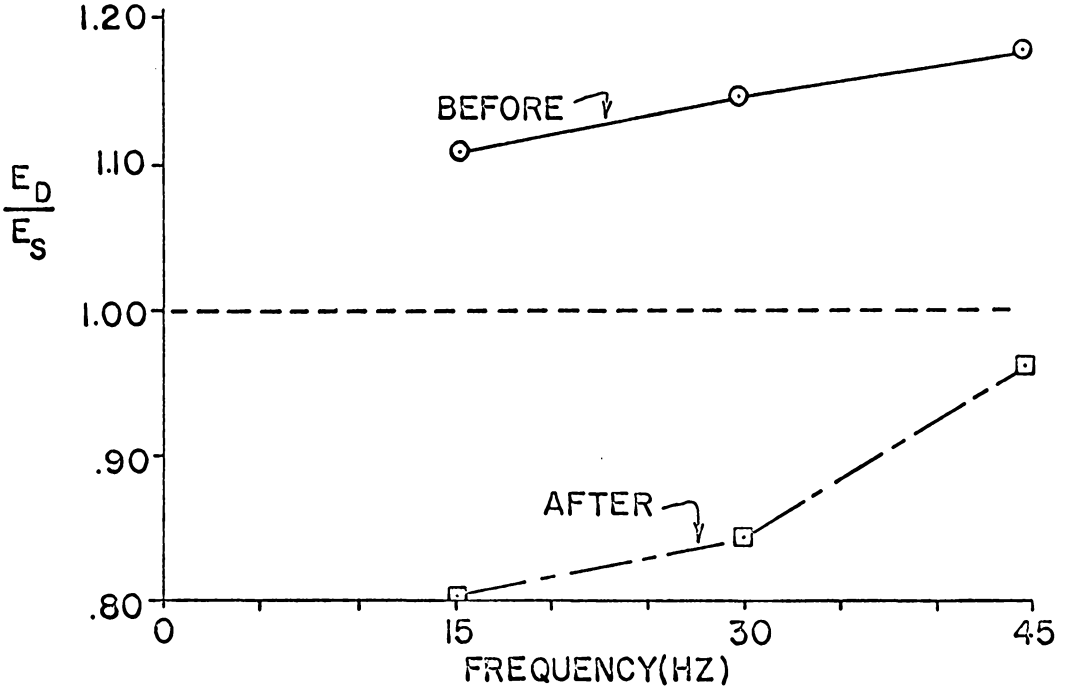

Figure 13. Ratio of dynamic to static stiffness versus frequency for B/Al Ib.

for B/Ep II, B/Al Ib, and B/Al IIb are shown in Tables I, II, and III respectfully. Average values of dynamic to static moduli ratios, percent changes in stiffness and compliance, and P/M cyclic σ/ϵ strain and load to failure data are given in Table IV for a series of B/Ep II and B/Al Ib tests. Plots of dynamic compliance and static stiffness changes versus frequency for these same series of tests are shown in Figures 9-11. The vertical bars indicate the range of values averaged. The plots of the initial and final values of the ratio of dynamic to static stiffness versus frequency for B/Ep II and B/Al Ib fatigue tests are contained in Figures 12 and 13.

DISCUSSION

Since many typical structural applications of composite materials involve stiffness designs, in many cases a more critical quantity for the determination of material failure is stiffness degradation, rather than fracture or residual strength. This is especially true for a strain-controlled situation, such as our test evironment. Although residual strength may be indicative of over all material damage, as in the case of B/Al(Table II), it can also be grossly misleading, as in the case of B/Ep(Table I). Comparing the failure stress and strain of undamaged B/Ep specimens with values of fatigue damaged specimens, with stiffness reductions of 25-30%, the values for the damaged case are from 15-30% higher than those for the undamaged case. In light of these observations, most of the following discussions of damage will be presented in terms of change of dynamic compliance.

Since one of the major goals of this experimental effort was to account for the effect of frequency on the fatigue damage mechanisms, substantial amounts of data

were taken for the purpose of isolating this effect. As evidenced by Table IV and Figures 9-13, there are definite frequency dependent fatigue damage mechanisms in both B/Ep and B/Al.

First, examining the virgin cyclic σ/ϵ data(Tables I and II), for B/Al Ib there is a very definite relationship between strain-to-failure and frequency (ϵ_f@15Hz--.66%; 30Hz--.56%; and 45Hz--.45%). The relationship is essentially linear, with 15Hz being the highest and 45Hz the lowest. This same relationship, however, does not hold for the failure stress, where 30Hz is the highest and 45Hz the lowest. The B/Ep II virgin cyclic σ/ϵ tests show very little, if any, frequency dependence. The strain-to-failure values are approximately the same for the 1Hz, 15Hz and 30Hz cases but higher for the 45Hz, whereas there are no trends in failure stresses. This lack of frequency dependence is also noted in the B/Ep P/M cyclic σ/ϵ tests, although the fatigue tests show a marked frequency dependence. For the B/Al Ib P/M cyclic σ/ϵ tests, there is also less frequency dependence, as compared to the virgin cyclic σ/ϵ tests, but the effect is still present.

The most obvious frequency effects are noted in conjunction with the fatigue tests. Frequency dependent phenomena occur for both B/Ep and B/Al composites, although the effects differ somewhat for each material.

For the case of B/Ep II, as noted in Table IV and Figures 9 and 10, there is a marked dependence of the change in dynamic compliance (ΔC_d) and the change in static stiffness(ΔE_s) with respect to cycling frequency. The percent change in dynamic compliance decreases almost linearly as frequency increases, whereas the change in static stiffness averages about the same for 15Hz and 30Hz, but decreases for 45Hz. For both materials, the ΔC_d

and ΔE_s data indicates that 15Hz is the most damaging. Due to the lengthy nature of tests run at low cycling frequencies, only several tests were run at frequencies lower than 15Hz. Therefore, because of the limited amounts of this data, it was not included in Figures 9 and 10, but the values are not significantly higher than those for 15HZ. The ΔE_s and ΔC_d values were 23.0% and 30.1%, respectfully, for a $2\frac{1}{2}$Hz test.

Shown in Figure 12 is a plot of the ratio of dynamic stiffness to static stiffness (E_d/E_s). It is interesting to note that, for the undamaged case, 15Hz is stiffer dynamically and 45Hz is softer dynamically, whereas 30Hz seems to lie at the break-point. This type of effect (structural softening with increasing frequency) has been noted for glass/epoxy beam vibration tests by Schultz and Tsai(24). They found the damping ratio ($E_d/2E_s$) to decrease with frequency up to about 500Hz, and then increase with increasing frequency for values up to 10KHz. The values of E_d/E_s after fatigue damage are also shown in Figure 12. The 15Hz tests, which suffered the greatest amounts of damage, show a decrease; but, where the amounts of damage were less, both the 30Hz and the 45Hz tests show an increase. Therefore, the effect of damage on this frequency dependent parameter is complex; indicating that small amounts of damage increase E_d/E_s, but increasing damage, beyond some point, causes a sharp decrease.

Examining other material parameters with respect to frequency, for B/Ep II the average value of specific damping($\Delta U/U$) for the fatigue and P/M cyclic σ/ϵ tests is highest for 45Hz(.10-.12), then 30Hz (.08) and lowest for 15Hz (.06). In all cases, the $\Delta U/U$ plot follows the changes in the plots of average specimen temperature and dynamic compliance; all three indicating increases in specimen dam-

age. Specimen heating due to cycling, as would be expected, was highest for the 45Hz test (ΔT-61° F); intermediate for the 30Hz test (ΔT-30° F); and lowest for the 15Hz test (ΔT -19° F). This specimen heating could be a partial explanation for the differences in E_d/E_s at different frequencies.

The frequency dependent relationships for B/Al composites are somewhat different and are summarized in Table IV and Figures 11 and 13. The changes in dynamic compliance are similar, but of greater magnitudes; whereas the changes in static stiffness are markedly different. The greatest changes in static stiffness were for 15Hz, with 30Hz the lowest and 45Hz intermediate. In all cases, the percent changes were very small (less than 10%) and in some cases nearly zero. As before, the 15Hz tests produced the most damage, and due to the length of lower frequency tests, fewer such tests were run. However, based on several low cycle fatigue tests, lower frequency tests do not seem to be substantially more damaging than the 15Hz tests.

There is also a dependence upon frequency for a change in the E_d/E_s ratio for B/Al, but drastically different from the B/Ep case. B/Al is stiffer dynamically at all frequencies, with the stiffness increasing almost linearly from 15Hz to 45Hz. After fatigue damage, the material is softer dynamically (E_d/E_s less than one) in all cases, but still becomes stiffer with increasing frequency. The change in E_d/E_s is directly proportional to damage, with 15Hz dropping the most and 45Hz the least.

There are no noticable trends with respect to frequency for specific damping or damping, but they tend to slightly higher values at higher frequencies. Since B/Al is a good conductor, there is little temperature increase during cycling; the temperature ranged from ap-

proximately 5° to 15°F above room temperature.

In the course of running these series of tests, several other effects have been noted. The most important of these is specimen conditioning, primarily the effect of static preloading before cycling and the number cycles taken to reach running conditions. Static preloading is the quasi-static loading of the fatigue specimen to a value of strain equal to or less than the maximum value of steady-state cyclic strain (for the case of a strain-controlled test). Also, as was noted in a previous section, since fatigue running conditions could not be reached consistently in several cycles, a step-loading method was used which required approximately 25K cycles to reach running conditions.

Several static tests of B/Ep II coupons with the same configuration as the fatigue specimens were carried out, resulting in values of ϵ_f=.56% and σ_f=67KSI. These values of stress and strain at failure are quite close to the average virgin cyclic σ/ϵ values of ϵ_f=.54% and σ_f=68KSI. But when fatigue tests were run at 90% of ϵ_f, very little damage resulted. To increase the amount of damage incurred during the test, the maximum running strain (ϵ_r) was increased to almost ϵ_f. The result was that some tests failed with several hundred cycles and others incurred very little damage and 'ran out'. Since some damage was noted, even at low strain levels (ϵ_r about eqaul to 50% ϵ_f), the fatigue tests were step-loaded slowly; the running strain was incremented in steps, allowing this low strain level damage to stabilize between increments. The number of cycles required to stabilize the response was only several hundred at low stress levels to several hundred thousand cycles at high stress levels. Us-

ing this strain incrementing technique (not allowing complete stabilization at high strain levels) it was possible to cycle the specimen at strain amplitudes well in excess of the static fracture strain (values of ϵ_r up to 140 to 160% of ϵ_f). For the present fatigue tests relatively quick step-loading (25K cycles total) to an ϵ_r of .620% (145% of ϵ_f) gave good repeatable tests with damage ranging from 15% to 35%, based on change in dynamic compliance.

Before fatiguing, most B/Ep specimens were preloaded to a strain of .400%; several were preloaded to lower values, and one series was not preloaded at all. Comparing the results of these tests, both fatigue and virgin cyclic σ/ϵ, shows very little difference between tests that were preloaded and those that were not. There was a slight increase in strain-to-failure in the virgin cyclic σ/ϵ tests, but very little effect was noted for the fatigue tests.

For the B/Al the behavior was markedly different. There was a strong dependence on preloading and a very weak, if any, dependence on the rate of step-loading. Although the majority of the B/Al tests were step-loaded in the same manner as the B/Ep tests, to minimize the influence of this variable for the sake of comparison, a series of earlier tests were run where the number of cycles taken to get to running conditions varied from 2K to 10K cycles. Upon examining the data, there appears to be little or no improvement of fatigue properties by lengthening the step-loading time.

B/Al is, however, quite sensitive to preloading. There is a marked increase in damage resistense noted between preloaded and not preloaded specimens. However, the amount of preload must be substantially less than ϵ_r to be most effective. For B/Al II (Table III), where the run-

ning strain was .300%, the fatigue resistense increased as the preload strain was lowered from .30%, to .25%, to .20%, and finally to .18%. The greatest effect was noted when going from .20% to.18%; this seemed to be a break-point. Further tests were not run at preload strains less than .18%, since this was not a major purpose of the investigation.

CONCLUSIONS

Based on the previous discussion, several trends can be noted and conclusios drawn. They are as follows:

1. Residual strength, as a measure of fatigue damage, is not consistently reliable, especially for the case of B/Ep during strain-controlled loading. A better indicator is the change in dynamic compliance.
2. The extent of damage development for B/Ep and B/Al is frequency dependent. As measured by a change in dynamic compliance, both B/Ep and B/Al tests indicated 15Hz to be the most damaging, with 30Hz and 45Hz developing less damage, in that order. Although the percentage changes are greater for B/Al, both B/Al and B/Ep produce almost linear plots of change in dynamic compliance versus frequency between 15Hz and 45Hz.
3. Changes in static stiffness values before and after fatigue are not indicative of the corresponding changes in dynamic compliance, especially for B/Al where the two may vary in reversed directions.
4. For undamaged B/Ep specimens, as frequency increases, E_d/E_s decreases, whereas for B/Al E_d/E_s increases with frequency.

5. Small amounts of damage in B/Ep causes E_d/E_s to increase, but large amounts cause it to decrease sharply. Damage causes E_d/E_s to decrease in all cases for B/Al.
6. B/Al is sensitive to the extent of preloading, but B/Ep is quite insensitive.
7. B/Ep is very sensitive to the length (in cycles) of step-loading, whereas B/Al is insensitive.
8. Preloading B/Al II to 35% of ϵ_r gives a marked increase in fatigue resistance.
9. By step-loading B/Ep II over 25K cycles, the failure strain can be increased by 60%.

There has been a number of significant effects noted previously. To further isolate and characterize these effects, the following future work is recomended:

-Load-controlled tests should be run at different frequencies to approximate actual loading situations.

-More low frequency tests should be conducted to investigate the effect of frequency in this range.

-A series of tests should be conducted at different preloading strains and step-loading times to further explore these effects.

-Combined frequency tests should be undertaken as a beginning to access the effects of spectral loading conditions.

CHAPTER III
SCANNING ELECTRON MICROSCOPY STUDY

Fractographs of B/Ep and B/Al are discussed in this chapter. On the basis of these data, a generalized conceptual model is developed which describes damage mechanisms and propagation associated with fatigue in these materials.

INTRODUCTION

As discussed previously, many techniques have been employed to characterize fatigue damage in fiber reinforced composite materials (FRCM). However, earlier literature does not include a definitive physical description of the microscopic damage mechanisms and their modes of propagation associated with fatigue in these types of materials.

Due to its large depth of field, the scanning electron microscope (SEM) has been quite useful in examining the jagged and irregular fracture surfaces characteristic of composite materials. A substantial part of the work in this area has been devoted to the study of processing variables encountered in the fabrication process(25,26). Other studies have examined static fractures (27-39), but relatively few have examined fatigue fractures (31). Also, many of these studies have been concerned with dicontinuously reinforced materials whose fracture mechanisms are quite different from those under present study.

It will be the purpose of this chapter to throughly examine both static and fatigue fractographs of two composite systems, similar in fiber type and layup, but drastically different in matrix properties. The end result will be a generalized conceptual model describing mechanisms and propagation associated with fatigue in FRCM.

The experimental methods used in this chapter are

those which were discussed in detail in chapter II.

DISCUSSION OF FRACTOGRAPHS

B/Al

The static fracture surface of a B/Al specimen is shown in Figure 14. The over all appearance of the fracture is quite uniform, except in the initiation region near the hole, compared to the fatigue fractures discussed later. There is essentially no debonding or delamination and in general, the matrix/fiber adhesion is extremely good. There are several cases of fiber pullout near the hole, but even in these cases there is still matrix material adhering to the fiber. There is no evidence of line voids (straight line separations in the matrix in the plane of the fibers between adjacent fibers). Throughout the entire fracture surface there is evidence of shattered fiber fractures, but only near the hole where the fracture initiated is there any fiber splitting.

Figure 15 shows the fracture surface of B/Al cycled at 15Hz. The fracture appearance is very jagged and irregular for over 60% of the fracture area emanating from the initiation at the hole. The remainder of the fracture surface (near the outer edge) is more uniform and resembles that of the previous static fracture. This demarcation in fracture appearance seems to be due to a change from fatigue induced damage to that caused by static catastrophic failure. This assumption is substantiated by observations made during the fatigue tests and the ensuing P/M cyclic σ/ϵ tests. The length of the visual surface damage incurred during cycling just prior to catastrophic failure is the same as the length of the 'fatigue damage zone' on the fractograph.

There is an extensive amount of delamination

Figure 14. B/Al Ib static fracture surface.

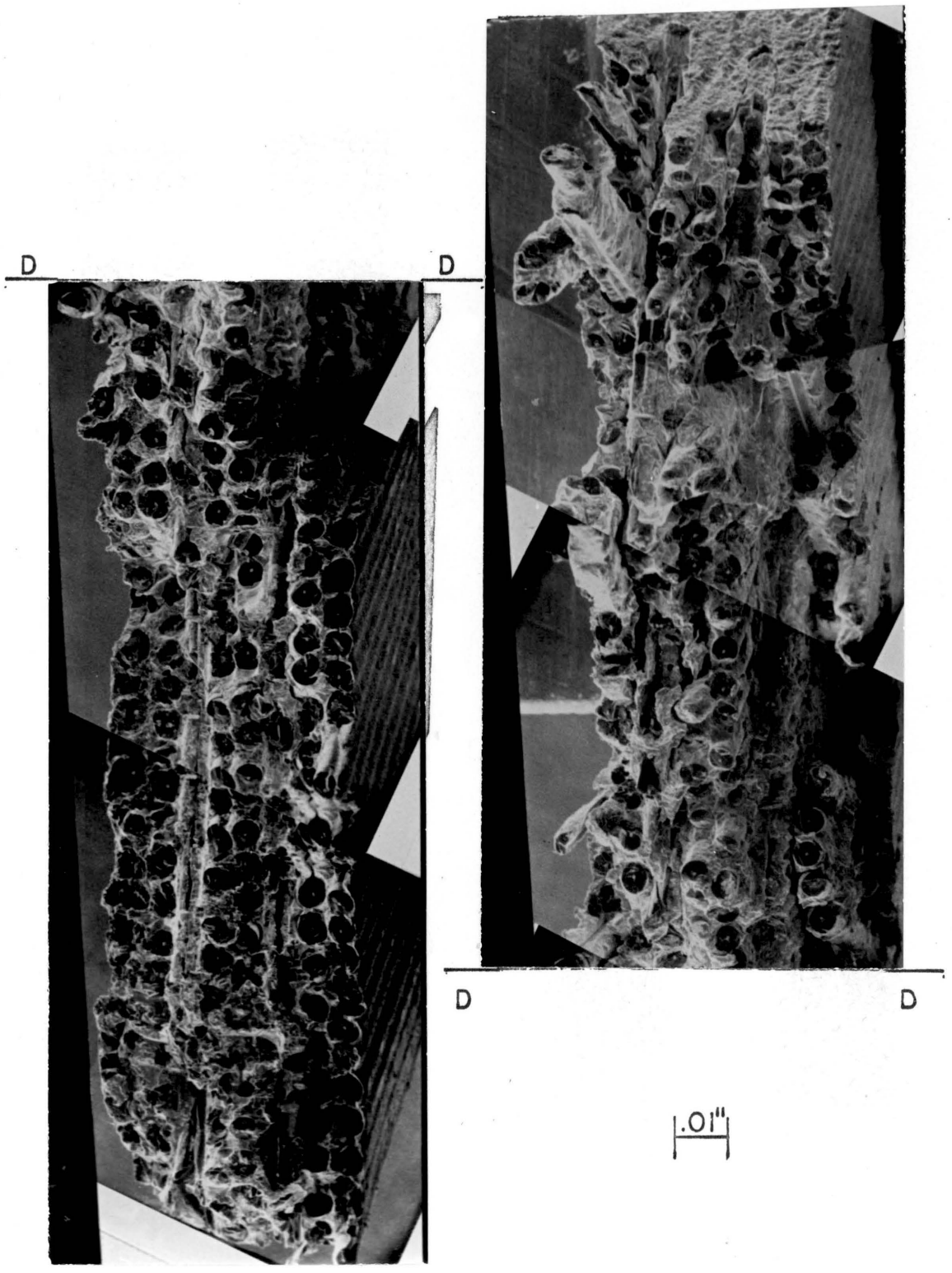

Figure 15. B/Al Ib 15Hz fatigue fracture surface.

in the fatigue damage zone, but a distinct lack of this in the static zone. These delaminations are predominately between the outter $0^{\circ}/+45^{\circ}$ layers and secondarily between the $\pm 45^{\circ}$ layers. Also, in this area there is fiber bundle pullout, especially in the outer two layers. There are significant amounts of matrix cracking in the fatigue zone and evidence of line void opening and coalesence. Although there are several instances of fiber pullout in all cases there is still good adhesion of the matrix to the fiber. Near the hole there is, again, a number of split fibers but in the fatigue zone the fractures do not appear to be as shattered-like in nature as those in the static zone.

The static zone in Figure 15 closely resembles the fracture in Figure 14. The surface is planar and there is an absence of delamination and debonding. The fiber fractures are shattered, with only one case of fiber splitting. There is one marked difference, there are line voids present and in some cases these have coalesed across several fibers. What might appear to be delamination in the -45° layer most likely is line void separation.

The fracture resulting from a 45Hz test of B/Al is shown in Figure 16. Again there is a transition be - tween the fatigue and static zones. In this case the fatigue zone comprises over 75% of the fracture. Whereas the fatigue zone fracture in the 15Hz case consisted of relatively large fiber bundle pullouts, giving a 'chunky' appearance; the 45Hz case has fewer bundles of fiber pullout and more instances of one, two, or three fibers pulling out, resulting in a rough jagged appearance. The appearance of the static zone and transition is much the same for both cases.

There is extensive delamination between all layers except the $0^{\circ}/0^{\circ}$ in the fatigue zone. The delamination

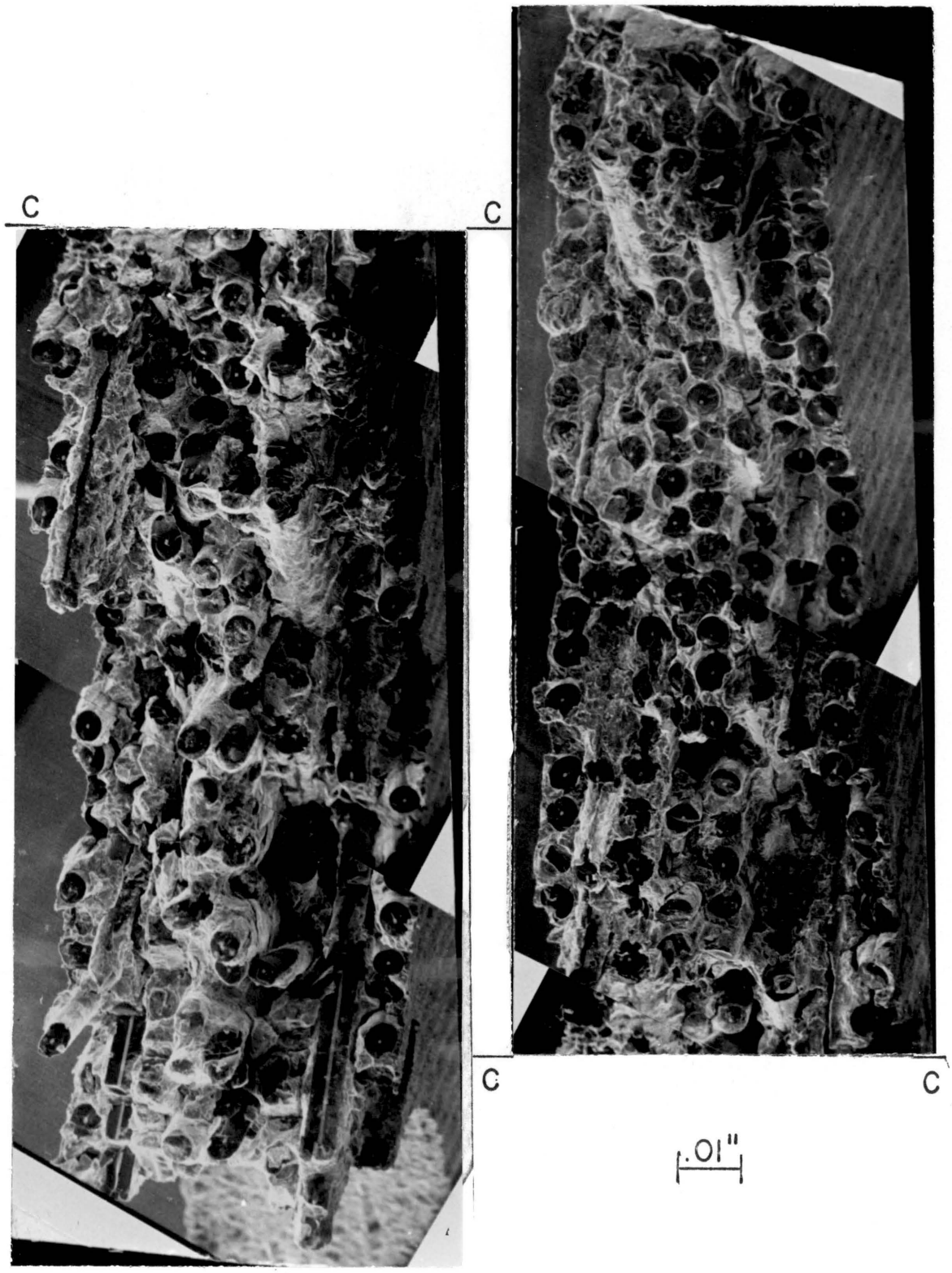

Figure 16. B/Al Ib 45Hz fatigue fracture surface.

seems most predominate between the outer $0°/+45°$ layers, followed by the $\pm 45°$ layers and the inner $-45°/0°$ layers. There is extensive matrix cracking throughout this zone. It appears, as evidenced by the somewhat fiber-contoured shape of the delamination, that the delamination process consists of a coalesence of the line voids between the fibers. Again, near the hole there is evidence of fiber splitting and the fiber fractures are less shattered-like in appearance than in the static zone.

The static zone of the 45Hz fracture is somewhat less planar in appearance than the 15Hz fracture. There are several of the $-45°$ fibers pulled out in bundles near the outer edge of the specimen. Delamination is not present, but there are numerous instances of isolated line void separations. As in all the static fractures, the fiber fractures have a shattered appearance and there is little fiber splitting.

Shown in Figures 17, 18 and 19 are fractographs of the matrix of the static test, the 45Hz test in the fatigue zone and the 45Hz test in the static zone, respectfully. The matrix of the static test is quite 'dimpled', with cupping impressions. Very closely resembling the matrix of the static case is the 'static' zone of the fatigue fracture. The static zone case has somewhat finer dimple markings than does the all-static case. By comparison, the matrix in the fatigue zone is markedly different from either the static or static zone case. The fatigue zone matrix has no dimple markings and appears to have a finer cotton-like texture. Some of this difference could well be due to rubbing of the fatigue matrix, but there is good cause to believe that this is also indicative of the extent of strain-hardening in the matrix. In the fatigue damage region, where there is greater localized straining and

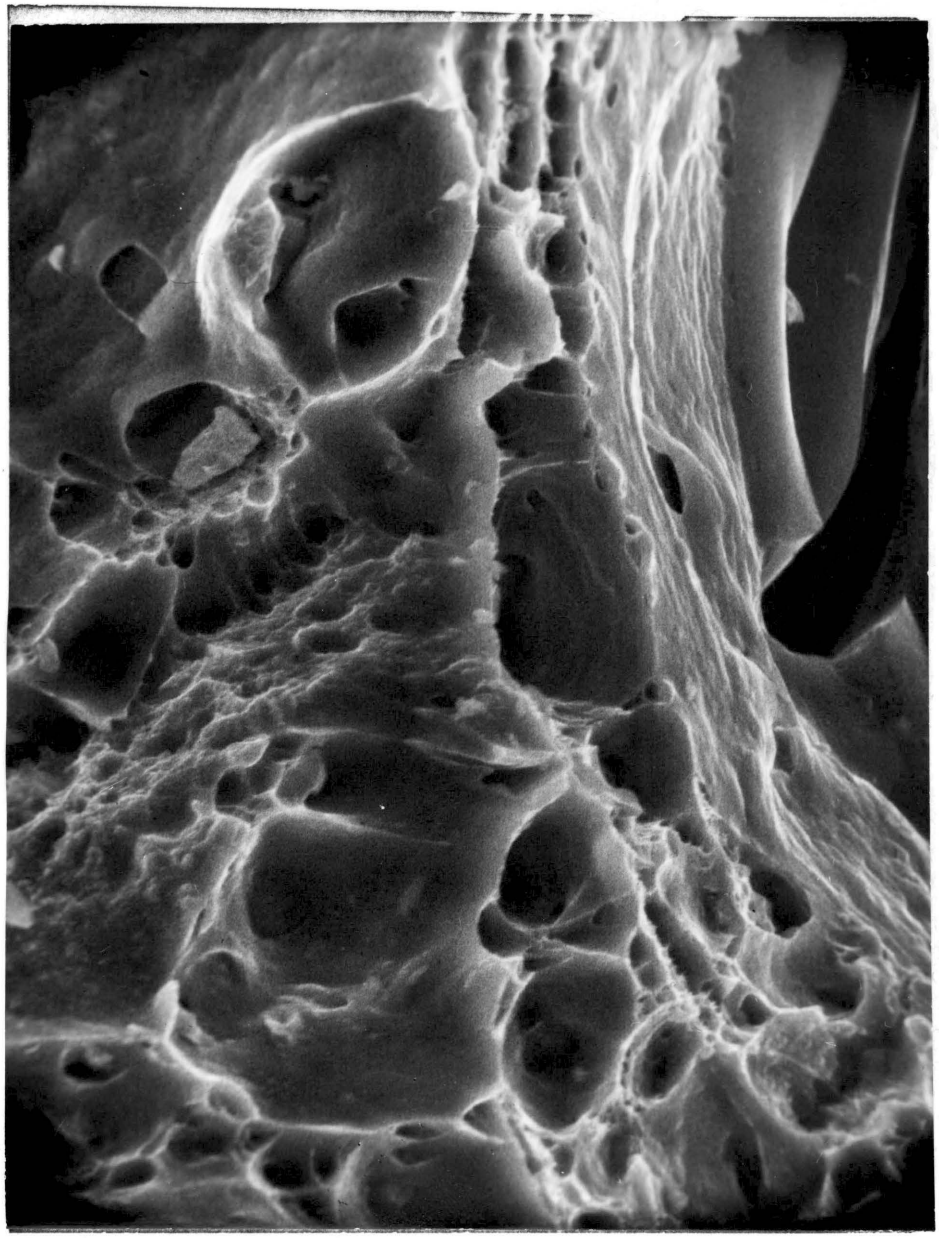

Figure 17. B/Al Ib static matrix fracture at approximately 1600x.

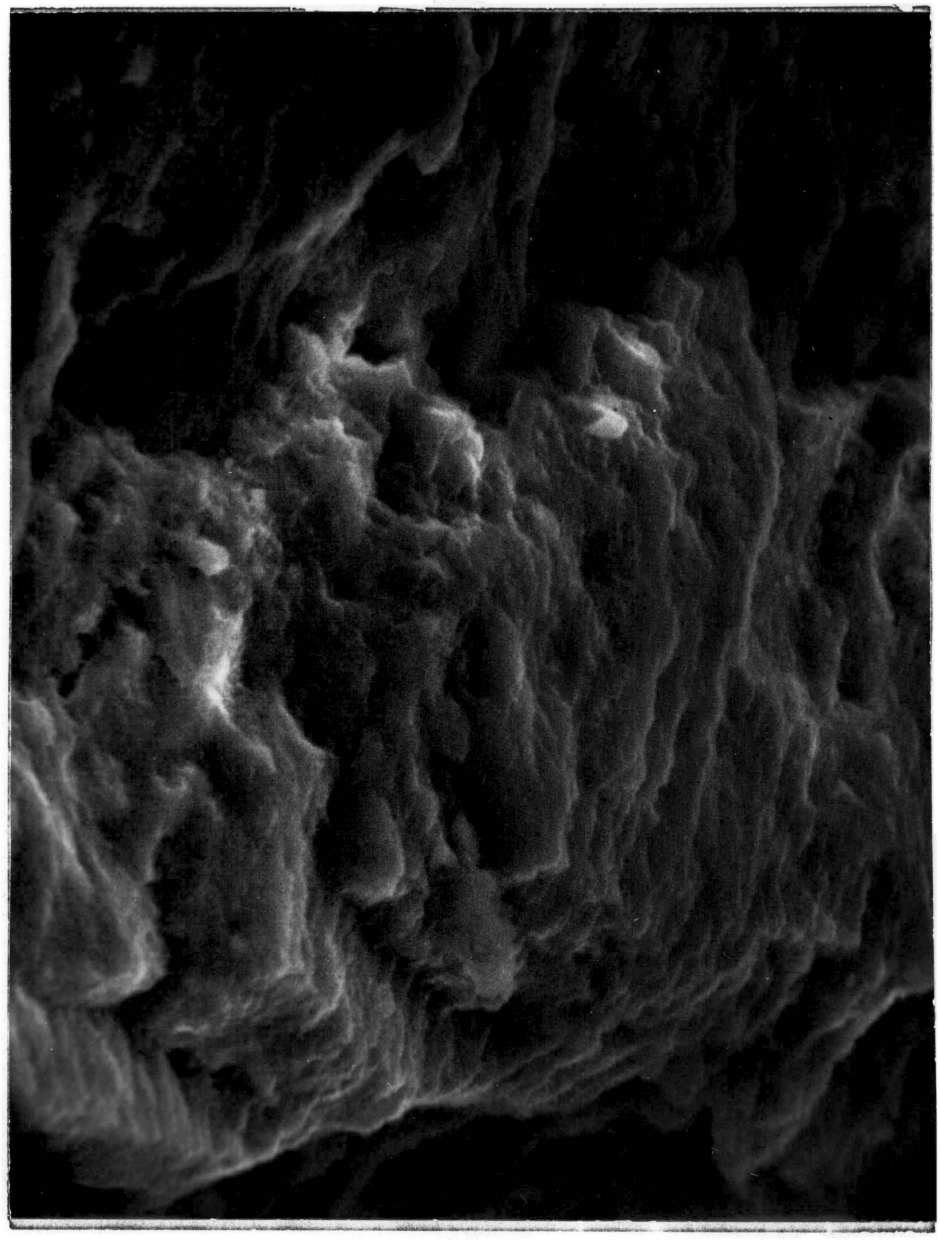

Figure 18. B/Al Ib 45 Hz fatigue matrix fracture well within the 'fatigue zone' at approximately 1600x.

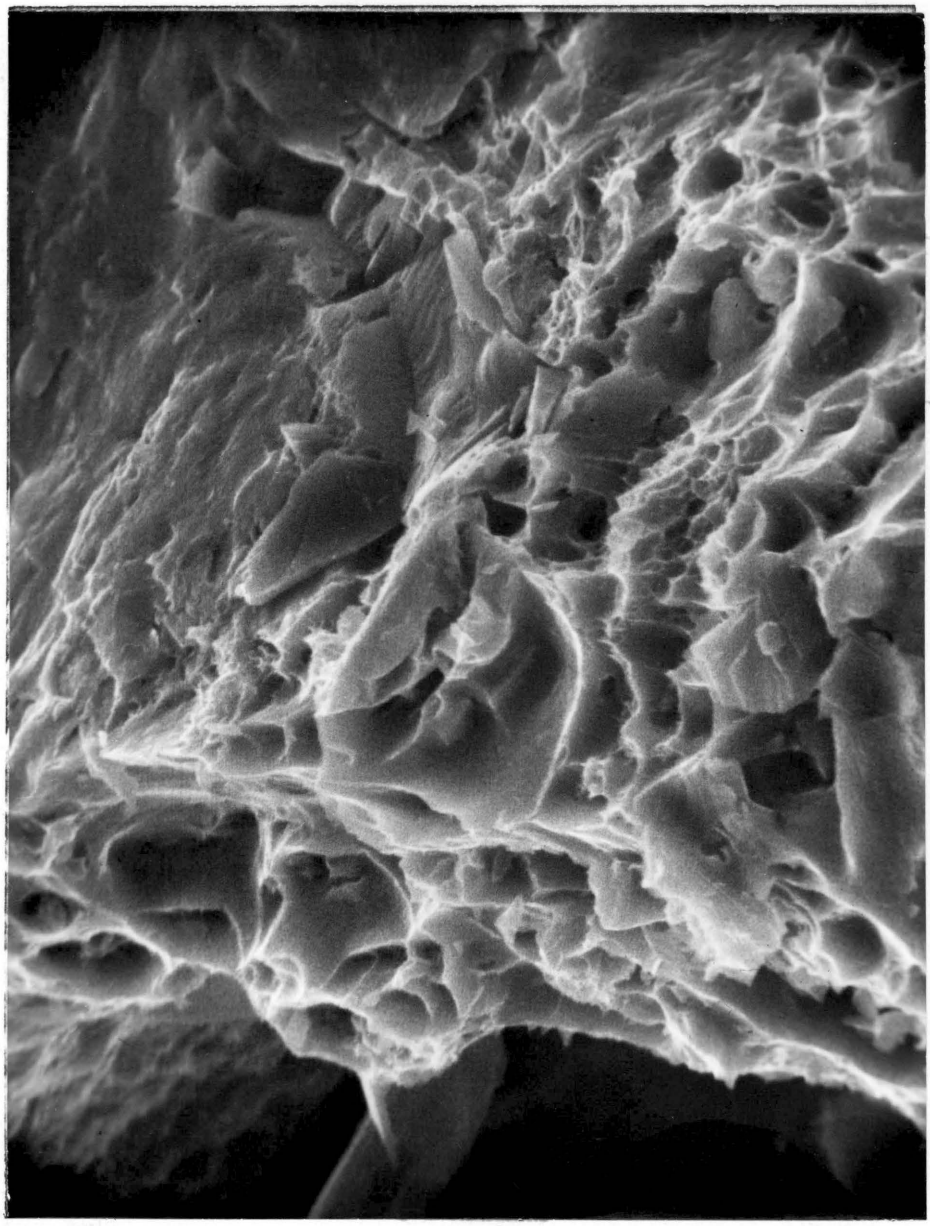

Figure 19 B/Al Ib 45Hz fatigue matrix fracture well within the 'static' zone at approximately 1600x.

TABLE V Summary of Fracture Observations for B/Al Ib.

Observation	Static Test	15Hz Fatigue Test	45Hz Fatigue Test
Over all appearance.	Uniform.	Very jagged.	Jagged.
Plane of Failure.	Uniform.	Large deviations.	Many small deviations.
Debonding.	None.	None.	None.
Fiber pull out.	Almost none, just a few near the hole.	Extensive, mostly in bundles.	Significant, but confined primarily to $\pm 45^{\circ}$ layers.
Fiber fractures.	Shattered.	Shattered in static zone, smoother in fatigue zone.	Same as 15Hz case.
Delamination.	None.	Severe in several areas, but appears to have started in $0^{\circ}/45^{\circ}$ then $\pm 45^{\circ}$.	Present in all layers, more so in $0^{\circ}/+45^{\circ}$, more dispersed than 15HZ.
Matrix.	Dimple marking, 'ductile'.	Ductile in static zone, brittle in fatigue zone.	Same as 15Hz case.

therefore more strain-hardening, the fracture is more brittle; whereas, in the static zone there is less strain-hardening and therefore a more ductile fracture.

B/Ep

A static fracture of B/Ep is shown in Figure 20. In general, the fracture surface is quite planar in appearance except in two areas. There is some amount of fiber pullout near the hole and large amounts of fiber bundle pullout (primarily in the $\pm 45^{\circ}$ layers) in the area near the outer edge. In fact, there is a distinct transition in fracture appearance about 40% of the way from the outer edge to the hole. There seems to be evidence to suggest that the fracture was initiated at two different sites, at the hole and near the edge. Other tests of these specimens have shown this material to be sensitive to edge effects.

For this static case there appears to be very little delamination and the matrix, although having some cracks, exhibits good over all structural integrity with a brittle, glassy appearance. There are substantial amounts of individual fiber debonding. Excluding the $\pm 45^{\circ}$ layers, the debond length is on the average about one or two fiber diameters (fiber diameter$\approx$4mils.) with only several instances of three or four fiber diameters (fd). There are substantial amounts of scrim cloth pullout, especially near the outer edge. Although there is no evidence in the fractographs to prove or to disprove the fact, it is quite possible that the scrim cloth influences the matrix crack initiation. The fiber fractures are less shattered than in the case of the B/Al fractographs, and many exhibit a cup/cone appearance. There are substantial amounts of fiber splitting in the $\pm 45^{\circ}$ layers near the outter edge, but only several small short sections in the more planar area towards the

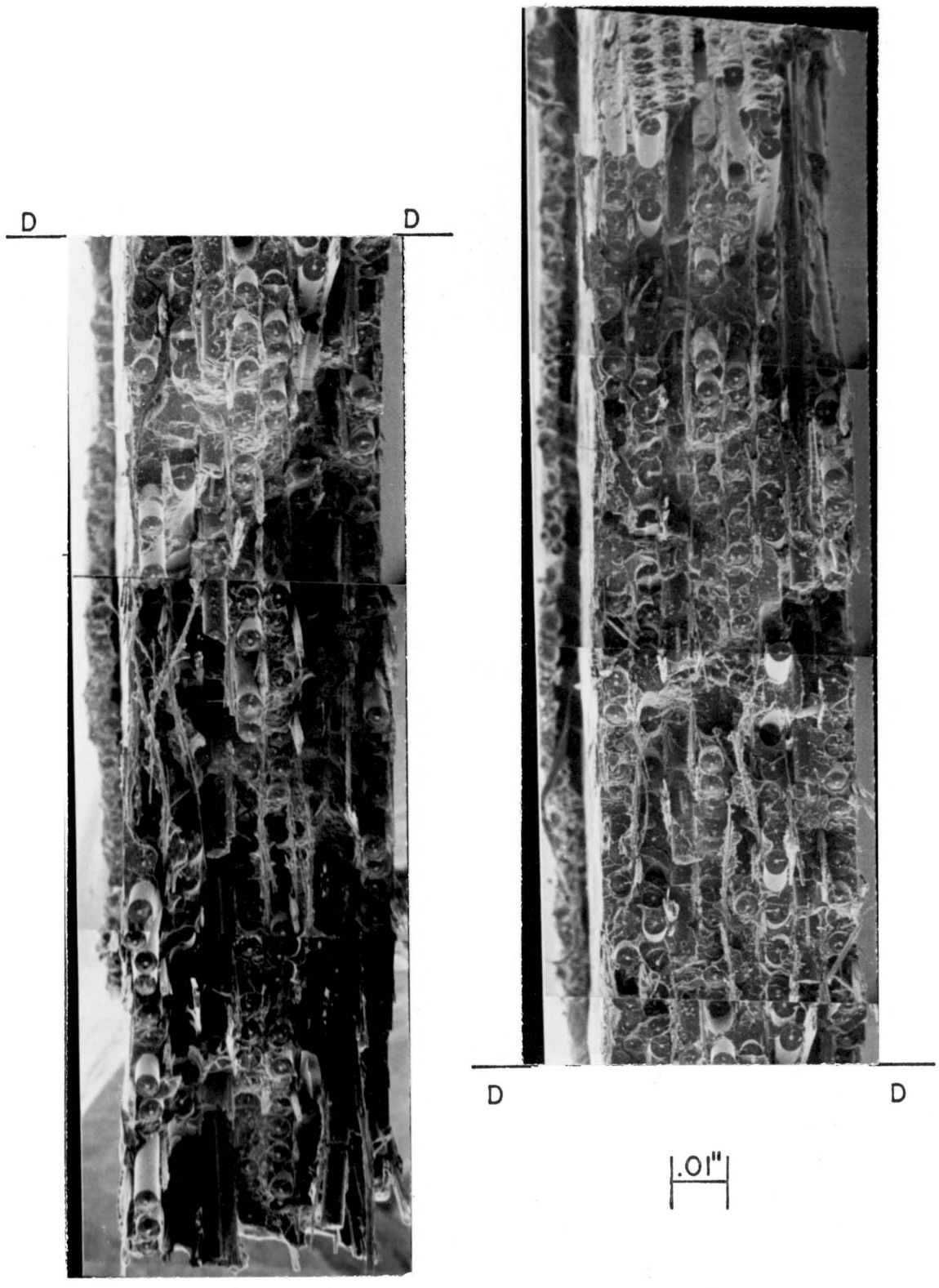

Figure 20. B/Ep II static fracture surface.

hole.

When B/Ep is fatigued it exhibits both vertical and horizontal damage emanating from the hole. The vertical damage forms an 'H' pattern with the hole located at the cross-bar. Figure 21 shows this vertical damage (0 layer is parallel to the plane of the picture) in a $2\frac{1}{2}$Hz fatigue test of B/Ep. Located in the center of this fractograph is the hole. Figure 22 is a fractograph of the same specimen showing the horizontal damage.

Considering both Figures 21 and 22, there are substantial amounts of delamination between all layers, with the $\pm 45^{\circ}$ position being the most severe case. The delaminations extend more above and below the hole than to either side of the hole. This seems reasonable considering the results of a three-dimensional finite element stress analysis (32) showing greater values of interlaminar shear in these areas. This preferential delamination is evidenced by almost no delamination at the hole in Figure 21 and amounts of delamination at the hole in Figure 23 (which shows the bottom section of the hole of a 30Hz fatigue fracture).

There are substantial amounts of fiber debonding in both Figures 21 and 22. In some areas the matrix has crumbled and fallen away from the fibers, leaving debond lengths of 20 to 40 fd. This is most evident in Figure 21. There are many instances of fiber pullout in both Figures 21 and 22, but it seems to be less severe near the outer edge of the horizontal fracture. In this area the matrix, although crumbled, has relatively good structural integrity and there is less delamination. Also, the debond length in the 0°layers is less, about one to three fd.

The fractographs of the B/Ep 30Hz fatigue test are shown in Figure 23. This view is of the horizontal damage

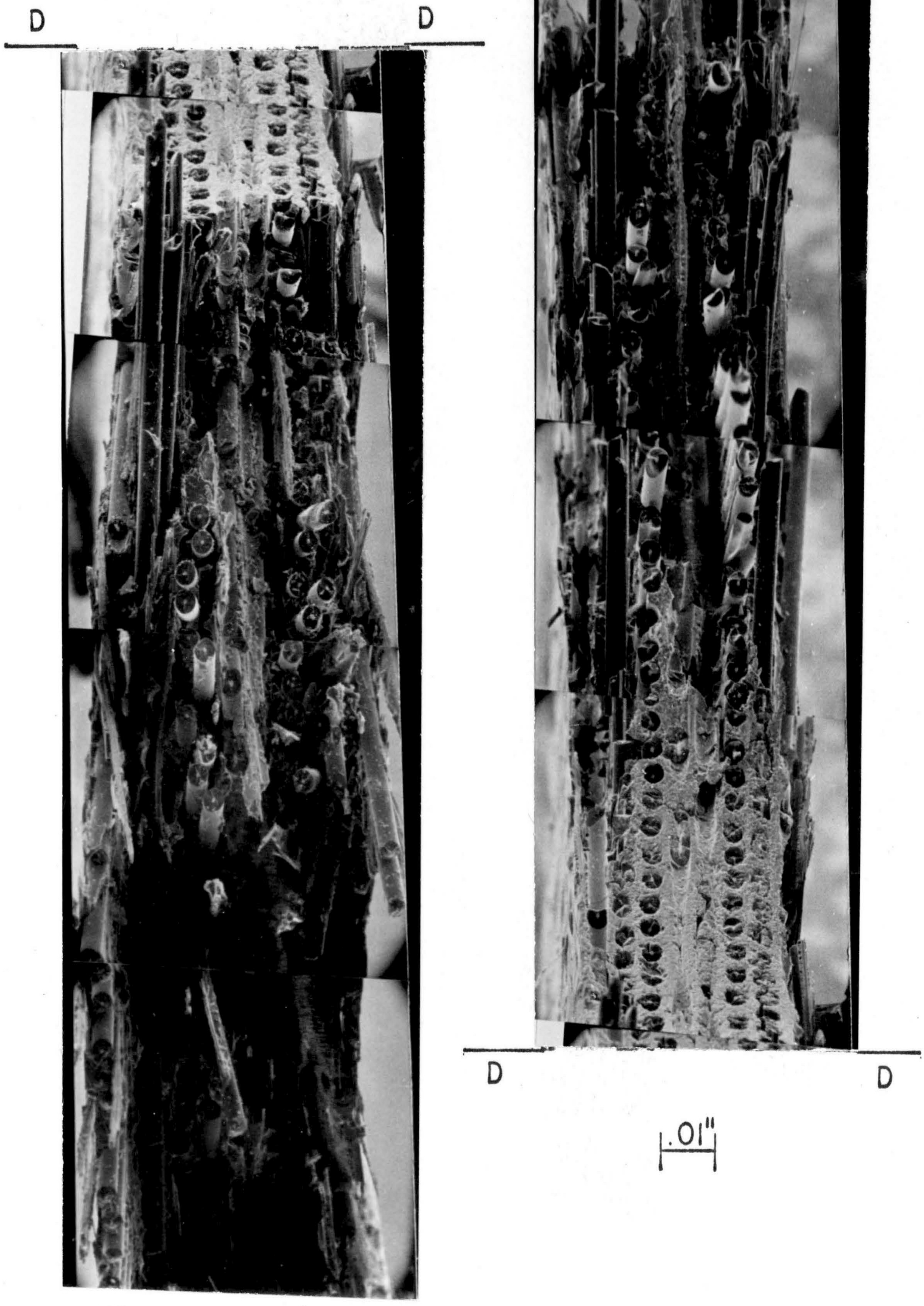

Figure 21. B/Ep II $2\frac{1}{2}$Hz fatigue vertical fracture surface.

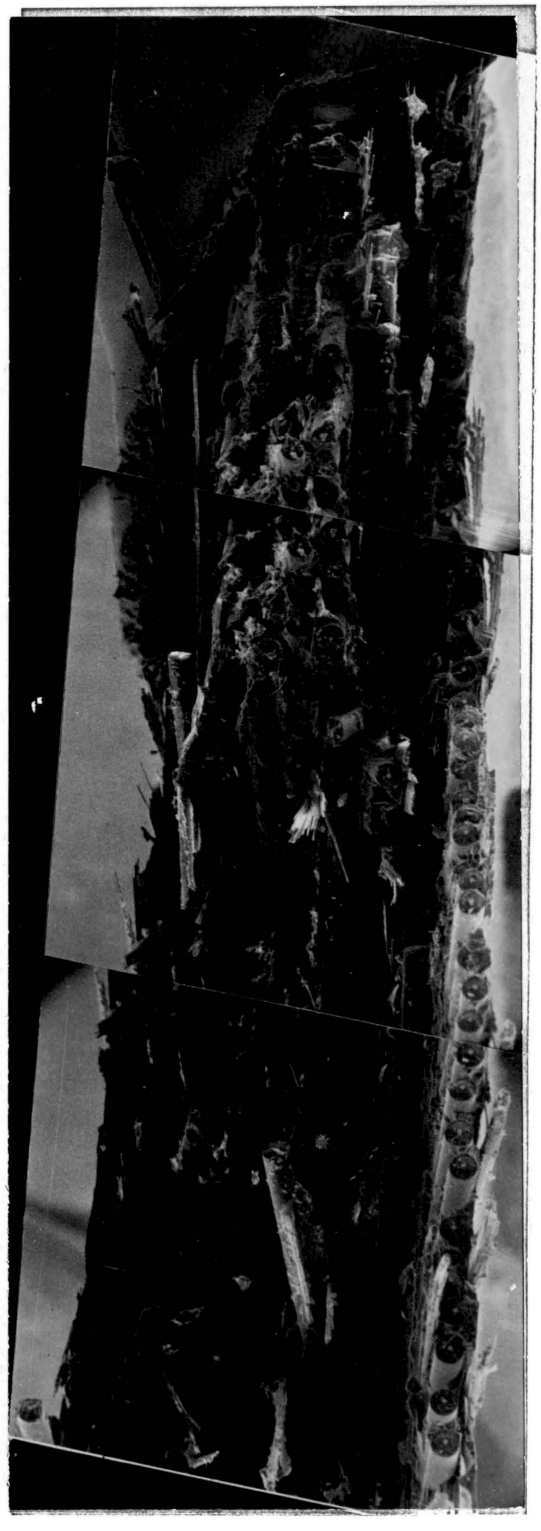

Figure 22. B/Ep II 2½Hz fatigue horizontal fracture surface.

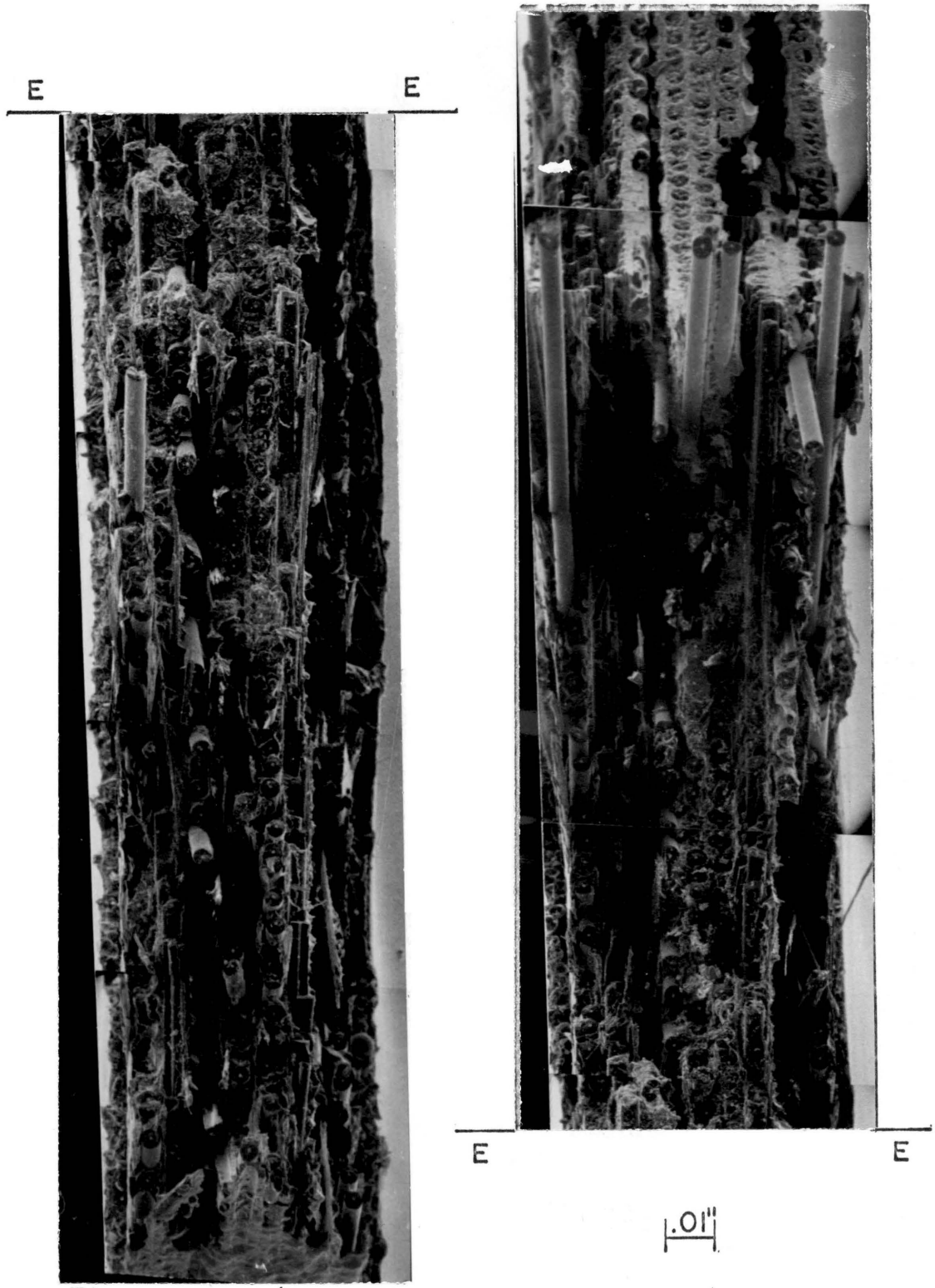

Figure 23. B/Ep II 30Hz fatigue fracture surface.

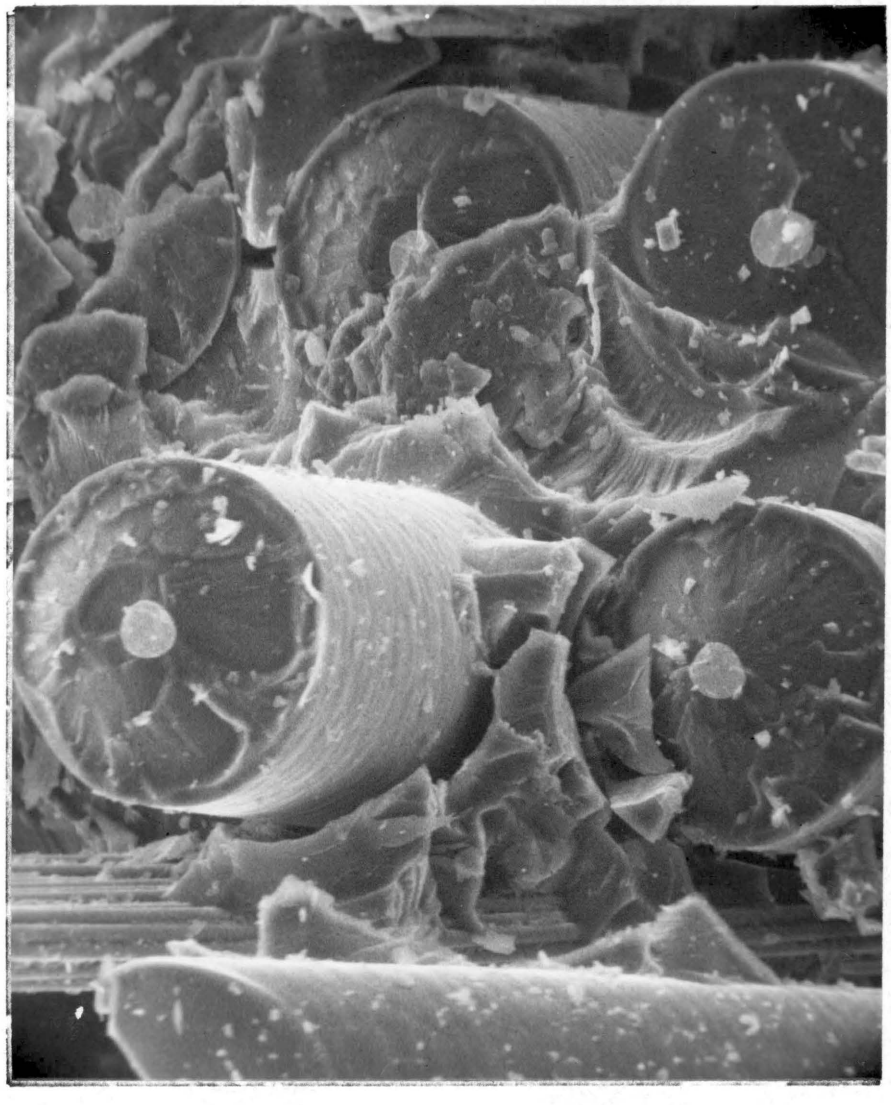

Figure 24. B/Ep II static fracture of 0-degree layers at approximately 350x.

TABLE VI Summary of Fracture Observations for B/Ep II.

Observation	Static Test	$2\frac{1}{2}$ Hz Fatigue Test	30Hz Fatigue Test
Over all appearance.	Somewhat jagged near hole and edge, rest uniform.	All very jagged.	All very jagged.
Plane of failure.	Generally uniform.	Many deviations horz. fracture, uniform wrt fibers only for vert.	Many deviations, most near hole and vert. damage extension.
Debonding.	1-2 fiber diam. (fd) in 0°, 4-5fd in ±45°.	1-2fd in 0°, up to 10fd in ±45°, and 30-40fd in vert view.	1-2fd in 0°, up to 10fd in ±45°, greatest near hole.
Fiber pull out.	Some near hole and edge in ±45°.	Bundles for horz., single for vert.	Little, some in ±45°.
Fiber fracture.	Cup & cone, not shattered.	Same as static.	Same as static.
Delamination.	None.	Extensive, all sites most in ±45°.	Worst in ±45°, some in 0°/+45° & -45°/0°.
Matrix.	Brittle, glassy.	Very crumbled and missing in vert., crumbled in horz.	Crumbled and missing near hole, crumbled elsewhere.

from the hole to the outer edge. There are large amounts of delamination, between the $\pm 45^{\circ}$ layers predominately, but also in the $0^{\circ}/+45^{\circ}$ and $-45^{\circ}/0^{\circ}$ layers. This delamination is more localized and severe than was the $2\frac{1}{2}$Hz case which was more dispersed. A distinct fracture zone transition (as seen in B/Al) is not apparent. But, there is some change in fracture appearance at about 40% of the distance from the hole to the outer edge.

Near the hole (Figure 23), where the vertical damage enters the plane of the picture, there is significant matrix crumbling and depletion. Throughout the rest of the fracture, the matrix, although still crumbled, is essentially intact (except in the immediate areas of delamination). Again, there is much debonding, and where the matrix is intact, the debond length is about one to three fd. Longer debond lengths are present where vertical damage is predominate. Fiber fractures are generally cup/cone in appearance and there is little fiber splitting, except in the -45° layers.

SUMMARY

The above results have been summarized in a fatigue damage flow chart shown in Figure 25. As load is applied to the material, the weak fibers which have break strengths on the low 'tail' of the statistical distribution of fiber strengths break at loads which may be as low as one half the mean ultimate strength. These breakages are evidenced by acoustic emissions and corresponding compliance changes. It is presumed that these weak fiber breakages act as nucleation points for the remainder of the damage development.

If the loading is quasi-static, the remainder of the fracture process is also fiber controlled and proceeds in a more or less planar through-the-thickness fashion to

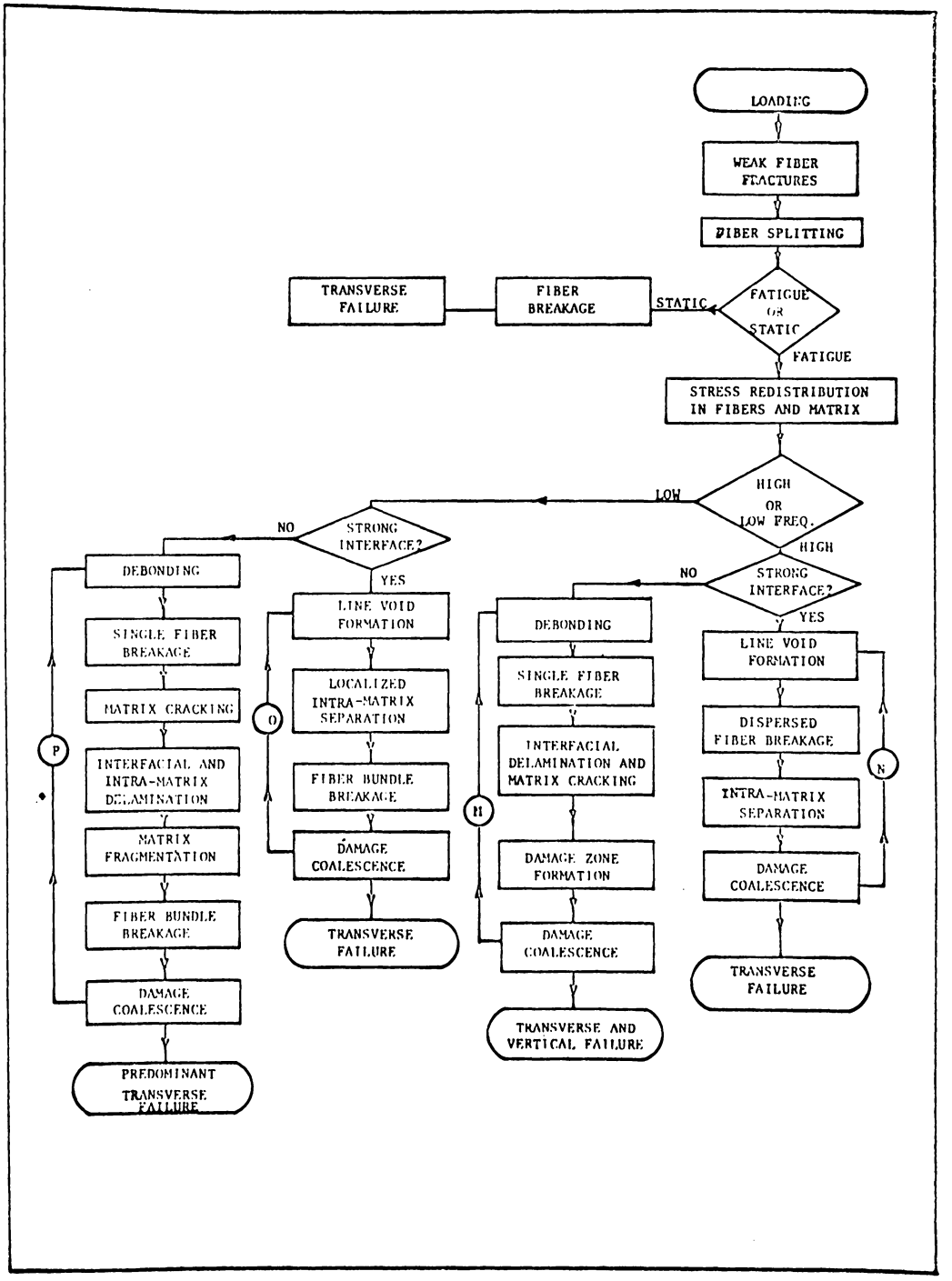

Figure 25. Fatigue damage mechanism flow chart.

produce a transverse failure.

If the load is being cycled (under strain-controlled conditions for the present case), the frequency of cycling must then be considered. Cyclic loading appears to have the effect of providing additional opportunity for other modes of damage to play an important part in the failure process. In addition to fiber breakage; debonding, delamination, line-void formation, intra-matrix separation, matrix cracking, fiber bundle breakage, damage zone formation, matrix fragmentation, and damage coalesence enter the picture as important damage modes in certain circumstances. The most salient effect of cyclic frequency is its' apparent control of the manner in which these fracture modes combine to cause fatigue damage.

As shown in Figure 25, regardless of frequency, some internal rearrangement of fibers takes place during the fatigue loading early in the test. Misaligned fibers shift slighty under load and other small changes in relative position of the constituents appear, as the internal stresses even themselves out as much as possible. This effect is most easily pictured in the neighborhood of a weak fiber breakage, but unbroken fibers move as well causing subsequent damage as will be described below.

The next highest priority item in the determination of subsequent damage is the strength of the fiber/matrix interface. In the present case, B/Al represents the strong interface system and B/Ep represents the weak interface system. For the high frequency, strong interface case, the next damage event appears to be line-void formation created by the separation of the matrix/matrix interface between the fibers in the plane of a given layer which results from the manufacturing process. This postulate is supported by the fact that the line-void is bounded not by

a crack-like fracture in many cases, but by two irregular but matching surfaces which appear to have been formed by flow of the matrix material at some time. In any case, voids do not form for distances of many fiber diameters in the plane of the fibers.

Two related events appear to follow for the high frequency case. They are dispersed fiber breakage (principally individual fibers) and intra-matrix separation. For this case, more or less isolated fiber failures seem to be accompanied by a large local matrix shear failure over some part of the broken ends of the fiber. This separation appears to proceed to failure or at least well into the plastic region over a few fiber diameters along the broken fiber, but clean debonding as such does not occur. If the matrix has strain-hardened a great deal (usually late in the test life), the chance for actual separation is increased.

Finally, in this high frequency, strong interface case, the widely dispersed damage positions begin to coalesce to form an irregular through plane of failure. These four types of damage events are looped on the flow chart in Figure 25 indicating that they probably occur in repeated sequence or concomitantly. In any case, it is not uncommon for an irregular through-plane of failure to form and 'propagate' from the stress concentrator (the hole in this case) in a roughly self-similar fashion. However, it is also not uncommon for no such plane to form for the high frequency case (i.e.--the tendency for through-(failure)-plane formation is much less than for lower frequencies, quite possibly because the highly dispersed damage does not coalesce as readily as the more local and grouped low frequency damage.

The high frequency weak interface situation is re-

presented by B/Ep in the present case. The most obvious difference between the weak interface sequence and the strong one is the appearance of debonding which plays a very important role in subsequent events. In the present case, debonding, especially in the angle plies, apparently occurs early in the test, closely followed by or together with single fiber breakage. In any case, the dominant debonding occurs over several fiber diameters. The debonding is clean with no visible matrix material remaining affixed to the fibers.

The fiber breakage and debonding is joined by interfacial delamination and other matrix cracking. Matrix crazing may occur very early in the loading sequence, but matrix cracking here will be meant to imply cracks of one fiber diameter length or longer. Delamination occurs within the first ten thousand cycles or so in regions primarily above and below the hole, as was noted previously.

Shortly thereafter, for the high frequency, weak interface case, damage zones form. These are most obvious in regions above and below the hole along lines tangent to the sides of the hole, producing the 'H' pattern refered to earlier. This vertical damage structure is easily seen on the specimen surface after a few thousand cycles in most cases and plays an important part in the final fracture. These vertical damage zones include substantial amounts of fiber breakage, debonding and delamination as evidenced by local heat development and continuous and discontinuous acoustic emission (discussed in chapters IV and V). These vertical damage zones combine with other local damage near the hole by some sort of coalescence process. Again, as indicated by the loop in the flow chart, these damage processes occur in repeated sequence or concomitantly, finally reaching combined severity sufficient

to cause fracture or major damage. In many cases, the final fracture is, in fact, along vertical planes up to the grip region where transverse separation finally does occur.

Low frequency, strong interface situations are represented by the 15Hz test on B/Al. Line-voids form and there is localized intra-matrix separation as there is for the high frequency case. However, these damage events do not occur in such a dipersed manner but in more concentrated groups. The result is the formation of bundles of fiber breakage, including a half dozen fibers or so. These bundles break and separate causing large local damage zones, including major delaminations. The coalescence does not produce an even planar failure, the final fracture being transverse to the load axis, but very jagged and irregular. The damage tends to be generally more severe than the high frequency case.

The weak interface, low frequency situation is represented by the 15Hz B/Ep tests. Single fiber breakage and debonding occur as in the weak interface, high frequency case. However, a much more severe sequence of matrix cracking, interfacial and intra-matrix delamination, matrix fragmentation, and fiber bundle breakage follows. The failure 'plane' is transverse and extremely irregular with large chunks of matrix missing after fracture.

A summary of these and other related fracture surface observations appears in Tables V and VI. For these fairly high-strain-amplitude tests, low frequencies of testing seem to cause the most severe gross damage. High frequency testing enhances the part played by dispersed individual events. There is decreased tendency for development of through-planes of failure for both strong and weak interface material systems (B/Al and B/Ep) at high frequencies.

In most cases, the exact chronology of the damage modes identified previously has not been established. However, even a casual examination of the fractographs leaves little doubt that frequency of testing can have a major influence on damage development. An explanation of these frequency effects has not been well established. However, it has been observed in polycrystalline (uniform) metal specimens that under high frequency (and/or high temperature) loading, crack propagation tends to be inter-granular while at low frequency (and/or low temperature) cracks tend to propagate in intra-granular fashion (1). Such behavior is certainly consistent with the present data, wherein damage tends to develop along the fibers at high frequencies and through them for low frequency loading. Although the basic reasons for such behavior are just beginning to unfold, some conjectures can be made at this point.

One useful observation is that if a single fiber breaks, there is a finite increment of time during which the strain energy release caused by the fracture takes place. That release provides a driving force for propagation of the crack in a direction which releases the most additional strain energy (i.e.,perpendicular to the load direction). If the load is quickly reduced, however, the driving process is quickly interrupted and a smaller region is affected by a single fiber failure, giving rise to a more dispersed damage as seen in the 45Hz tests.

Another line of reasoning comes about on the premise that there is a region of deformation just ahead of the crack tip for any matrix crack which is rate controlled. For the aluminum matrix, the plastic enclave is that region, since plastic flow is a rate controlled process commonly described by the Arrhenius equation. For the epoxy matrix, some nonlinear flow at the crack tip is assured, possibly encouraged by high local temperatures caused by a

fiber breakage. In any case, if such a region exists, low cycling frequencies will provide more time-at-load and therefore allow more deformation to occur in that region. That deformation will follow the local stress field, which will favor self-similar growth in the transverse direction. Higher frequencies of loading will provide less time-at-load, less stress-controlled deformation, and less tendency for self-similar propagation of a crack or defect. Instead, the defects will grow or spread by a combination of elastic cracking and coalescence (i.e., they will tend to follow the line of least resistance). For a crack approaching a fiber, that line is the fiber/matrix interface, especially for B/Ep.

In general, then, these tentative arguments support the view that frequency dependence comes about because of local time dependent processes that occur at individual failure events. Since the global response of the specimens is controlled by the fibers, which do not display any such time dependent behavior, these processes are thought to occur in the matrix material. Frequency of cycling controls the opportunity for these processes to develop by controlling the time-at-load, and the degree of developement controls the manner in which fatigue damage is generated as previously described. Obviously much additional investigation is needed, but these arguments will serve to provide at least some intuitive guidance. In particular, the idea of local rate-controlled processes controlling the selection and combination of damage modes to produce frequency dependent fatigue damage does remove the conceptual conflict of those effects with the fact that very little time dependent response of these materials is observed during static loading, under otherwise identical conditions.

CHAPTER IV
ACOUSTIC EMISSION INVESTIGATIONS

In this chapter the experimental relationship between acoustic emission and fatigue damage is examined. A good correlation between acoustic emission and structural damage is obtained, which leads to the developement of an energy-based failure model.

INTRODUCTION

Because of the complex structural nature of composite materials, characterizing and measuring the damage processes during cyclic loading is quite challenging. Compared to homogeneous materials, where damage can be characterized as the propagation of usually one crack, composite materials exhibit several major damage mechanisms which can progress independently or in interaction with each other. As mentioned earlier. these mechanisms include matrix cracking, interfacial debonding, delamination, and fiber breakage.

In order to apply any form of fracture analysis and/or predictions, it is first necessary to establish an experimental parameter with which theoretical results can be compared. In the case of homogeneous materials, the clearly visible propagation of a through-crack is the measure of damage, in the form of the change in crack length, Δl. This data can then be correlated with various theories, most of which are similar to that after Paris (34),

$$\frac{dl}{dn} = c(\Delta K)^m \quad \text{.....eq.(1)}$$

Where l is the crack length; n, the number of cycles; c, a constant containing other material parameters; $\Delta K = K_{max} - K_{min}$, the diference between the stress intensity factors at maximum and minimum loads; and m, a constant denoting

the log-slope of the data, which is usually between 2-6. For composite materials, since there are at least four major distinct damage mechanisms, it is difficult to determine which mechanisms dominate, let alone experimentally measure them. It has been the observation of the present investigator that damage usually propagates by the spreading and advancement of a 'damage affected' zone, in the case of a specimen with a geometrically induced stress concentration, such as a hole in a plate(21). Therefore, it is obvious that an experimental method is needed to characterize the extent and propagation of this damage zone.

Different methods have been used to attempt to characterize this process. Some of these are visual surface observations, ultrasonic attenuation measurements, thermal emission patterns, and acoustic emission measurements. Each of these methods have their advantages and disadvantages.

Visual surface observations, although sometimes indicative of over all specimen damage, based a static residual strengths and change in over all specimen stiffness, can be misleading. For fatigue tests of B/Ep coupons with a hole, it has been observed that some specimens, although showing extreme surface damage, have undergone little degradation of over all mechanical properties. Therefore, as evidenced by the three-dimensionality in structure of composite materials, two dimensional surface observations can not be treated as a reliable measure of over all damage.

Ultrasonic attenuation measurements, although they may be a useful tool in detecting damage (35), presently are not practical as a device to measure the propagation of damage. Due to the extremely thin nature of structural composite panels (usually less than 0.10 inch), a quartz

block must be bonded to the panel to separate the pulses for electronic analysis. The test, therefore, must be stopped, the specimen removed from the grips, the quartz block bonded, and the measurements performed periodically during the test. For most testing situation this is not desirable or practical, since the nature of the test could well be altered during the stopping and starting of the test. Also, since the transducer and the quartz block must be rebonded for each measurement, there is a large source of experimental error due to the inherent variability of the bond.

Thermal emission data, in the form of real-time video thermography, has had recent applications with promising results (36). It provides a two-dimensional pictorial (averaged over the third dimension) view of damage, that has been correlated with the mode of failure in several composite materials. It does have its disadvantages in that the data must be analyzed and interpreted before an experimental parameter can be extracted (This will be discussed in more detail in chapter V.).

Acoustic emission has received a great deal of attention as a measure of damage in homogeneous materials (37). By comparison to the number of those investigating quasi-static induced damage, relatively few have investigated fatigue propagated damage; and even fewer have looked at the phenomena in composite materials. It will be the purpose of this chapter to investigate the relationship of acoustic emission to damage measurement and propagation in composite materials subjected to cyclic loading.

ACOUSTIC EMISSION PRINCIPLES

The basic premise of appling acoustic emission to detecting the extent and propagation of damage in a struct-

ural material is when a damage event occurs (such as matrix cracking, debonding, delamination, fiber breakage, etc.), there is a characteristic release of energy, primarily in the form of acoustic, thermal, and exo-electronic emissions. By bonding a piezoelectric transducer to the specimen, the acoustic signals can be detected, electronically processed and then recorded; therefore, giving a permanent record of damage events throughout a given test. The usual procedure is to count the number of pulses that cross a preset amplitude threshold. The number of counted pulses indicates the extent of the damage and the count rate indicates the rate of damage propagation.

As mentioned previously, there are four major damage mechanisms: matrix cracking, debonding, delamination, and fiber breakage. It has been stated by several investigators (38) that the magnitude of the acoustic emission signal emitted by fiber breakage is greater in magnitude than those generated by delamination, debonding, or matrix cracking. But, depending upon the material and damage circumstances delamination and debonding may cause relatively large acoustic signals. Since the acoustic signals are characteristically compound decaying sinusiodal waves, large amplitude emissions will contribute more counts per event because the decaying oscillations will be counted before they are attenuated below the amplitude threshold. Therefore, fiber breakage characteristically should generate more counts than delamination, debonding, and matrix cracking. The over all result would be that the acoustic emission count is 'weighted' more towards fiber breakage, delamination, debonding, and matrix cracking, in that order. And in light of the present understanding of the severity of these fracture mechanisms, this does not appear to be undesirable.

EXPERIMENTAL METHODS

A detailed discussion of the experimental methods can be found in chapter II, including a description of the final version of the acoustic emission system used. Since the modifications to the acoustic emission (AE) system are related to the discussion of the data, they will be detailed in this chapter.

Acoustic emission was monitored by two types of systems. The modified system incorporated a programable gate, sample rate and readout (Figure 3). With this system it is possible to look at the A.E. over a specific part of the loading function. The normal practice was to look at acoustic emission generated only during the top half of the loading signal. By doing this, acoustic emission generated at and approaching high stress levels where new damage is most likely to occur is recorded and the acoustic emission generated during unloading and at low stress levels, where damage is least likely, is not. In this manner, specimen fretting and machine noise is most likely rejected. Also, this system provided the option of recording totalized acoustic emission or acoustic emission rate averaged over relatively long periods of time (10sec-5min). By means of an FM tape recorder, selected portions of actual acoustic emission signals can be recorded for further analysis.

The original system was the same as the modified system except that it did not provide any programable features. The output was always in the form of a non-gated acoustic emissionrate per ten second interval.

Both systems used a broad- band Panametrics acoustic emission transducer with a center frequency of 100KHz. This signal was then amplified 60db by a Panametrics preamp incorporating a band-pass filter tuned to 80KHz-300KHz.

This signal then passed through a Tektronix differential amplifier set for a band-pass of 10KHz-300KHz, to eliminate transmission noise. This output was then processed by a Hewlett-Packard programable counter and its output channeled through a D/A convertor to several analog and digital recording devices.

RESULTS AND DISCUSSION

The results of a strain-controlled 30Hz fatigue test of B/Al are shown in Figure 26. This Figure shows the acoustic emission rate and total plotted with the remote stress versus cycles. Since the test is run at constant strain amplitudes, the resulting decrease in stress in indicative of a reduction in stiffness or an increase in compliance, therefore a measure of over all specimen damage. During the first 400K cycles there is very little A.E. and accompanying there are correspondingly small fluctuations in stress. At about 400K cycles there is a gradual rise in A.E. whille the stress increases. This A.E. is believed primarily due to micro-cracking in the aluminum matrix during a strain-hardening process, with smaller contribution from weak fiber breakage. There is a sharp rise in A. E. at 800K cycles and at 1M cycles and likewise sharp decreases in stress. The A.E. seems to peak around 1M cycles where the stress drop is most severe. After this the stress continues to drop, but at a lesser rate and a corresponding decrease in A.E. rate is noted up until 1.4M cycles. At 1.4M cycles there is again a very drastic drop in stress and this is met with a sharp increase in A.E. At 1.525M cycles the test was stopped. Also, at about 1M cycles there was noted visual extension of surface damage which seemed to stop or slow down until about 1.4M cycles, when the damage on the right side of the hole propagated

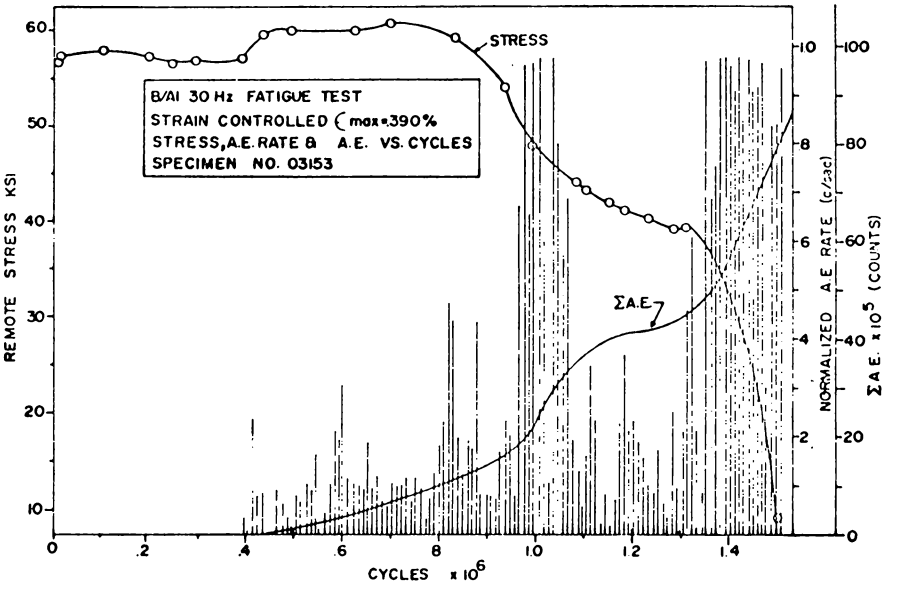

Figure 26. Stress and A.E. versus cycles for 30Hz B/Al.

through the thickness and almost all the way to the free edge.

Figure 27 shows the same type of test as that in Figure 26 except the specimen was cycled at 45Hz instead of 30Hz. A plot of compliance is also shown for comparison with the stress curve. Between start up and 300K cycles, where the stress is decreasing rapidly (after a small amount of strain-hardening) and the compliance is increasing, there are corresponding high rates of A.E. Between 300K and 700K cycles, where the rate of increase in compliance and the rate of decrease in stress decreased, there is a marked decrease in A.E. rate. Also during this period, the visual damage, noted in the few 100K cycles, seemed to arrest itself. At 800K cycles an abrupt increase in surface damage was noted, accompanied by increases in A.E. rate and compliance and a decrease in stress. The compliance continued to increase and the stress decreased at slower rates between 900K and 1M cycles when the test was stopped. During this period the A.E. rate was still high, but tending to decrease in correspondence with compliance and stress. This somewhat higher-than-expected A.E. at the end of the test is most likely due to specimen fretting and scraping caused by the large amounts of damage present. Upon viewing the A.E. signals on an oscilloscope, they were found to be periodic in nature, with the frequency of occurance approximately the same as the test frequency, 45Hz. It should be noted that for this test and all others, with the exception of those shown in Figures 34 and 35, the acoustic emission was monitored using the system without any programable features, such as gating.

A 15Hz strain-controlled fatigue test of B/Al is shown in Figure 28. This curve shows good correlation between A.E. rate and stress drop during the first 400K

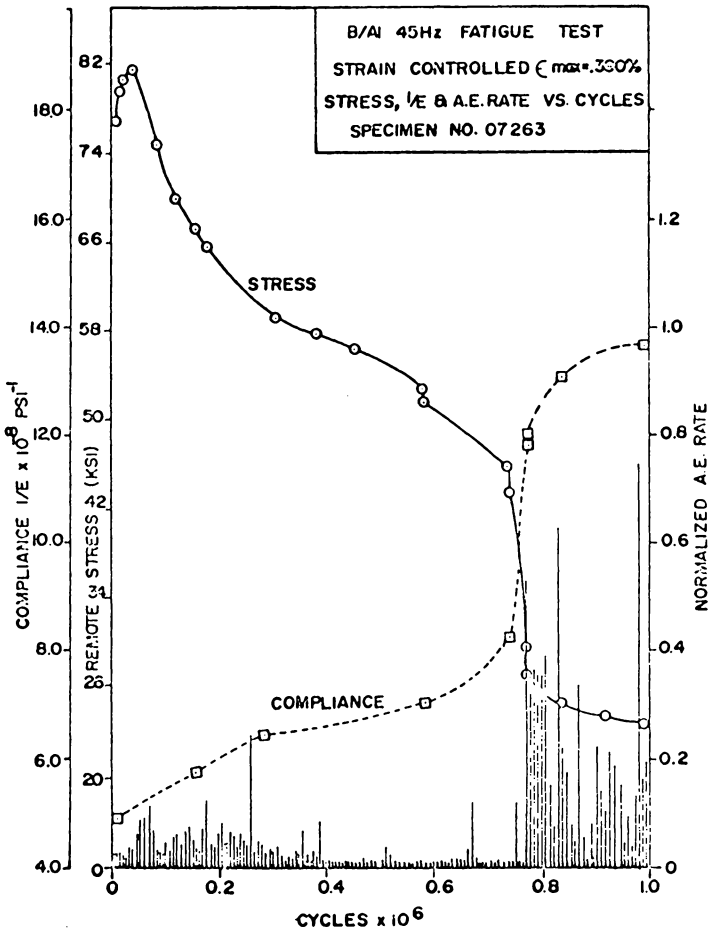

Figure 27. Stress, compliance, and A.E. versus cycles for 45Hz B/Al.

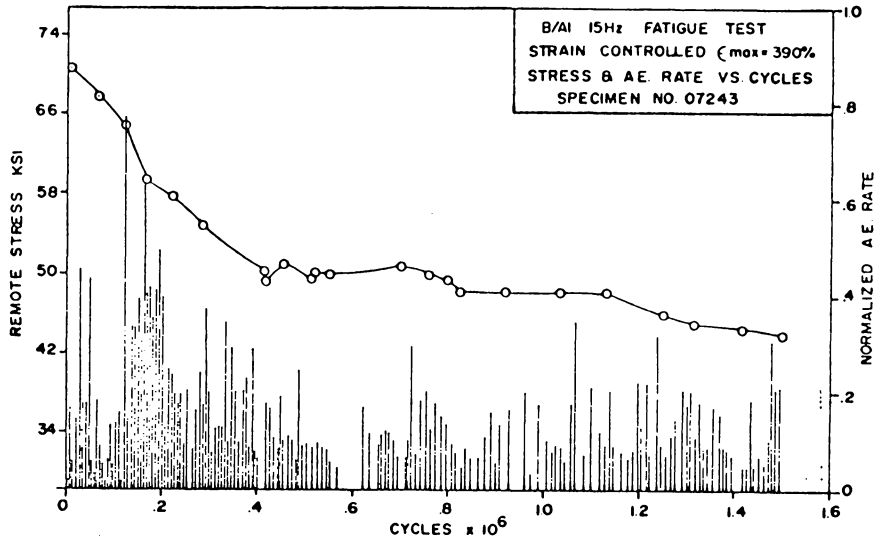

Figure 28. Stress and A.E. versus cycles for 15Hz B/Al.

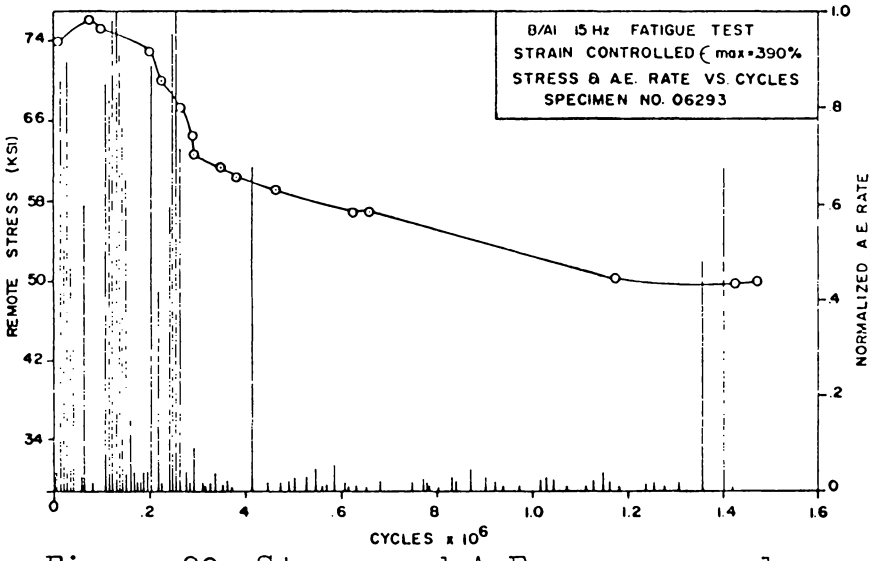

Figure 29. Stress and A.E. versus cycles for 15Hz (transducer debonded @ 300K cycles).

cycles; the magnitude of the A.E. rate very closely follows the slope of the stress plot. During this time there was fairly steady visual damage propagation on both sides of the hole. Between 400K and 500K cycles, this growth seemed to arrest itself at a 'visually severe' stage. From 500K cycles to the end of the test, there were only small amounts of visual damage growth. During this period the stress continued to drop at a much slower rate than previously. In general, the A.E. rate for this portion of the test is consistent, but again, seems somewhat high considering that the rate of damage development was slow. As before, this can be explained as possible specimen fretting caused by extensive damage.

Figure 28 is of a B/Al fatigue test run at the same conditions as the test in Figure 27. There is good correlation between structural damage and A.E. for the first 300K cycles, but after this the A.E. rate is quite low except for several short bursts. The reason for this disparity was found to be debonding of the transducer during the test (at about 300K cycles). Many methods of bonding the transducer have been tried. The present method uses double-backed 3M tape between the transducer and the specimen, with several more layers over the transducer to hold it in place. In observing numerous tests where this method has been used, the bond either remains essentially constant in transmission losses or becomes debonded (as in the case of Figure 29) causing very high transmission losses. This apparent go-nogo nature of the bond is an advantage in the analysis of the data, in that gradual degradation of the bond (which could confuse the data) does not appear to occur.

A load-controlled fatigue test of B/Ep at 30Hz is shown in Figure 30. By observing the change in strain with

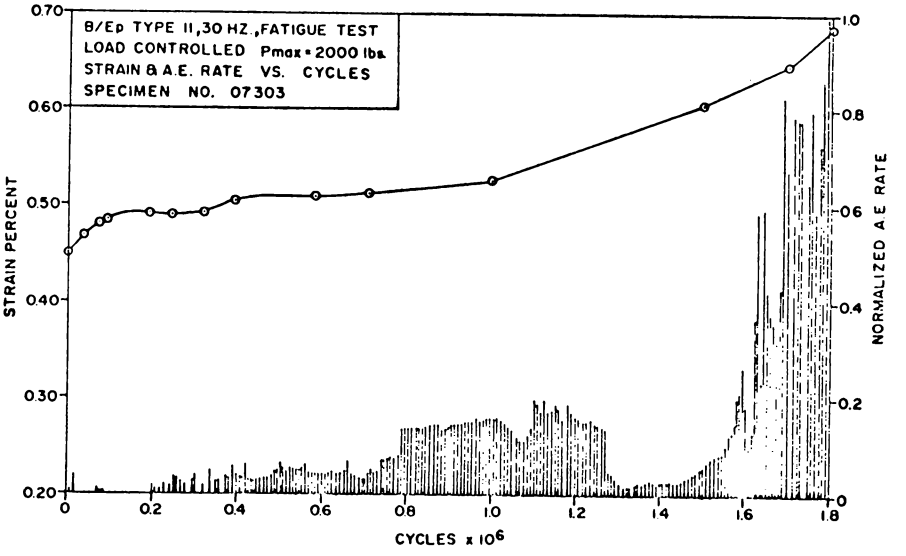

Figure 30. Strain and A.E. versus cycles for 30Hz B/Ep (load-controlled test).

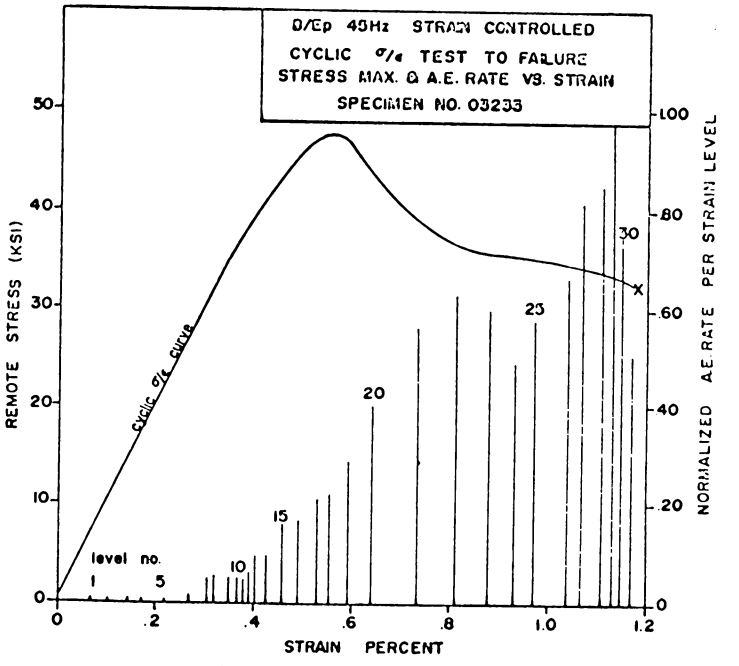

Figure 31. B/Ep cyclic σ/ε curve with A.E. rate per level shown.

cycles it is noted that most of the damage occurs at the end of the test in an accelerated fashion, as compared to the strain-controlled tests, where a large amount of damage is incurred early in the test. And, as would be expected from previous tests, the A.E. rate increases with increasing damage. The drop off in A.E. rate around 1.4M cycles may be explained in the following way. Prior to 1.4M cycles the damage was quite severe and propagating slowly. Perhaps it propagated in such a manner as to preclude the fretting noise present between 800K and 1.2M cycles. This occurance has been noted on several strain-controlled tests of this material; the periodic (same frequency as the test) fretting or scraping noises viewed on an oscilloscope were observed to start and stop with progressing visual damage propagation.

The results of a 45Hz strain-controlled cyclic stress/strain test of B/Ep are shown in Figures 31, 32, and 33. The average acoustic emission rate per level is plotted versus strain, superimposed on the cyclic stress/strain curve in Figure 31. The manner in which the surface damage propagated, referenced by strain level, is shown in Figure 32. The first substantial acoustic emission occurred at levels 7 and 8 ; this was accompanied by cracks at 2, 8, and 10 o'clock around the hole. As the strain level was increased, an almost linear increase in A.E. rate is noted through level 22. This increase in rate is paralleled by an increase in damage, as shown in Figure 32. On about level 22 or 23, delaminations were noted eminating inward towards the hole from the predominate second and fourth quadrant cracks. This was followed by a drop in A.E. rate on the next level, with little cracking, and then an increase in A.E. rate on level 25 and 26, with further cracking and delaminations. From level 26 to fail-

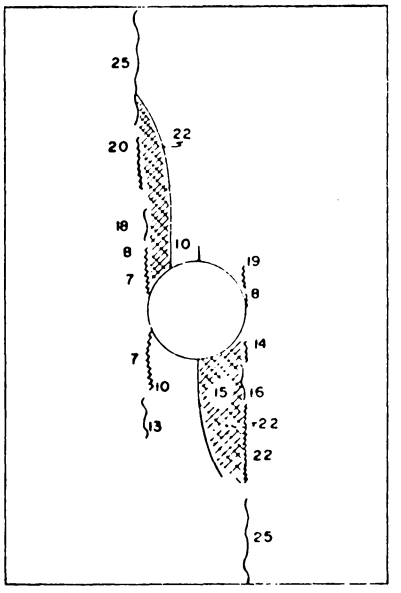

Figure 32. Surface damage propagation for test shown in Fig.31, number indicates increasing strain level.

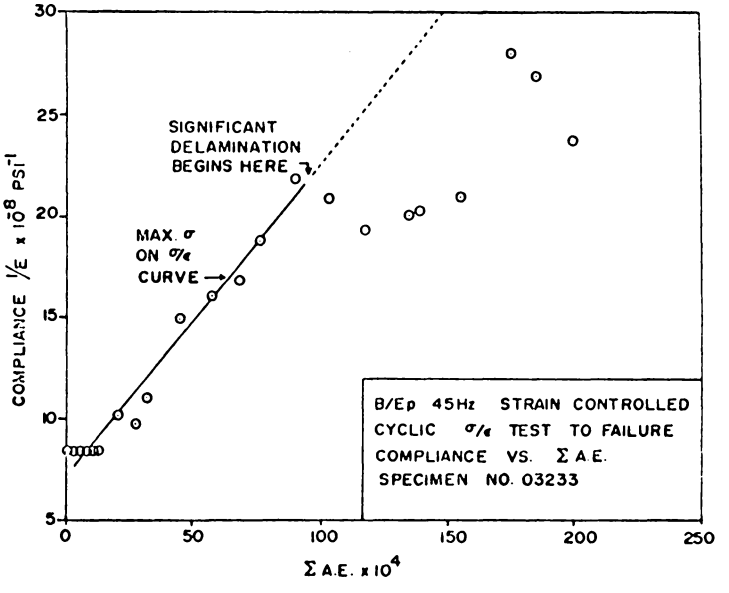

Figure 33. Compliance versus totalized A.E. for test shown in Fig. 31.

ure, little further damage was incurred, although a rise in A.E. rate was noted. This, again, was presumed to be due to scraping noises from the delaminations.

Fig.33 shows a plot of compliance versus totalized acoustic emission. There is an extremely good correlation (indicated by the straight line) between these two variables for the initial portion of the test where there is little delamination. After level 24, where there is significant delamination, the total A.E. increases more rapidly than does the compliance, as evidence to the presence of scraping noise caused by the delamination. Also, since the caompliance was computed from the hysteresis loops and after level 23 the hysteresis loops are very rounded (due to large amounts of damping), there is considerable chance for error in computing the compliance. This is evidenced by the decrease in compliance for several levels. Therefore, keeping these factors in mind, there is an relatively good correlation between damage (compliance) and totalized acoustic emission.

Throughout the previous discussion, there has been a continued reference to extraneous fretting or scraping noise that causes the data to deviate from 'ideal'. It was observed, using an oscilloscope, that most of these noises took place during the unloading cycle and during the lower half of the loading cycle. Therefore, it became increasingly desirable to look at the acoustic emission during only a portion of the loading cycle. A system was devised that could do this and it was described in the experimental section. A number of tests have been performed using this system and the results shown in Figures 34 and 35 are indicative of these tests.

Figure 34 is a plot of total acoustic emission and compliance versus cycles for a 15Hz B/Al strain-controlled

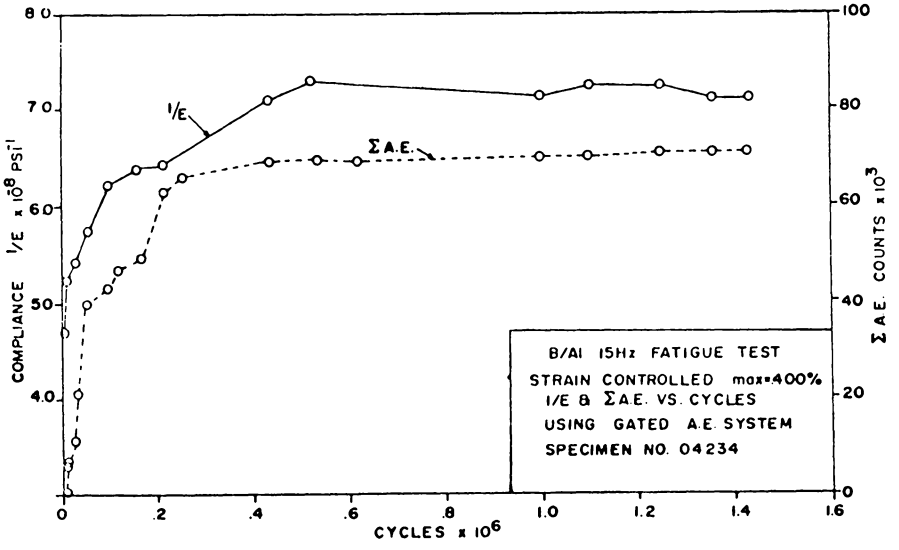

Figure 34. Compliance and totalized A.E. versus cycles for 15Hz B/Al.

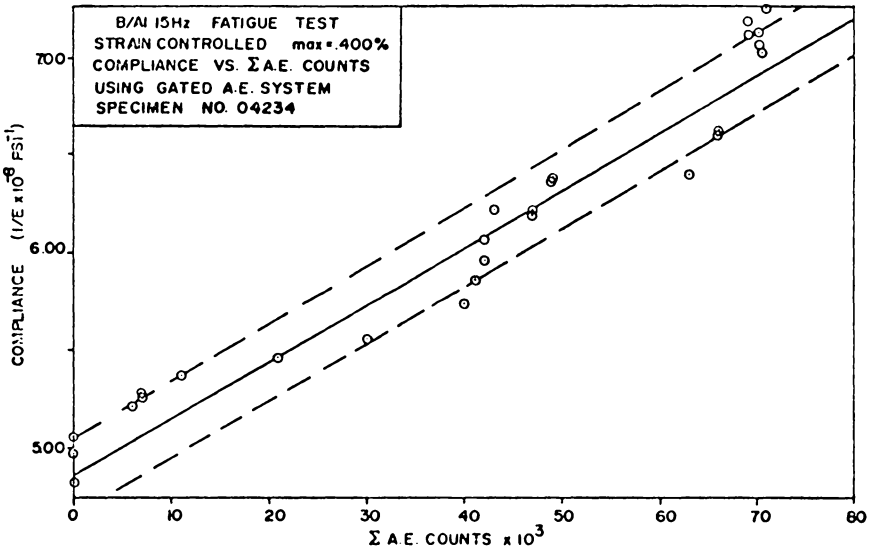

Figure 35. Compliance versus totalized A.E. for test shown in Fig. 34.

fatigue test. As seen from the plot, there is almost a one-to-one relationship between the two curves, with most of the acoustic emission activity and damage taking place during the first 600K cycles. It was noted during the test that significant visual damage was present at 600K cycles and that the customary fretting noise was also present, but, as evidenced by the plot, this noise was excluded and not counted as acoustic emission counts.

Further evidence of the relationship between compliance and acoustic emission is shown in Figure 35. Here the curves shown in Figure 34 are plotted against each other and the results approximate, quite closely, a straight line, within the limits of experimental error (shown as dotted straight lines on the plot). In later tests refinements in the data acquisition has minimized this error.

CONCLUSIONS

As evidenced by the data, a good correlation between specimen damage and totalized acoustic emission, and the rate of damage propagation with acoustic emission rate exists until significant delaminations cause extraneous scraping and fretting noise. This extraneous noise occurs primarily during specimen unloading and at low stress levels during specimen loading. It, therefore, can be eliminated by gating the acoustic emission signal to count only during the top half of the loading portion of the cycle. By using this gated acoustic emission system excellent agreement between over all structural damage (both rate and extent) and acoustic emission is achieved throughout the entire test. This is evidenced by an aparent linear first order relationship between totalized acoustic emission and dynamic structural compliance.

Having observed the previous relationships between

acoustic emission and structural damage, the basis for a fracture mechanics-type model is established. Its foundation would be the following.

If we assume that the acoustic emission sigal is a damped sinusoid, then it can be shown (37) that the number of counts per event is proportional to the initial voltage intensity of the event. Since the transducer operates on the basis of the piezoelectric effect, this voltage is proportional to the energy released per event ($U \alpha n$). Neglecting work terms, G, the strain energy release rate, may be written as:

$$G = \frac{\partial U}{\partial A} \quad \text{.....Eq.(2)}$$

where A is the collective area of newly created debonding, delamination, and microcracking damage attributed to fiber breakage. Then defining a specimen compliance, C, in the normal way,

$$G = \tfrac{1}{2} P^2 \frac{\partial C}{\partial A} \quad \text{.....Eq.(3)}$$

for a specimen under load P (33). Using the chain rule, then equation 3 becomes:

$$G = \tfrac{1}{2} P^2 \frac{\partial C}{\partial D} \frac{dD}{dA} \quad \text{.....Eq.(4)}$$

where D is a damage function which represents, quantitatively, the collective extent of local damage. In the present case,

$$D = D(n) \quad \text{.....Eq.(5)}$$

and for the purpose of this discussion set D = n, the total acoustic emission count. The slope of the linear relationship in Figure 34 then provides $\partial C/\partial D$ immediately. Moreover, the nature of dD/dA should be subject to direct experimental determination , with the expected result that dD/dA will depend on the damage mechanisms involved and their relative contribution to the eventual failure mode.

Therefore, utilizing this type of analysis acoustic emission can be used as an experimental basis for relating strain energy release and material failure events.

CHAPTER V
THERMOGRAPHIC ANALYSIS

In this chapter real-time video thermographs are compared with fatigue damage developement. Correlations between thermography and damage are presented and an energy-model that relates thermal emission with strain energy release is discussed.

INTRODUCTION

Since fatigue damage initiation and propagation is, by definition, a dynamic process, a likewise dynamic experimental technique must be used to characterize it. Furthermore, this system should be entirely passive and time-resolved in nature. One such technique was discussed in the previous chapter. Another method, and not totally unrelated since both rely on energy emissions, is infrared thermography.

When, in the process of cyclic fatigue, a composite specimen developes damage, there is a release of strain energy. Most of the released strain energy is dissipated in the form of heat. Therefore, the premise is that the pattern or image of the thermal emission from the surface of the specimen will be indicative of damage developement. It will be the purpose of this chapter to discuss this application of thermography and how it might be used in failure analysis. And finally, a possible approach, based on an energy balance, offered by Reifsnider and Stinchcomb (39) is discussed.

EXPERIMENTAL METHODS

A real-time video (16 frames/second) thermographic camera model 680, manufactured by AGA Corp. of Sweden, was

used to monitor the thermal emission produced by specimens during cyclic loading. This unit provided both a black and white presentation and a continuously variable ten-color isothermal representation.

A more complete description of this system and other experimental methods is contained in chapter II.

DISCUSSION

A black and white representation of a series of ten-color isotherm thermographs taken during a 45Hz B/Ep fatigue test is shown in Figure 36. The scale shown at the bottom of each thermograph indicates the temperature ordering of the isotherms; coldest to the left and hottest to the right. The notch on either the right or left side of the thermograph indicates the differential temperature range of the isotherms. The thermographs are presented in sequential order, beginning very early in the test with Figure 36a.

Initially, as the specimen is first cycled, a classic butterfly pattern, centered about the specimen hole, is noted (Figure 36a). After several thousand cycles, this pattern begins to elongate into the second and fourth quadrants (Figures 36 b and c), with the hottest zone in the second quadrant. It should be noted that this growth of the thermographic pattern is observed before any visual damage can be seen around the hole. When the visual damage did occur, it appeared first in the second and fourth quadrants, in that order. As the fatigue damage increased during the test, the pattern grew from that shown in Figure 36d to the pattern of Figure 36c, in all cases preceding visual damage. The thermal image shown in Figure 36e was taken at approximately 400K cycles. At this point in the test, visual damage seemed to stabilize, while structural

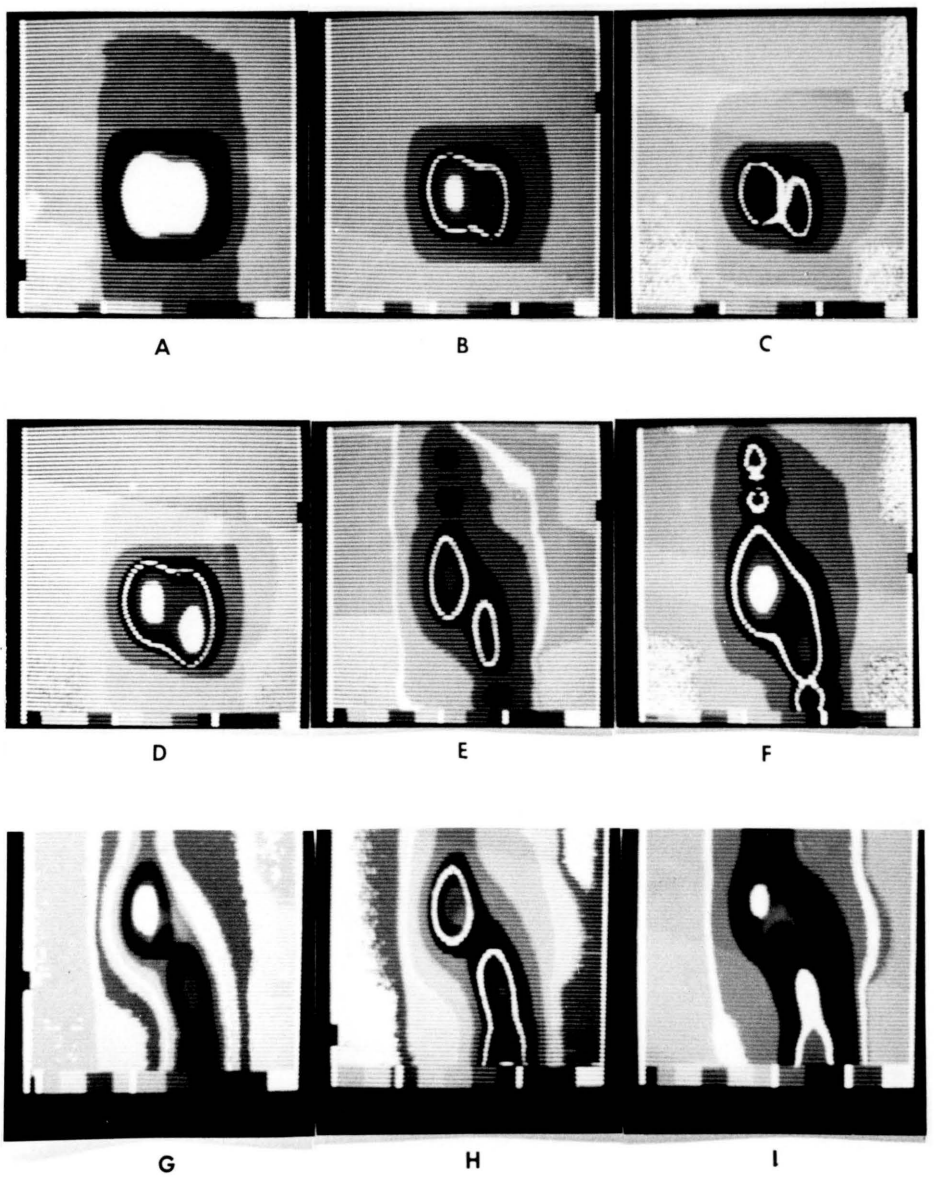

Figure 36. Black and white representation of ten-color thermograph for a 45Hz B/Ep fatigue test.

compliance continued to increase very slowly until the end of the test. During this time the thermal image remained similar in appearance, but increased slightly in intensity to that shown in Figure 36f.

The remaining three thermographs in Figure 36 show the increasing extent and intensity of the thermal image during the P/M cyclic stress/strain test. Throughout the P/M cyclic stress/strain test, while the cyclic strain was increasing, the thermal image advanced and increased in intensity prior to any visual indication of advancement. The eventual fracture pattern of the specimen is shown in Figure 37. It is quite interesting to note that fracture occurred where the highest temperature was indicated in Figure 36i. Also, fracture occurred in the quadrants where the thermal intensity was greatest very early in the test.

The previously discussed test is typical of the thermographic and experimental damage correlations noted for a large number of tests of B/Ep. As shown in Figure 38, the eventual damage affected zones and fracture initiation points vary from test to test, the thermal emission pattern can be used quite effectively to monitor damage advancement and to predict fracture initiation points. Due to the poor conductivity of B/Ep, relatively large temperature differentials were encountered (ΔT up to 60°F.), making thermal analysis quite successfull. In the case of B/Al, which is a good conductor, the temperature differential was significantly less (ΔT between 10° and 15°F.), making analysis more difficult, but still useful.

As stated previously, one source of these thermal emissions is from the strain energy released in damage propagation. Another source is from internal friction. Due to the large amounts of wide spread debonding and delamination in B/Ep, this is most likely a substantial source of

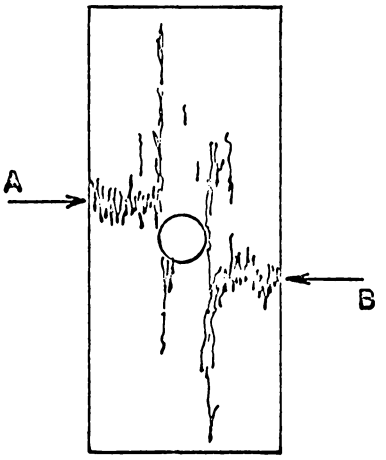

Figure 37. Fracture pattern of 45Hz B/Ep fatigue test shown in Fig. 36.

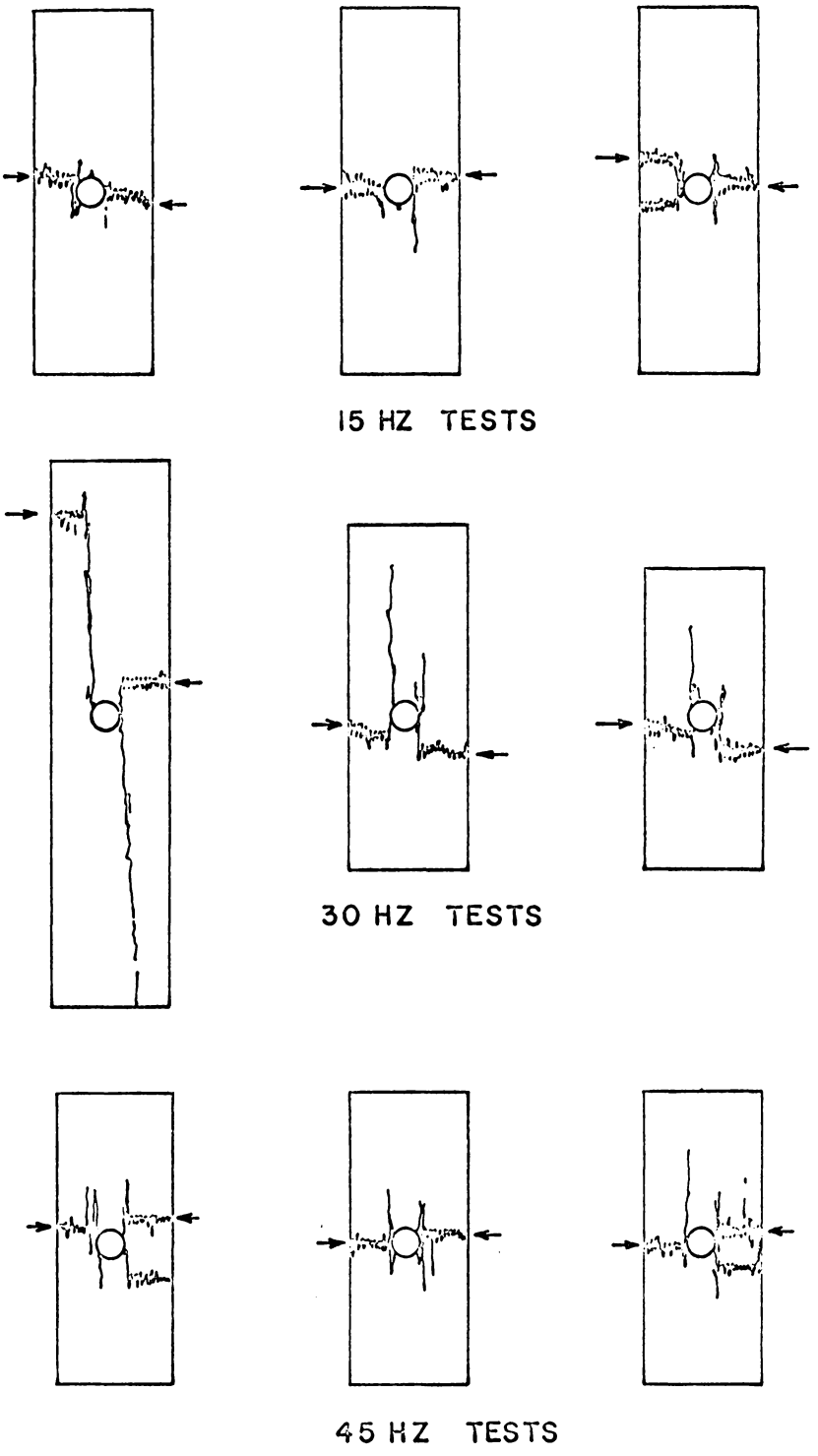

Figure 38. Typical fracture patterns for B/Ep fatigue tests at several frequencies.

thermal emissions in these specimens. In the case of B/Al, there is no debonding and smaller amounts of delamination, therefore, internal friction does not play a major role. It should be noted that although thermal emission due to internal friction is not related to the strain energy release, this emission does serve to indicate what region has been damaged.

A theory, based on energy considerations similar to those used in the previous chapter on acoustic emission, has been proposed by Reifsnider (39). Using a first law analysis, he stated that the heat emissions (Q) are related to the differential work (W) done on the system and the change in system potential energy (E).

$$\Delta Q = \sum_i \Delta W_i - \Delta E \quad \text{.....Eq.(6)}$$

Three contributions to the work term are identified as: work done against internal damping; frictional work done in rubbing together two fracture surfaces; and work done by external forces as related to specimen stiffness changes during the damage process. Designating this last work contribution as ΔW_3, it is shown that:

$$\Delta W_3 - \Delta E = \frac{P^2}{2} \Delta C, \quad \text{.....Eq.(7)}$$

where C--compliance

P--applied load.

Then, upon evaluation of the first two work contributions and the substitution of equation 7 into equation 6, a relationship quite similar to that of Irwin-Orowan for strain energy release can be developed for the thermal emissions and compliance.

Based on the previous discussion, there are potentially good correlations between quantitatively measurements of thermal emissions and strain energy release theories, with results similar to those discussed in the

acoustic emission chapter. The thermal emission, however, provide, in addition to intensity, the intensity distributions which can be used to map out the damage affected zone. But with these advantages come disadvantages, in that the thermal image must be interpreted to provide a quantitative number and the emissions due to friction are difficult to separate from the other heat sources at this point in the developement of the technique.

CONCLUSIONS

In light of the preceding discussions, several conclusions can be made. They are as follows:

- Thermography can be used very successfully as a means of detecting damage initiation and propagation in composite materials. Damage can usually be detected thermographically before it can be perceived visually. Also, using thermography it has been possible to predict fracture site and to predict damage modes.

- Using a first law of thermodynamics approach, thermal emissions can be related to a strain-energy-release theory. Together with the previously developed acoustic emission theory, this thermal emission theory could be used to provide an experimental basis for an energy-related fracture analysis.

At present the thermographic method, developed at Virginia Tech, is a valuable nondestructive investigation tool which provides the only direct method of detecting the position and severity of dispersed damage, common to these materials, during fatigue loading. As models of the fatigue damage process are developed, the thermographic patterns can be compared to the heat patterns predicted by each analytical representation, thereby providing an indispensible means of discriminating between

correct and incorrect concepts. The fact that it is a time resolved technique which provides data in picture form also raises a number of interesting possiblities for the use of this method for practical fatigue damage detection applications.

CHAPTER VI

STRAIN ENERGY RELEASE-POTENTIAL THEORY

In this chapter a new theory called the Strain Energy Release-Potential theory is formulated. Based on this theory, failure models for B/Al and B/Ep are proposed.

INTRODUCTION

The fatigue and fracture damage mechanisms involved in the failure of fiber reinforced composite materials are many, complex and interdependent. There have been several efforts to utilize linear elastic fracture mechanics (LEFM) (12-16) in describing the fracture behavior of composites. In most cases the material is treated as a flawed anisotropic plate. This flaw is usually a crack, which is artificially induced by means of a saw-cut or sharp notch. Then, using conventional methods, critical values of the stress intensity factor (K_{Ic}) and/or the strain energy release rate (G_{Ic}) are determined, using the change in length of this induced crack as the damage parameter. The basic premise of this type of analysis is the assumption that the failure of these materials can be characterized by the propagation of a single crack to failure.

The results of a large number of fatigue and static tests of B/Ep and B/Al flawed angle-plied coupons (19,20) have indicated that damage propagation is more an advancement of a damage affected zone rather than the propagation of a single crack. Within this zone there exists some combination of fiber breakage, debonding, delamination, and matrix cracking. Since elastic analysis of each of these damage mechanisms proves quite cumbersome (40), a more basic and general approach is desired. One possible approach has its origin in the fracture energy release concept postulated by Griffth and further expanded by Orowan,

Irwin and Kies (41,42).

It will be the purpose of this chapter to present a basis for this energy related failure criterion. Using this criterion, a rationale for fatigue damage propagation will be postulated and compared to data from composite fractographs, discussed in chapter III.

THEORY

The concept of crack instability in a solid as first postulated by Griffth (43) is that the crack will begin to propagate when the elastic energy released by its growth is greater than the energy required to create the new fracture surfaces. The Griffth concept assumes self-similar propagation. In an effort to account for the direction of propagation, Sih (43) has proposed the concept of strain energy density. Sih's theory has two fundamental hypotheses: the crack will spread in the direction of maximum potential energy density and the critical intensity of this potential field governs the onset of crack propagation.

In light of the two previous concepts, it seems reasonable that the potential for strain energy release is the driving force for crack propagation. Extending this line of reasoning to include the various damage mechanisms observed in composite material failure, then, each individual mechanism has a distinct driving force or potential for strain energy release. As stated by the second law of thermodynamics, a system subjected to irreversible processes must experience an increase in entropy. Since the processes involved in each damage mechanism are, by nature, irreversible, and for an isothermal system an increase in entropy is directly proportional to a decrease in internal energy, damage propagation can be thought of as a process directly

governed by the second law (It is assumed that no work is done on or by the system during the damage events, or if it is, that it does not influence the internal choice of damage mechanism.). It therefore follows, that an event that causes the greatest decrease in internal energy will be the most likely to occur, given an otherwise equal probability of occurance for all possible events. This assumption is made in the spirit of the proportionality between entropy and probability assumed by Boltzman (55). Applying this directly to a composite material system, if all other factors affecting the probability of occurance of several damage mechanisms are the same, then the mechanisms most likely to occur first will have the highest potential for release of strain energy (since the prime contributor to a decrease in internal energy is a release in strain energy). Therefore, for total damage development in a composite material, given an otherwise equal probability of occurance of all possible damage mechanisms, the total driving force will be related to a summation of the potential for strain energy release of all mechanisms, with those mechanisms having the highest value dominating or most likely to occur.

In the following sections, three predominate damage mechanisms, debonding, delamination, and fiber breakage, will be considered. By suitable analytical methods an expression for the potential for strain energy release for each will be developed and compared.

A. Fiber Debonding

In this section an expression for the stored strain energy of a simple fiber/sheath model will be derived. The strain energy release caused by debonding will then be taken to be the difference in strain energy of the coupled fiber/sheath system and that of the fiber and sheath considered separately. The analysis is a plane strain, axi-

symmetric, elastic solution (although for the B/Al case the secant modulus was used to partially account for plasticity) first formulated by Ebert and Gadd (44).

Considering the model in Figure 39 and taking the sum of the forces in the radial direction gives,

$$\sigma_{rr}dr + rd\sigma_{rr} - \sigma_{\theta\theta} = 0 \quad \text{.....Eq.(8)}$$

In cylindrical coordinates Hooke's Law is

$$\begin{aligned} E\epsilon_{zz} &= \sigma_{zz} - \nu(\sigma_{rr} + \sigma_{\theta\theta}) \\ E\epsilon_{rr} &= \sigma_{rr} - \nu(\sigma_{zz} + \sigma_{\theta\theta}) \\ E\epsilon_{\theta\theta} &= \sigma_{\theta\theta} - \nu(\sigma_{zz} + \sigma_{rr}) \end{aligned} \quad \text{.....Eq.(9)}$$

Rewriting and arranging equations (9) gives,

$$\begin{aligned} \sigma_{\theta\theta}/K &= (1-\nu)\epsilon_{\theta\theta} + \nu\epsilon_{rr} + \nu\epsilon_{zz} \\ \sigma_{rr}/K &= (1-\nu)\epsilon_{rr} + \nu\epsilon_{\theta\theta} + \nu\epsilon_{zz} \end{aligned} \quad \text{.....Eq.(10)}$$

where $K = E/(1-\nu)(1-2\nu)$

Now, assuming rotational symmetry, the strains can be written as,

$$\begin{aligned} \epsilon_{rr} &= \frac{d\phi}{dr} \\ \epsilon_{\theta\theta} &= \phi/r \end{aligned} \quad \text{.....Eq.(11)}$$

Substituting equations (11) into equations (10) gives,

$$\begin{aligned} \sigma_{\theta\theta}/K &= \frac{d\phi}{dr} + (1+\nu)\,\phi/r + \nu\epsilon_{zz} \\ \sigma_{rr}/K &= (1-\nu)\frac{d\phi}{dr} + \nu\,\phi/r + \nu\epsilon_{zz} \end{aligned} \quad \text{.....Eq.(12)}$$

And substituting equations (12) into equation (8) gives,

$$\frac{d^2\phi}{dr^2} + \frac{1}{r}\frac{d\phi}{dr} - \phi/r^2 = 0 \quad \text{.....Eq.(13)}$$

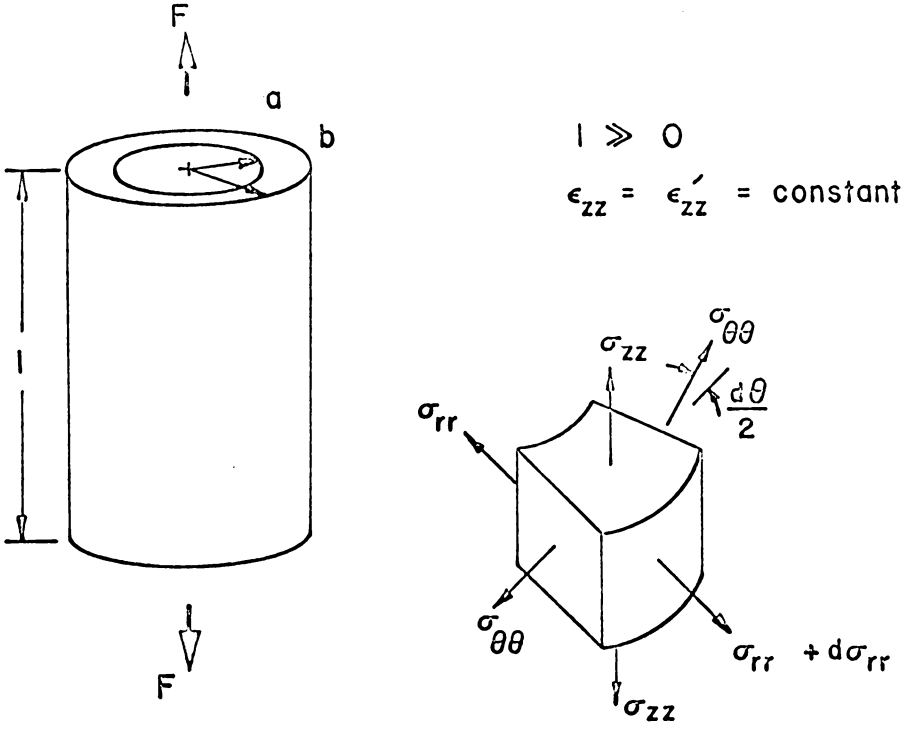

Figure 39. Fiber/sheath model.

A solution of equation (13) is

$$\phi = C_1 r + C_2/r \quad \text{(matrix)}$$

and .....Eq.(14)

$$\phi' = C_3 r + C_4/r \quad \text{(fiber)},$$

where the prime is used to denote the fiber case and the umprimed quantities represent the matrix material.

Now substituting equations (14) into equation (13) and appling the following boundary conditions:

$$\sigma_{rr} = 0 \ @ \ r = b$$
$$\phi = \phi' \ @ \ r = a$$
$$\sigma_{rr} = \sigma'_{rr} \ @ \ r = a$$
$$\phi' = 0 \ @ \ r = 0 \ ,$$

yields,

$$C_1 = (a^2\epsilon_{zz}(1-2\nu)/\beta) - \nu\epsilon_{zz}$$
$$C_2 = a^2b^2\epsilon_{zz}/\beta \quad \text{....Eq.(15a\&b)}$$

for the matrix and for the fiber,

$$C_3 = (\epsilon_{zz}(a^2(1-2\nu)) + b^2/\beta) - \nu\epsilon_{zz} \text{.Eq.(15c)}$$

where

$$\beta = (1/(\nu-\nu'))(a^2(1-2\nu)(1-K/K') + b^2(1 + (1-2\nu)K/K')$$

And substituting equations (15) into equations (14) yields,

$$\phi = (a^2\epsilon_{zz}/\beta)(r(1-2\nu) + b^2/r) - r\nu\epsilon_{zz}$$

and .....Eq,(16)

$$\phi' = r\epsilon_{zz}((a^2(1-2\nu) + b^2)/\beta - \nu)$$

Then solving for the stresses in the fiber and the matrix, respectively, gives,

$$\sigma_{rr} = a^2\epsilon_{zz}(1-2\nu)(1-b^2/r^2)(K/\beta)$$
$$\sigma_{\theta\theta} = a^2\epsilon_{zz}(1-2\nu)(1-b^2/r^2)(K/\beta)$$
$$\sigma_{zz} = E\epsilon_{zz} + a^2\nu\epsilon_{zz}(1-2\nu)(K/\beta) \quad \text{.....Eq.(17)}$$
$$\sigma_{r\theta} = \sigma_{rz} = \sigma_{\theta z} = 0$$

and

$$\sigma'_{rr} = \sigma'_{\theta\theta} = \epsilon_{zz}K' \left\{\left\{\frac{a^2(1-2\nu) + b^2}{\beta}\right\} - (\nu-\nu')\right\}$$
$$\sigma'_{zz} = E'\epsilon_{zz} + 2\nu'\epsilon_{zz}K' \left\{\left\{\frac{a^2(1-2\nu) + b^2}{\beta}\right\} - (\nu-\nu')\right\}$$
$$\sigma'_{zr} = \sigma'_{r\theta} = \sigma'_{\theta z} = 0 \quad \text{.....Eq.(18)}$$

Now, solving for the strains, realizing that

$$\epsilon_{zz} = \epsilon'_{zz} = \text{constant}$$
$$\epsilon_{\theta\theta} = \epsilon'_{\theta\theta} \quad @\ r = a,$$

and

$$\epsilon'_{\theta\theta} = \epsilon'_{rr} \ ;$$

gives,

$$\epsilon_{rr} = \frac{d\phi}{dr} = \frac{a^2}{\beta}\epsilon_{zz}((1-2\nu) - (2b^2/r^2)) - \nu\epsilon_{zz}$$
$$\epsilon_{\theta\theta} = \phi/r = \frac{a^2}{\beta}\epsilon_{zz}((1-2\nu) + (2b^2/r^2)) - \nu\epsilon_{zz} \quad \text{....Eq.(19)}$$
$$\epsilon_{r\theta} = \epsilon_{rz} = \epsilon_{\theta z} = 0$$

and

$$\epsilon'_{rr} = \epsilon'_{\theta\theta} = \phi'/r = \epsilon_{zz}\left\{\left\{\frac{a^2(1-2\nu) + b^2}{\beta}\right\} - \nu\right\} \quad \text{...Eq.(20)}$$
$$\epsilon'_{r\theta} = \epsilon'_{rz} = \epsilon'_{\theta z} = 0$$

Since all of the shear stresses are zero, the strain energy is given by:

$$U = \tfrac{1}{2}(\sigma_{rr}\epsilon_{rr} + \sigma_{\theta\theta}\epsilon_{\theta\theta} + \sigma_{zz}\epsilon_{zz}) \quad \text{.....Eq.(21a)}$$

and

$$U' = \tfrac{1}{2}(\sigma'_{rr}\epsilon'_{rr} + \sigma'_{\theta\theta}\epsilon'_{\theta\theta} + \sigma'_{zz}\epsilon'_{zz}) \quad \text{.....Eq.(21b)}$$

Therefore,

$$U_{total} = U + U' \ . \quad \text{.....Eq.(21c)}$$

To evaluate the total strain energy, the expressions for stress and strain are substituted into equations 21a and 21b and the results integrated over the matrix and fiber, respectively.

For the case where the matrix and the fiber are separated, there exists a simple state of uniaxial tension. Therefore, the strain energy is simply,

$$U_o = \tfrac{1}{2}\ {}_{zz}\epsilon_{zz} = \tfrac{1}{2}E\epsilon_{zz}^{\ 2} \quad \text{.....Eq.(22a)}$$

and

$$U'_o = \tfrac{1}{2}E'\epsilon_{zz}^{\ 2} \quad \text{.....Eq.(22b)}$$

for the matrix and the fiber, respectively. And the total unbonded strain energy is

$$U_{o_{total}} = U_o + U'_o. \quad \text{.....Eq.(23)}$$

This, then, results in the strain energy release for debonding to be

$$G_{DB} = U_{total} - U_{o_{total}} \ . \quad \text{.....Eq.(24)}$$

It should be noted that no mention of units was made in the previous derivation. For the time being, these quantities will be left as densities (energy/volume). In a later section this matter will be more completely developed.

B. Delamination

The calculation of the strain energy release caused by delamination was accomplished using a three-dimen-

sional, finite element program developed by Barker, Lin, Dana, and Pryor (45,46).

The program is an isoparametric finite element, minimum potential energy formulation for the problem of a rectangular laminated plate with a hole; several hole shapes being possible (diamond, square, and circular). The curved element has 72 degrees of freedom (Figure 40) with the degrees of freedom preserved at the interfaces so that conections between lamina may be made. Cubical planeform and linear through-the-thickness displacement response function are used. The displacement of finite element theory is used and a conjugate gradient method selects a set of displacements that minimize the total potential energy of the system. According to variational principles, then, this set of displacements is the unique solution to the problem. A listing and complete program user's guide can be found in reference 47.

For these calculations a circular hole modelled by the mesh configuration as shown in Figure 41 was used. All of the anisotropic characteristics of the actual specimens were simulated by the program. To simulate delamination a very thin lamina was sandwiched between the two lamina to be uncoupled. For the coupled case this lamina was assumed to have the material properties of the matrix. To simulate delamination the stiffness of this lamina was allowed to approach unity. The concept of using stiffness reduction to simulate damage is similar to the Unimod scheme originated by Reifsnider and used with good results by Reifsnider and Nair (48). Since the finite element program could only accomadate up to twelve axi-symmetric lamina, in order that the model correspond to available test coupons, only four delamination simulation layers were possible. These were situated symmetrically between the $0°/+45°$ and $\pm 45°$ plies,

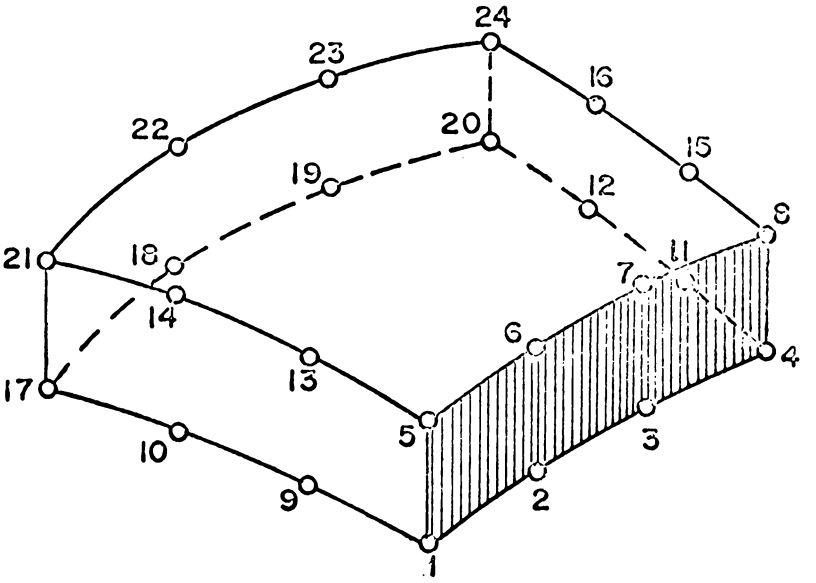

Figure 40. Curved element configuration.

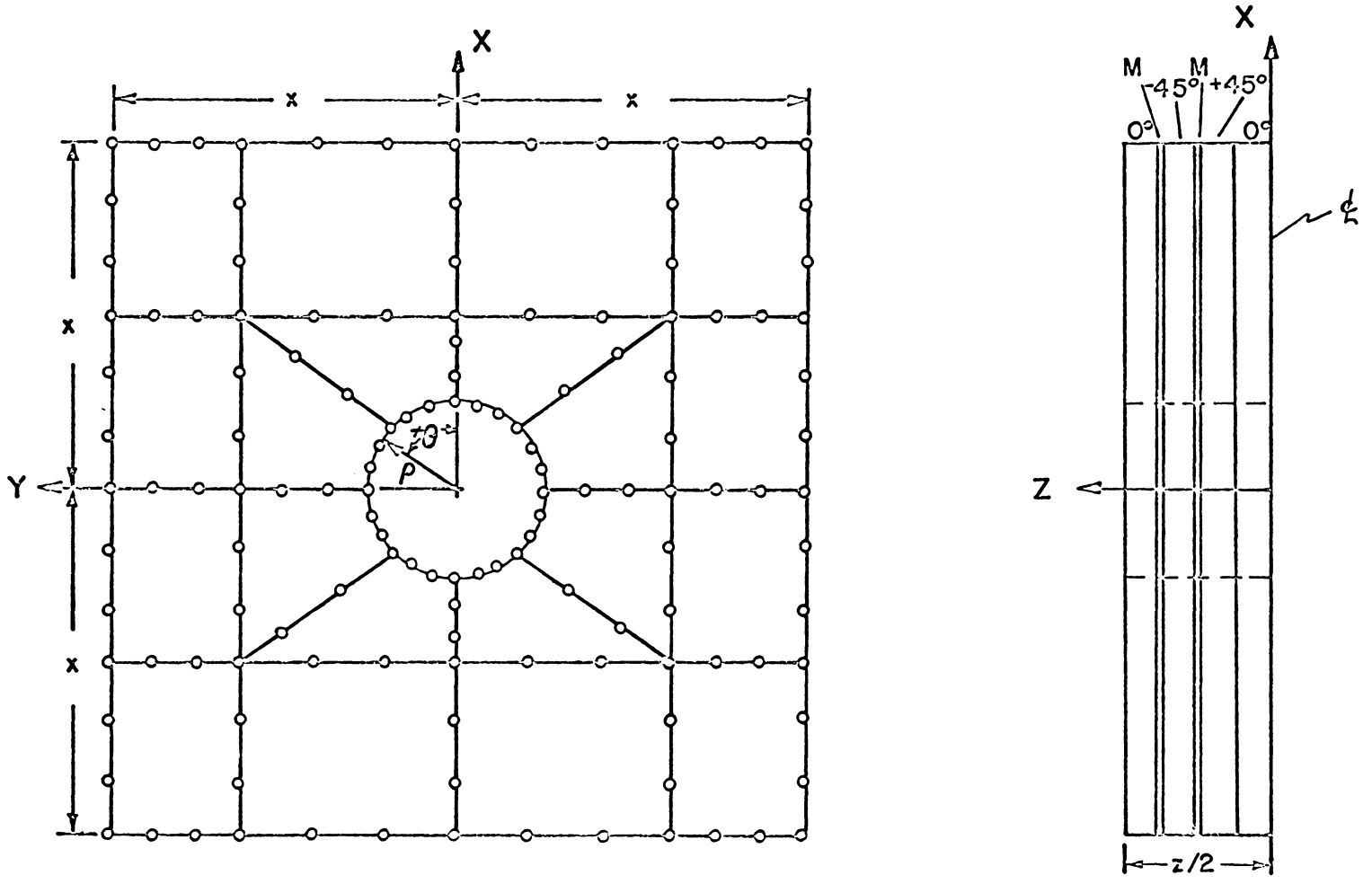

x = 1/2 in = 1.27 cm z = thickness ρ = 1/8 in = 0.318 cm

Figure 41. Element and node structure of finite element model.

since, from experimental evidence, delamination occured there most frequently. Since the computer program could only consider symmetric configuration, the simulated delaminations were also symmetric.

All possible combinations of delaminations were run and the strain energy release was calculated by taking the difference in stored strain energy before and after simulated delamination.

C. Fiber Breakage

Two factors that must be considered when calculating the strain energy released when a constrained fiber fractures are the effective gage length (the length of the fiber over which the strain energy release occurs) over which the fiber fails, and the stress distribution in this region before and after fracture. Since most of the literature in this area stops one step short of actual application, the scheme of this section will be first to examine representative work and then extend it by means of suitable rationale to arrive at an expression for strain energy release.

Olster and Jones (49) considered the case of a crack in the matrix approaching the interface perpendicular to the fiber for both ductile and brittle matrix materials. For the case of the brittle matrix, they assumed that debonding would occur and that the debonded region would represent the effective gage length. Within this region, they assumed the stress in the fiber to be constant and equal to the ultimate stress at failure. For the case of the ductile matrix, the effective gage length was determined by the extent of the plastic zone associated with the advancing crack in the matrix. And the stress distribution within this region was assumed to vary linearly, with the maximum equal to the ultimate strength at the

fracture point and decreasing linearly to some remote value outside the plastic zone. Comparisons were made between calculated values of critical toughness, using the ductile matrix model, and experimental results, using B/Al specimens. A good correlation was only achieved for very low fiber volume fractions (less than 10%); at higher volume fractions (40 to 50%) the calculated values were substantially higher.

Several finite element studies have been made of the stress distribution in the fiber and the matrix caused by the fracture of a single fiber. Barker and MacLaughlin (50) used a linear elastic analysis to examine axially loaded unidirectional composites with a single discontinuous fiber surrounded by unbroken fibers. They varied fiber volume fraction, end-gap sizes and fiber/matrix modulus ratios; and plotted fiber and matrix stresses versus distance along the fractured fiber. As the end-gap decreased and/or the modulus ratio increased, the distribution of stresses moving away from the fracture, along the fiber, tended to drop off more sharply.

Iremonger and Wood (51) performed a similar study, but also included the case where the end-gap was void of matrix material. They found that, for the case of the void end-gap, the stress drop off was sharper than when it was filled with matrix. In other respects, the results agreed quite well with those of Barker and MacLaughlin.

A number of closed form elastic solutions exist for a fiber embedded in a matrix. However, a substantial number of these are limited to very low fiber volume fractions (less than 10%) and/or to non-engineering materials with low fiber/matrix modulus ratios (such as aluminum/epoxy or aluminum/steel), making it impossible to relate the results to actual engineering composite materials.

A series of papers by Erdogan and Pacella (52,53) does, however, include the cases where the fiber volume fraction varies up to 35% and the modulus ratio ranges up to 100. But, this series only considers the case of discontinuous fiber reinforcement with aspect ratios less than 50. The fiber diameters are also somewhat large by as much as an order of magnitude, as compared to boron or glass filaments. The effect of the end-gap can not be assessed since it is assumed to be infinite, but the effect of increasing the modulus ratio is similar to the results of the finite element programs, although the drop off is less sharp by comparison.

To account for the effect of plastic deformation in the matrix, Iremonger and Wood (54) determined the stress distribution along the fibers for a discontinuous fiber composite with elastic fibers and elastoplastic matrix material. The theoretical predictions, obtained by a finite element method, are compared experimentally with a lead/steel model using a surface-coating photoelastic technique. Using material parameters similar to those of B/Al, they determined the stress distribution in the fiber and the matrix, before and after fracture, for an end-gap size of 0.5 fiber diameters. They also concluded that once the matrix was fully yielded, the modulus ratio had little effect and most of the load was carried by the fiber. The axial stress distribution in a fiber adjacent to a discontinuous fiber was also determined.

As evidenced by the previous discussion, there is considerable variation in what might be considered as the effective gage length and in what manner the stresses are distributed in this region, depending upon such variables as a ductile or brittle matrix, the end-gap size, the aspect ratio, the modulus ratio, and/or the fiber volume

fraction. Therefore, to restrict this discussion to the present class of structural engineering materials, only two cases will be considered. The first case will assume a low strength, brittle matrix with a high modulus ratio, similar to a B/Ep composite. The second case will assume a high strength, elastoplastic matrix and a somewhat low modulus ratio, similar to a B/Al composite. Both cases will consider small void end-gaps and about a 50% fiber volume fraction.

For the brittle matrix case, the effective gage length will be assumed to be the length of the debond region (Figure 42). In this region the fiber will be assumed to have a constant stress value equal to its' failure stress. The assumed fiber and matrix stresses, before and after fracture (based on the trends discussed in references 50 and 51), are shown in Figures 43 and 44. Realizing that much greater amounts of energy are stored within the fiber ($E_f/E_m \approx 120$) than in the matrix, it is feasible to assume that the bulk of the energy is released by the fiber over the debonded region, and the energy lost by the fiber outside this debonded region is gained by the matrix as shown in Figure 44. Therefore, the expression for the strain energy release, with units of energy, will be:

$$G_f = \frac{\sigma_f^2}{2E'} (d2\pi a^2), \quad \text{.....Eq.(25)}$$

where σ_f = fiber failure stress
E' = fiber modulus
d = debond length
a = fiber radius.

Now, for the ductile matrix case, the determination of the effective gage length is a good deal more difficult. The method used by Olster and Jones (49), as indicated by their own results, was invalid for high volume

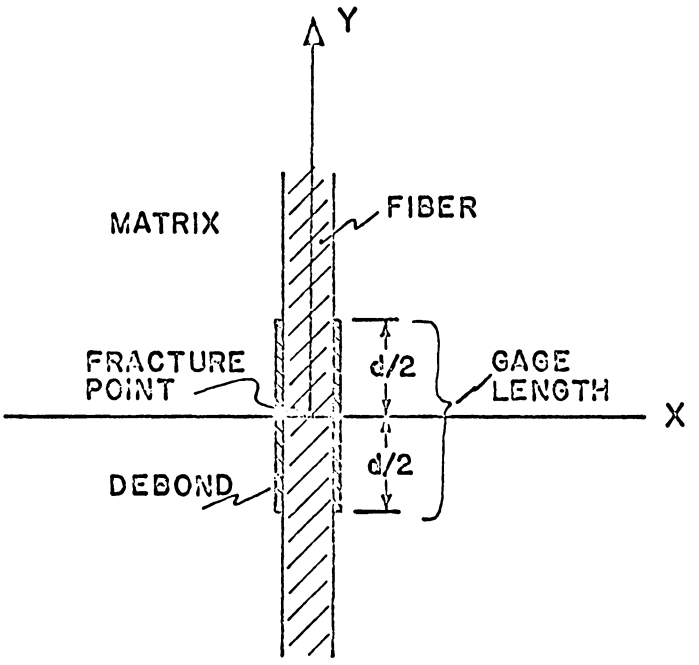

Figure 42. Brittle matrix model, showing gage length.

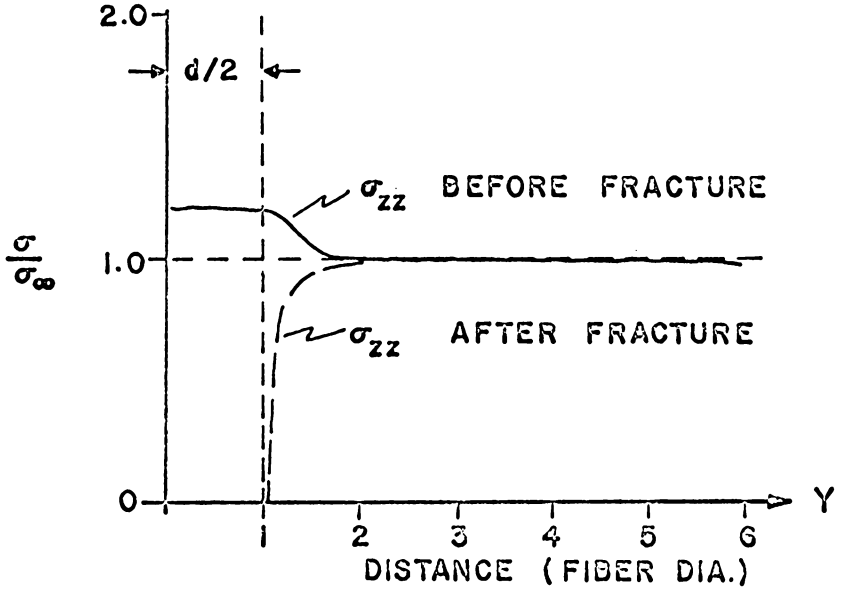

Figure 43. Stress distribution in fiber for brittle matrix composite.

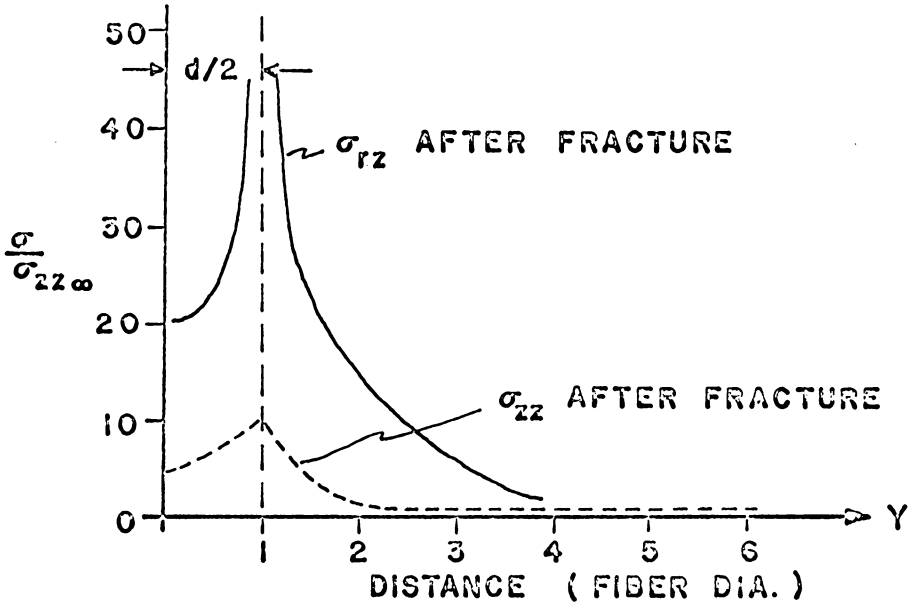

Figure 44. Stress distribution in matrix for brittle matrix composite.

fractions. This is not surprising, because they assumed the matrix plastic zone to govern the gage length. If one assumes a 20KSI yield stress for the matrix, this results in a yield strain of only .0020 in/in. Since the fiber fails at about .008 in/in, the matrix is entirely plastic long before failure. Therefore, another approach must be used.

Since the fiber can withstand stresses of the order of 400 to 500KSI, and the matrix has yielded at 15KSI, the majority of the strain energy is stored in the fiber. Figure 45 is a plot from Iremonger and Wood (54) of the axial stress in the fiber caused by a broken adjacent fiber. Also shown is the stress distribution in that fiber after fracture. Since the end-gap size is large (about $\frac{1}{2}$ a fiber diameter) and filled with matrix material for the distributions shown in Figure 45, it is quite likely that the drop off and/or rise is sharper than shown for the present smaller void end-gap case.

Since the contribution to the strain energy release of the matrix is small by comparison to that of the fiber, only that of the fiber will be considered. Also, due to the smaller end-gap, it is reasonable to assume that the probable gage length is closer to four fiber diameters than six, as shown in Figure 45. Therefore, the strain energy release can be expressed as:

$$G_f = 2\int_0^{4a} \frac{1}{2E},\ \sigma_1^2(x)dx - 2\int_0^{4a} \frac{1}{2E},\ \sigma_2^2(x)dx, \quad ..Eq.(26)$$

where $\sigma_1(x)$ and $\sigma_2(x)$ are the stress distributions before and after fracture. It is assumed that the maximum stress before fracture at $x = 0$ is the failure stress (σ_f) and the stress at $x = 4a$ is $\frac{2}{3}\sigma_f$. It is further assumed that the stress behaves linearly between these two points. If these

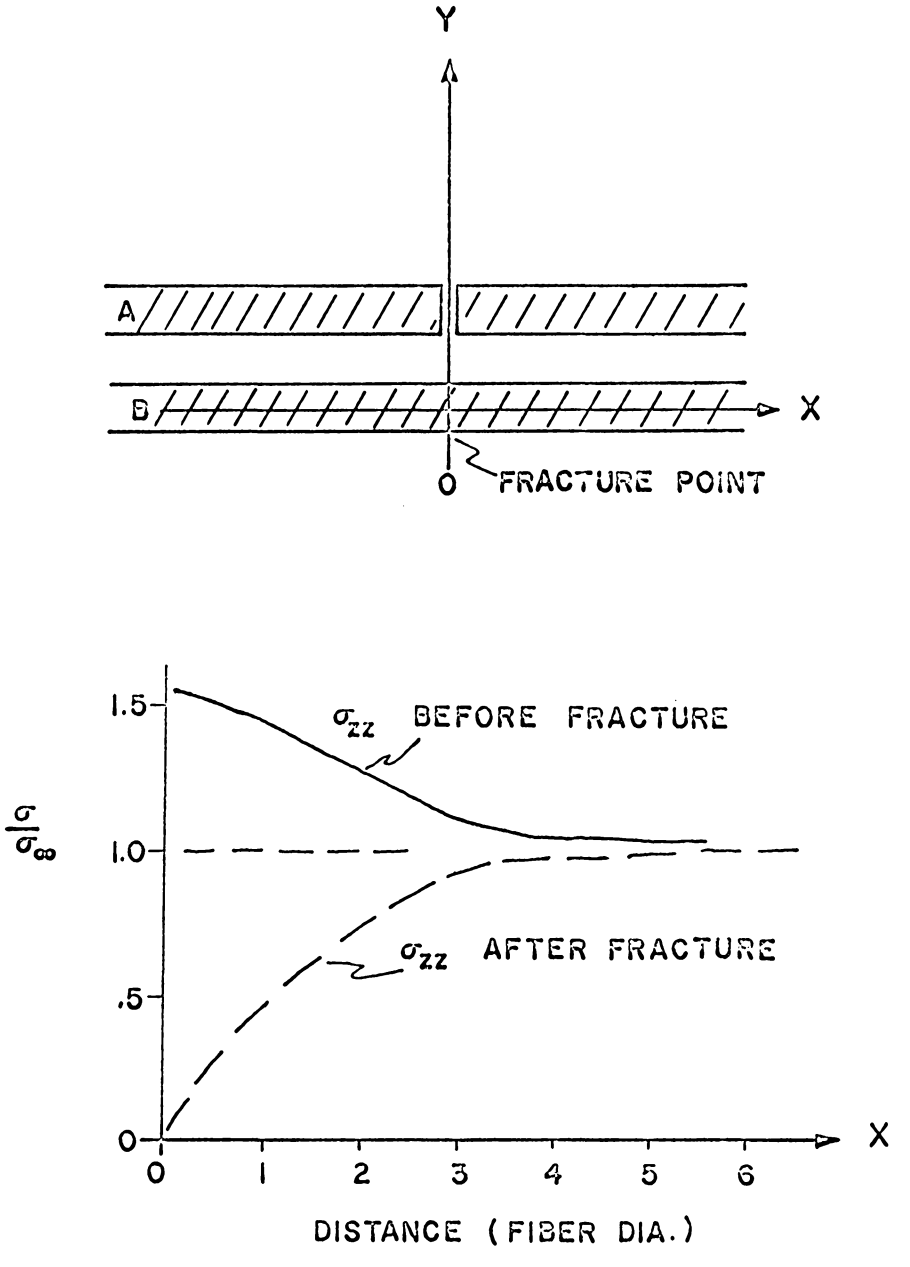

Figure 45. Axial stress distribution in fiber for ductile matrix composite.

substitutions are made in equation (26) and the result is intergrated, and then simplified, the strain energy release (with units of energy per unit area) is:

$$G_f = \frac{20}{9} \frac{\sigma_f^2 a}{E'} \quad \text{.....Eq.(27)}$$

where σ_f = failure stress in fiber
E' = fiber modulus
a = fiber radius.

Now that either an expression for or a means of calculating the strain energy release has been developed for all major damage mechanisms, there remains the problem of expressing each in consistent units. Recalling Griffith's original formulation of his energy criterion, he considered the energy released by the crack in forming a new fracture surface. In the present case for the different damage mechanisms, which are all markedly different in manner of occurance, but in all situations there is a creation of a new fracture surface. Therefore, to allow the necessary comparison between the strain energy released by each damage mechanism, in the subsequent calculations they will be expressed in terms of energy released per newly created fracture area (in-#/in^2).

RESULTS

Since a large number of well documented fatigue tests of B/Ep and B/Al fiber reinforced composites was available, the strain energy released for each damage mechanism was calculated for these two materials. The test specimens used for the fatigue tests in both cases were eight-ply laminates with ply configurations of $(0^\circ;\pm 45^\circ;0^\circ)_{sym}$. A complete description of the specimens, testing procedure,

and results is presented in chapter II. Also , the results of a scanning electron microscopy study are described in chapter III. The material parameters used in calculating the strain energies are listed in Table VII.

Using the material properties in Table VII and the expressions developed in part A of the previous section, the average values of the stresses and integrated values of the strain energies for the matrix and the fiber are shown in Table VIII. The primed quantities denote the fiber and the unprimed represent the matrix. For this table, the strain energy is expressed in terms of energy per unit length along the fiber.

The computed strain energies, associated with delamination using the properties given in Table VII, are listed in Table IX. The ply configuration was $(0^{\circ};M;-45^{\circ};M;+45^{\circ};0^{\circ})_{sym}$, where 'M' designates the matrix layer. The symbol 'D' was used to indicate delamination simulation using the modified Unimod scheme. The strain energy values listed have units of energy.

Using the results of Tables VIII and IX and equations developed in the previous section (part C), the strain energy released per newly created fracture area is listed in Table X. Since the strain energy released, when a fiber breaks in a brittle matrix, is dependent upon the debond length, the value is expressed in terms of energy/newly created fracture surface/unit debond length. The strain energy released for the case of delamination is expressed in terms of going from state one to state two (i.e., MM to MD or MD to DD, etc.).

DISCUSSION

The Strain Energy Release-Potential Theory (SERPT), previously postulated, can be summarized as follows: if the

TABLE VII

Material Parameters Used in Calculating Strain Energy.

Material Parameter		B/Ep	B/Al
Used in Fiber/Sheath Model:			
E_{secant} (matrix) MSI		--	3.75
E (matrix) MSI		.49	10.0
E' (fiber) MSI		58.0	58.0
ν (matrix)		.31	.33
ν' (fiber)		.20	.20
Fiber Volume Fraction		55%	50%
a inches		.002	.0028
b inches		.0024	.00351
$\epsilon_{zz}=\epsilon'_{zz}$ (in/in)		.006	.004
σ'_f (fiber) KSI		450	450
σ_{yield} (matrix) KSI		--	15
Used in Computer Program:			
ϵ_{11} in/in		.006	.004
0-degree laminate:	E_{11} MSI	27.0	31.0
	E_{22} MSI	25.5	20.0
	E_{33} MSI	25.5	20.0
	ν_{12}	.23	.25
	ν_{13}	.23	.27
	ν_{23}	.35	.27
	G_{12} MSI	1.0	7.0
	G_{13} MSI	1.0	7.0
	G_{23} MSI	0.9	6.8
Matrix layer:	$E_{11}=E_{22}=E_{33}$ MSI	.49	10.2
	$\nu_{12}=\nu_{13}=\nu_{23}$	.31	.33
	$G_{12}=G_{13}=G_{23}$ MSI	.19	3.84
Debond layer:	$E_{11}=E_{22}=E_{33}$ PSI	1.0	1.0
	$\nu_{12}=\nu_{13}=\nu_{23}$	.31	.33
	$G_{12}=G_{13}=G_{23}$ PSI	.382	.376

TABLE VIII

Average Stress Values and Strain Energy Values Calculated Using Fiber/Sheath Model.

Parameter	B/Ep	B/Al
Stresses before debonding in PSI.....		
$\sigma'_{\theta\theta}=\sigma'_{rr}$	-60	-1100
σ'_{zz}	347,000	320,000
$\sigma_{\theta\theta}$	692,000	3098
σ_{rr}	-692,000	740
σ_{zz}	2982	15,000
Stresses after debonding in PSI.....		
$\sigma'_{\theta\theta}=\sigma'_{rr}$	0	0
σ'_{zz}	347,000	232,000
$\sigma_{\theta\theta}=\sigma_{rr}$	0	0
σ_{zz}	2940	15,000
Strain energy before debonding in in-#/in.....		
U'	.01311	.0139
U	.0333	.001144
Strain energy after debonding in in-#/in.....		
U'	.01311	.0114
U	.00005	.001148

TABLE IX

Computed Strain Energy Values Associated with Delamination Using Computer Program and Composite Configuration of $(0°;M;-45°;M;+45°;0°)_{sym.}$.

Configuration		B/Ep	B/Al
U(in-#) for	M,M*	5.0597	5.110
	M,D	4.9555	4.8438
	D,M	4.8998	4.9750
	D,D	4.8153	4.6325

*where: M--matrix
D--delamination

TABLE X

Strain Energy Released for Different Damage Mechanisms.

Damage Mechanism		G(in-#/in^2) for B/Ep	G(in-#/in^2) for B/Al
Fiber/Matrix Debonding		2.6445	.1396
Delamination:	MM to MD	.1296	.3312
	MM to DM	.1989	.1680
	MM to DD	.1520	.2970
	MD to DD	.1744	.2628
	DM to DD	.1051	.4260
Fiber Breakage:			
-in terms of debond length.....		1043.9(d(in))	----
-approximation based on equation 27.....		----	21.72

probability of occurance of several damage mechanisms otherwise is the same, then the mechanism most likely to occur first will be the one which has the highest potential for release of stored strain energy. The purpose of this section will be to compare the predictions of this theory, based on the strain energy release values tabulated in Table X, with observation made both visually and utilizing scanning electron microscopy, of the damage propagation and the resulting fracture of B/Ep and B/Al composite specimens. Finally, on the basis of these comparisons, a model will be proposed for each composite system.

First, considering B/Ep, the SERPT theory predicts that, initially, the fiber/matrix will debond. Since fiber breakage is related to the debond length for a given fiber, it is possible to predict the debond length prior to fracture in the following manner. Initially when the debond length is small, the potential strain energy release for fiber fracture is also small (this assumes that there is sufficient stress within the fiber for fracture). But as the debond length increases, the potential strain energy release for fiber fracture increases, while the the potential strain energy release for debonding remains constant. Therefore, when the potential strain energy release for fiber fracture exceeds that for debonding, at some critical debond length, the fiber will fracture. This is expressed as:

$$G_{fiber}\left(\frac{in\text{-}\#}{in^3}\right) \times d_{crit.}(in) \geq G_{debond}\left(\frac{in\text{-}\#}{in^2}\right). \quad \text{Eq.(28)}$$

Using a fiber failure stress of 450KSI for B/Ep, the critical debond length is approximately one half of a fiber diameter. This is somewhat low, based on scanning electron micrographs, the value ranged from one to two fiber diameters. But considering the following, this correlation is

considered to be very good. The assumed failure stress of 450KSI is quite high. Since the material is quite notch sensitive, the value is more likely close to 350KSI due to damage during fabrication. Also, the scanning electron microscope observation were of angle-plied composites, subjecting the fiber to a combined stress state, which could have the effect of further lowering the effective failure stress. Accounting for these factors, in calculating the critical debond length, gives a somewhat higher value (1.0 to 1.5 fiber diameters), therefore showing better correlation between theory and observation.

Now examining the strain energy release values for delamination in B/Ep, the most probable delamination site would be the outside $0^\circ/-45^\circ$ interface, followed by the $\pm 45^\circ$ interface. Comparing this with experimental oservations, this is consistentely the case. During the fatigue tests, after a significant amount of vertical damage (this appears as an 'H' around the hole in the specimen, with the sides of the 'H' parallel to the loading direction) has occurred, $0^\circ/-45^\circ$ delamination is usually noted both above and below the hole. This has also been confirmed by scanning electron micrographs which show the $0^\circ/-45^\circ$ interface to be the most consistently and severely delaminated. It should be pointed out that there is some delamination present between all plies. This is to be expected since, as evidenced by Table VII, there are extremely high stresses in the matrix. Generally, these stresses are higher than the matrix material can withstand. Therefore, there is a substantial amount of intra-matrix cracking and crazing. This matrix damage serves to provide initiation sites for future damage, which leads to delamination of all interfaces with the exception of the $0^\circ/0^\circ$ case. Also, since the analysis, both closed form and finite element, is elastic and does not account for

the presence of damage, the values listed in Table X can be compared to each other only before large amounts of damage have occurred. Once there is significant damage, their absolute values are no longer valid for comparison. It is, however, postulated that the relative values of the strain energy release may be compared between the cases of debonding and fiber breakage and also between the possible delamination sites. Therefore, for the case of B/Ep, although debonding and fiber breakage may increase the potential for strain energy release due to delamination, the initial preferential ordering should not be altered.

Based on the previous discussion, the failure model for a brittle matrix composite with a high fiber/matrix modulus ratio would be as follows. Initially, caused by very high matrix stress, there would be much small scale matrix cracking. This cracking initiates fiber/matrix debonding, which grows to a critical length until the fiber fractures. Debonding is then further initiated in the surrounding and proceeds intil fiber breakage occurs. These processes would tend to increase the potential for strain energy release due to delamination, and delamination would subsequently occur. The ordering, as indicated by the strain energy release values shown in Table X, would remain the same. The delamination should occur first and be most severe at the $0^{\circ}/-45^{\circ}$ interface, followed by the $\pm 45^{\circ}$ position and then the $+45^{\circ}/0^{\circ}$ position (least severe). Delamination at the $0^{\circ}/0^{\circ}$ interface should be highly unlikely. Caused by large amounts of debonding and delamination, the matrix is severely degraded and in high damage zones (such as around the 'H' pattern) crumbles and 'falls out' of the composite system. Finally, the previously mentioned mechanisms propagate and coalesce to cause failure.

Next considering B/Al, a ductile matrix, low fiber/matrix modulus ratio composite. For this material the damage mode preference and the mechanisms of damage propagation are quite different from B/Ep. Due to the extremely low potential for strain energy release due to debonding, especially as compared to B/Ep, debonding is predicted to be highly unlikely. This is found to be the case, as evidenced by scanning electron microscopy, which indicates no presence of fiber/matrix debonding. Also, once there is significant plastic deformation of the matrix material and a sufficient stress concentration developes to cause fiber stresses to rise near the critical value, fiber breakage is very likely due to the high value of potential strain energy release. It should be noted that the value listed in Table VIII is somewhat high because of several approximations made in its calculation, but it is quite apparent that it should be, by far, the most probable initial damage mechanism.

Delamination shoul occur in a different sequence for B/Al than B/Ep. As shown in Table X, the $\pm 45^{\circ}$ site is the most probable, with the $0^{\circ}/-45^{\circ}$ site a poor second. And again, as in the previous cases, experimental observation and scanning electron microscopy have shown this to be the case. All interfaces, with the exception of the $0^{\circ}/0^{\circ}$ and sometimes the $+45^{\circ}/0^{\circ}$ sites, show some delamination, but the $\pm 45^{\circ}$ site is found to be the most severe.

Now in constructing a failure model for B/Al, a necessary consideration is what causes the initial stress concentration sufficient to induce close-to-failure level stresses in the fiber. Scanning electron microscopy has revealed the presence of line-voids (separations of the aluminum/aluminum diffusion bond between the fibers). Therefore, when the matrix is deformed plastically, there

is some opening of these line-voids, causing a stress riser that quite possibly initiates fiber breakage. This would further increase stress concentrations in surrounding fibers, which then would continue to fracture. These fiber fractures, then, increase the potential strain energy release for delamination, and delamination takes place, preferentially controlled by the maximum potential for strain energy release. These damage mechanisms then are thought to coalesce and form an irregular fracture surface which is non-uniform in direction and in its' plane of propagation, which eventually leads to failure.

CONCLUSIONS

As evidenced by the previous sections, there is substantial agreement between the Strain Energy Release-Potential Theory (SERPT) and the experimental findings. In summary, several conclusions can be drawn.

An explanation of situations where in the fiber or the matrix controls composite material damage development can be put forth. For the case where there is substantial (elastic) property mismatch, as indicated by a high modulus ratio, there is higher tendency for the fiber and matrix to separate. This leads to debonding and eventual matrix degradation, which causes failure; this may be characterized as matrix-controlled damage development. When the modulus ratio is low, this tendency for separation is less and debonding is much less likely to occur. In that case, fiber breakage is much more likely, initiating and dominating failure; this may be characterized as fiber-controlled damage development. An important conclusion is, then, that the fiber/matrix modulus ratio plays a substantial role in composite material fatigue response.

Using the Strain Energy Release-Potential Theory,

debond probability and length can be predicted. Also, the most probable delamination sites can be determined. The initial inter-relationship between the occurence of different damage mechanisms can be explained in terms of relative probabilities of occurence based on relative potential for strain energy release.

By addition of the probability of occurrence (not including the previously discussed energy considerations) to the Strain Energy Release-Potential Theory, it would provide the foundation for a theoretical estimation of a critical strain energy release rate for a composite material system. It is this that provides the basis for future work.

CHAPTER VII
SUMMARY

In the preceeding chapters, many aspects of fatigue damage in fiber reinforced composite materials have been explored. By taking a many faceted approach, there is the inherent advantage that the end result is reached by means of several different viewpoints, all converging to support a given conclusion.

To account for the effect of cyclic frequency on fatigue damage, the experimental results of chapter II were combined with the physical observations of chapter III. This resulted not only in delineating the effect of cyclic frequency on structural parameters, but also formed the basis from which a micro-mechanical model of damage propagation, accounting for the effects of frequency and relative fiber/matrix bond strengths, was developed.

Characterization of the fatigue damage process involved utilizing the experimental evidence in chapter II to develope the relationships between damage extent and propagation, and energy-emission techniques dicussed in chapters IV and V. By means of a suitable first law of thermodynamics analysis, both of these experimental methods can be related to the Strain Energy Release-Potential theory postulated in chapter VI. Using this theory as the basis, damage initiation and propagation models were constructed for B/Ep and B/Al composites. These models and predictions based on these models were compared with the observations and the model developed in chapter II, and the comparison was both valid and substantial. The end result is a new energy-based failure theory that has been substantiated by physical observations and two energy-

related damage measurement techniques that constitute the foundation of experimental verification of this theory.

Several other more specific conclusions and trends have been noted in this work. They are listed as follows:

1. Damage extent and propagation is dependent upon cyclic frequency in composite materials. This is evidenced by a nearly linear relationship between change in dynamic compliance and frequency for both B/Ep and B/Al, with 15Hz having the greatest change and 45Hz the least.
2. The greater amounts of damage developed at low frequencies (15Hz) compared to high frequencies (45Hz) can be partially explained by a local time-at-load argument. This conclusion is also supported by the scanning electron microscope fractographs.
3. The effects of quasi-static specimen preloading and low-load precycling on the fatigue response of composite materials appears to be matrix dependent, as evidenced by the different results obtained with B/Al and B/Ep.
4. Energy-emission techniques can be used successfully to measure the damage extent and propagation in composite materials. This conclusion is supported by a first order (linear) relationship between totalized counts and remote structural compliance in the case of acoustic emission; and a good correlation between the thermal image and the damage affected zone and fracture mode for the case of thermal emissions.
5. Utilizing the Strain Energy Release-Potential Theory, it is possible to predict whether the fiber/matrix interface will debond, the approxi-

mate critical debond length for fiber fracture, and the most probable delamination sites as well as the relative extent of delamination at these sites with some success. Both these predictions and the model from which they are derived have been substantiated by scanning electron microscope fractographs.

In general, the investigation represents a reasonably complete attempt at a rational account of the fatigue damage process in these two composite materials. The results suggest that, while classical characterizations of self-similar single flaw propagation are inadequate for composite materials, reasonable mechanical models can be constructed which appear to represent some useful aspects of the response. In particular, the generalized strain energy release concepts described above would be very useful in predicting the fatigue response of other composite materials if they can be extended and further substantiated. Much additional work is necessary before such an extension can be made.

The investigation has also provided the first documentation of a new effect, the influence of cyclic frequency on the fatigue response of these materials. These effects are substantial and important. They can result in large differences in resultant damage as measured by stiffness changes and/or residual strength, as well as large differences in the mode of failure.

The investigation has also served to clarify need for additional work. A data base comparable to that reported previously is needed in other materials, such as graphite/epoxy. The energy-release concepts need to be further refined and developed to point where they can be used

for quantitative predictions of such things as fatigue life or residual strength. Other parametric changes should be examined, including change of geometry and variation of ply orientation. Perhaps the greatest need is for continued efforts to characterize the micro-mechanisms which act in concert to produce fatigue damage in composite materials.

REFERENCES CITED

1. Coffin,L.F.,Jr.,"Fatigue", Annual Review of Material Science, Vol. 2,(1972).
2. Cessna, L.C., Levens, J.A.,and Thomson, J.B.,"Flexural Fatigue of Glass Reinforced Themoplastics",24th Annual Tech. Conf.of SPI,(1969).
3. Owens, M.J. and Morris, S.,"An Assessment of the Potential of Carbon Fiber Reinforced Plastics as Fatigue Resistent Materials", 25th Annual Tech. Conf. of SPI, (1970).
4. Santelli, M.L.,and Simon, R.A., "Fatigue Testing of Graphite Fiber Composites", 26th Annual Tech. Conf. of SPI,(1971).
5. Salkind, M.J.,"Fatigue of Composites", ASTM STP 497, (1972).
6. Christian, J.L., "Axial Fatigue Properties of Metal Matrix Composites", presented at Fall Symp. of the ASTM, Bal Harbor, Fla.,(1973).
7. Broutman, L.J. and Krock, R.H., Modern Composite Materials, Addison-Wesley Publishing Co.,(1967).
8. Boller, K.,"Fatigue Characteristics of Reinforced Plastic Laminates Subjected to Axial Loading", ASTM STP 460, (1969).
9. Baker, A.A., Braddick, D.M. and Jackson,P.W., "Fatigue of B/Al and C/Al Fiber Composites", J. of Mat. Sc., Vol.7,(1972).
10. Schwabe, J.E., "Composite Material Fatigue Crazing: Detection and Measurement",presented at ASTM Spring Symp., Las Vegas,(1974).
11. Underwood, J.H.,"Crack Tip Deformation Measurements Accompanying Fracture in Fibrous and Laminar Composites", Technical Report No. WVT-7201, Watervliet Arsenal, June, 1974.
12. Beaumont, P.R. and Tetelman, A.S.,"The Fracture Strength and Toughness of Fibrous Composites", UCLA-ENG-7269, Livermore, Calif.,Aug.,1972.
13. Konish, H.T., Cruse,T.A. and Swedlow, J.L.,"Method for Estimating Fracture Strength of Specially Orthotropic Composite Laminates",ASTM STP 521, (1973).

14. Zweben, C., "Fracture Mechanics and Composite Materials: A Critical Analysis", ASTM STP 521, (1973).

15. Waddoups, M.E., Eisenmann, J.R. and Kaminski, B.E., "Microscopic Fracture Mechanics of Advanced Composite Materials", J. of Composite Mat.,Vol.5, Oct., (1971).

16. Mandell, J.F.,and Meier, U.,"Fatigue Crack Propagation in 0°/90° E-Glass/Epoxy Composites", presented at the ASTM Fall Symp., Bal Harbor, Fla., Dec.,1973.

17. Dally, J.W. and Broutman, L.J., "Frequency Effects on the Fatigue of Glass Reinforced Plastics", J. of Comp. osite Mat., Vol.1, (1967).

18. Liu, C.T., Stinchcomb, W.W. and Heller, R.A., private communications, 1974.

19. Williams, R.S., Reifsnider, K.L., Stinchcomb, W.W., and Turgay, H.T., "The Effect of Frequency on the Fatigue Damage of Boron/Aluminum Fiber Reinforced Composite Materials", AFOSR Technical Report, Contract no. AFOSR-72-2358, Oct.,1974.

20. Williams, R.S., Reifsnider, K.L., Stinchcomb, W.W. and Turgay, H.T., "The Effect of Frequency and Strain Amplitude on the Fatigue Damage of Boron/Epoxy Fiber Reinforced Composite Materials", AFOSR Technical Report, Contract no. AFOSR-72-2358, Oct.,1974.

21. Reifsnider, K.L., Stinchcomb, W.W.,Williams, R.S. and Marcus, L.A., "Heat Generation in Composite Materials During Fatigue Loading", Technical Report no. AFOSR-TR-73-1961, May,1973.

22. Stinchcomb, W.W., Reifsnider, K.L., Marcus, L.A. and Williams, R.S., "Effects of Cyclic Frequency on the Mechanical Properties of Composite Materials", Technical Report no. AFOSR-TR-73-1907, July,1973.

23. Raske, D.T. and Morrow, J., "Mechanics of Materials in Low Cycle Fatigue Testing", ASTM STP 465, (1969).

24. Schultz, A.B. and Tsai, S.W., "Measurement of Complex Dynamic Moduli for Laminated Fiber Reinforced Composites", J. of Composite Mat., Vol.3, July, (1969).

25. Cooper, G., "Forming Processes for Metal-Matrix Composites", Composites, Vol.1, No.3, March, (1970).

26. Darondi, T., Vedula, K.M.,and Heckel, R.W., "Fabrication of Composites by Diffusion Processing", Met. Trans., Vol.2, Jan., (1972).

27. Tressler, R.E. and Moore, T.L., "SEM Study of Sapphire Filament Reinforced Metals", Scanning Electron Microscopy/1970, 3rd Annual Proc., April, 1970.

28. Steele, J.H.,Jr., "A Microradiographic Study of Fracture in Boron Filament-Aluminum Matrix Composite", IMS Proc., (1970).

29. Herring, H.W., Lytton, J.L. and Steele, J.H.,Jr., "Experimental Observations of Tensile Fracture in Unidirectional Boron Filament Reinforced Aluminum Sheet", Met. Trans., Vol.4, March, (1973).

30. Toy,A. and Engguist, R.D., "SEM Fractography of Carbon Fiber Reinforced P13N Polymide Composites", Scanning Electron Microscopy/1969, 2nd Annual Proc., April,1969.

31. Thornton, P., "Fatigue Crack Progation in a Discontinuous Composite", J. of Composite Mat., Vol.6, Jan., (1972).

32. Marcus, L.A., Stinchcomb, W.W., and Turgay, H.T., "Fatigue Crack Initiation in a Boron Epoxy Plate with a Circular Hole", Technical Report no. AFOSR-TR-74-0833, Feb.,1974.

33. Williams, R.S. and Reifsnider, K.L., "Investigation of Acoustic Emission During Fatigue Loading of Composite Specimens", J. of Composite Mat.,Vol.8, Oct., (1974).

34. Paris, P.C., "The Fracture Mechanics Approach to Fatigue",Proc. of the 10th Sagamore Army Mech. Res. Conf., Syracuse Univ. Press, N.Y., (1964).

35. Jones, G.L., "Acoustic Emission Studies in Composites and Composite Reinforced Metals", Materials Eng. Sc. PhD Dissertation, V.P.I.&S.U., Blacksburg, VA.,1974.

36. Reifsnider, K.L. and Williams, R.S., "Determination of Fatigue Related Heat Emission in Composite Materials", Exp. Mech.,Dec., (1974).

37. Liptai, R.G. and Tatro, C.A., "Acoustic Emission Techniques in Nondestructive Testing", Proc. of the 7th Int. Conf. on NDT, Warsaw, Poland, June, 1973.

38. Harris, D.O., Tetelman, A.S. , Darwish, F.A.I., "Detection of Fiber Cracking by Acoustic Emission", Dunegan Corp. Technical Report no.DRC 71-1, (1971).

39. Reifsnider, K.L. and Stinchcomb, W.W., "Investigation of Dynamic Heat Emission Patterns in Mechanical and Chemical Systems", presented at the IRIE Conf., St. Louis, Aug.,1974.

40. Corten, H.T., "Fracture Mechanics of Composites", Fracture Vol.VII, Academic Press Inc.,N.Y.,(1972).

41. Orowan, E., "Energy Criterion of Fracture", Welding Res. Supplement, March,(1955).

42. Irwin G.R. and Kies, J.A., "Critical Energy Rate Analysis of Fracture Strenght", Welding Res. Supplement, April, (1954).

43. Sih, G.C., "Introductory Chapter: A Special Theory of Crack Propagation", Mechanics of Fracture I, edited by G.C. Sih, Noordhoff Int. Press, Leyden, (1973).

44. Ebert L.J. and Gadd, J.D., "A Mathematical Model for the Mechanical Behavior of Interfaces in Composite Materials", Fiber Composite Materials, ASM pub.,(1964).

45. Dana, J.R., "Three Dimensional Finite Element Analysis of Thick Laminated Composites--Including Interlaminar and Boundary Effects Near Circular Holes", PhD Dissertation, Engineering Science and Mechanics, V.P.I. &S.U., Blacksburg, VA.,1973.

46. Barker, R.M., Dana, J.R. and Pryor, C.W., "Three Dimensional Analysis of Stress Concentrations Near Holes in Laminated Composites", Technical Report no. VPI-E-72-27, V.P.I.&S.U., Blacksburg, VA.,Dec.,1972.

47. Dana, J.R. and Barker, R.M., "Three Dimensional Finite Element Program: User's Guide", Technical Report no. VPI-E-74-19, V.P.I.&S.U., Blacksburg, VA.,Aug.,1974.

48. Nair, P. and Reifsnider, K.L., "Unimod: An Applications Oriented Scheme for the Analysis of Fracture Mechanics Problems", ASTM STP 560, (1974).

49. Olster, E.F. and Jones, R.C., "Toughening Mechanisms in Continuous Filament Unidirectionally Reinforced Composites", ASTM STP 497, (1972).

50. Barker, R.M. and MacLaughlin, T.F., "Stress Concentrations Near a Discontinuity in Fibrous Composites", J. of Composite Materials, Vol.5, Oct.,(1971).

51. Iremonger, M.J. and Wood, W.G., "Stresses in a Composite Material with a Single Broken Fiber", J. of Strain Anal., Vol.2, No.3,(1967).

52. Erdogan, F. and Pacella, A.H., "A Penny-Shaped Crack in a Filament-Reinforced Matrix-I. The Filament Model", Int. J. of Solid Struct., Vol.10, (1974).

53. Pacella, A.H. and Erdogan, F., "A penny- Shaped Crack in a Filament-Reinforced Matrix-II. The Crack Problem", Int. J. of Solid Struct., Vol.10, (1974).

54. Iremonger, M.J. and Wood, W.G., "Plastic Flow and Failure of Discontinuous Fiber Composite Materials", J. of Strain Anal., Vol.5, No.3, (1970).

55. Grossman, L.M., Thermodynamics and Statistical Mechanics, McGraw-Hill Book Co., (1969).

The vita has been removed from the scanned document

FATIGUE DAMAGE MECHANISMS IN FIBER REINFORCED COMPOSITE MATERIALS INCLUDING THE EFFECT OF CYCLIC LOADING FREQUENCY

by

Richard Scott Williams

(ABSTRACT)

A broad-based investigation seeking to characterize fatigue damage mechanisms in fiber reinforced composite materials, accounting for the effect of cyclic loading frequency, is presented. A many faceted approach to the investigation was utilized; which included well documented strain-controlled fatigue tests, a scanning electron microscopy study, implementation of energy emission techniques (such as acoustic and thermal emissions), and the development of an energy-based failure theory.

A detailed discussion of each aspect of the investigation is presented and, in each case, pertinent conclusions are drawn.

The effect of cyclic loading frequency on fatigue damage development is documented and found to be substantial. A micro-mechanical damage model, which accounts for the effects of frequency and fiber/matrix interface strength, is developed. Using a first law analysis, a good correlation between acoustic and thermal emission with damage propagation and extent is developed. Finally, a new conceptual theory, called the Strain Energy Release-Potential Theory, is postulated. Predictions based on this theory are made and compared with experimental findings, resulting in substantial agreement.